ADVANCED POROUS SILICON PHOTONIC DEVICES FOR BIOSENSING APPLICATIONS

By

Gilberto A. Rodriguez

Dissertation
Submitted to the Faculty of the
Graduate School of Vanderbilt University
in partial fulfillment of the requirements
for the degree of
DOCTOR OF PHILOSOPHY
in
Electrical Engineering

May, 2016
Nashville, Tennessee

Approved:
Prof. Sharon M. Weiss
Prof. Rizia Bhardan
Prof. Ronald Schrimpf
Prof. Jason Valentine
Prof. Yaqiong Xu

For my parents,

for always believing in me.

ACKNOWLEDGEMENTS

First and foremost, I am grateful of Prof. Sharon Weiss who has been the best the Ph.D. advisor I could have asked for. I thank her for taking a chance on me even though I had minimal research experience and had never taken an optics course. Her encouragement, support, patience, and guidance have led to my success and have tremendously helped improve myself as both a researcher and a professional. Her expertise and talent has led to me tremendously improving my theoretical knowledge, writing and presentation skills, and my analytical and technical skills. Her hard work and value placed on the research was inspiring for me to never give up and to work through the rough patches whenever challenges were encountered.

I have had the opportunity to be mentored and work alongside some truly brilliant minds throughout my career at Vanderbilt. I would like to particularly acknowledge Dr. Judson Ryckman, Dr. Yang Jiao, Dr. Jeremy Mares, Dr. Petr Markov, Shuren Hu, Joshua Fain, Yiliang Zhao, Kelsey Beavers, Kevin Miller, Francis Afzal, Robert Fuller, John Lonai, and Alyssa Cartwright. These people have had a significant impact and contribution to the work presented in this thesis and I have learned a lot from our discussions and feedback. Even more importantly, I would like to thank them for their friendship and comradery and for the great people they have been to me.

This work would not be possible without the help of Dr. Scott Retterer, Dr. Ivan Kravchenko, Dayrl Briggs, Dale Hensley, and Kevin Lester from the Oak Ridge National Laboratory. I am grateful for their patience throughout instrument trainings and thankful for their fabrication expertise that allowed the successful demonstrations of the devices in this work. I would also like to thank the VINSE staff, in particular, Dr. Anthony Hmelo for his patience and dedication to keeping the cleanroom and electron beam lithography system in tip-top shape. The

work presented in this thesis was funded in part by the Army Research Office (W911NF-09-1-0101) and National Science Foundation (ECCS-0746296).

I am thankful of my parents and sister who have had to deal with my stressed and exhausted self over the last five years. Their support throughout my entire college career has never wavered and has always kept me focused and determined to succeed. Lastly, I would like to thank Jessica Tumolo and Pumpkin the cat for the wonderful destressing evenings after getting home from lab. Words cannot express my gratitude to all the people and cat listed, but know that I could not have completed my Ph.D. work and thesis without them.

TABLE OF CONTENTS

PAGE

CHAPTER

LIST OF FIGURES

LIST OF TABLES

CHAPTER 1

INTRODUCTION

1.1 Optical Biosensors

Biosensors are analytical devices that transduce the presence of chemical or biological molecules into a measurable optical or electrical signal. The ability to detect specific analytes and molecules is prevalent in medical and research laboratories, where trained personnel are able to detect hazardous analytes collected from a blood, soil, or water sample using expensive, sophisticated equipment. However, with the progression of the internet-of-things and wearable technology, the demand for immediate detection of hazardous chemical and biological markers has been increasing [1,2]. For example, current diagnostic methods are not capable of efficiently preventing a military troop from entering an area containing explosive chemicals, preventing a customer at a restaurant from eating E. coli contaminated food, or detecting early signs of cancer that would reduce painful and costly future treatments. One vision for an effective point of care (POC) diagnostics device, shown in Figure 1.1, was proposed by IBM in 2011 to motivate biosensing researchers to focus their efforts on producing compact, low cost (~$1), disposable, simple-to-use, portable, high fidelity, and high sensitivity lab-on-a-chip biosensors [1]. This biosensor includes a sample processing area where the analyte of interest is placed. The microfluidic chip section of the sensor incorporates on-chip channels and pumps to transfer the analyte to the transducer. The transducer is the active sensing region that is chemically functionalized to specifically bind to the target molecule of interest within the analyte. Finally, electronics are used to process the transducer's electronic or optical signal to provide a rapid, real-time read-out containing the diagnostic information. Current biosensor research is heavily focused on optimizing the transducer and surface chemistry for capture of various target molecules, investigating materials functionalized to detect labeled and label-free biological agents such as DNA [3-7], proteins, and antibodies [8-12]. For detection of specific bioanalytes, label-free photonic sensing platforms utilizing silicon-on-insulator (SOI) substrates have emerged as powerful tools that can address sensor applications spanning medical diagnostics, food safety, and homeland security [13-15]. Recently, a table top biosensing system based on SOI technology has been commercialized [16]. SOI optical platforms leverage silicon microelectronics fabrication methods and can provide simple detection measurements by monitoring refractometric changes caused by the presence of surface-bound molecules. In particular, SOI waveguide (WG) – based technology has been demonstrated for high sensitivity, compact, and multiplexed devices and they hold promise for integration with microelectronic devices including smart phone technology [17-22]. Typically, the most sensitive of these types of biosensors function through the utilization of strong local electric fields that spatially and temporally interact with surface bound molecules specifically attached to the sensor, leading to a quantifiable refractive index change measured by a resonance wavelength shift [23,24]. Sensitivity is quantified by the change in optical or electrical properties that results from the infiltration and attachment of target molecules. Sensitivity is often reported as the change in a particular electrical or optical property (e.g., change in capacitance or optical resonance shift) divided by the concentration or number of molecules exposed to the sensor. In optical systems, sensitivity can also be reported in terms of the magnitude of the shift in the optical spectrum divided by the refractive index change due to the exposure of target molecules to the sensor (i.e., units of nm/RIU or degrees/RIU) [17,24].

Although realized commercially, SOI optical biosensors have encountered key limitations. For example, the WG-based structures are oriented such that a majority of the electric field is within the solid material and only an evanescent field decaying at the surface of the WG interacts with the surface bound molecules, resulting in a limited sensitivity [3,25-28]. Also, nonlinear effects arise when employing SOI WG structures and cause unstable resonances that are susceptible to changing environmental conditions such as temperature and input laser power fluctuations which may lead to false positive read-outs in field applications [29-32]. Moreover, the SOI platform itself may be cost-prohibitive for some POC systems. In this work, by replacing the SOI material platform with porous silicon (PSi), we demonstrate the potential to simultaneously improve upon cost, sensitivity, and minimization of nonlinear thermo-optic effects while maintaining feasible integration with microfluidics, microelectronics, and multiplexed configurations by replacing the SOI material platform with porous silicon (PSi).

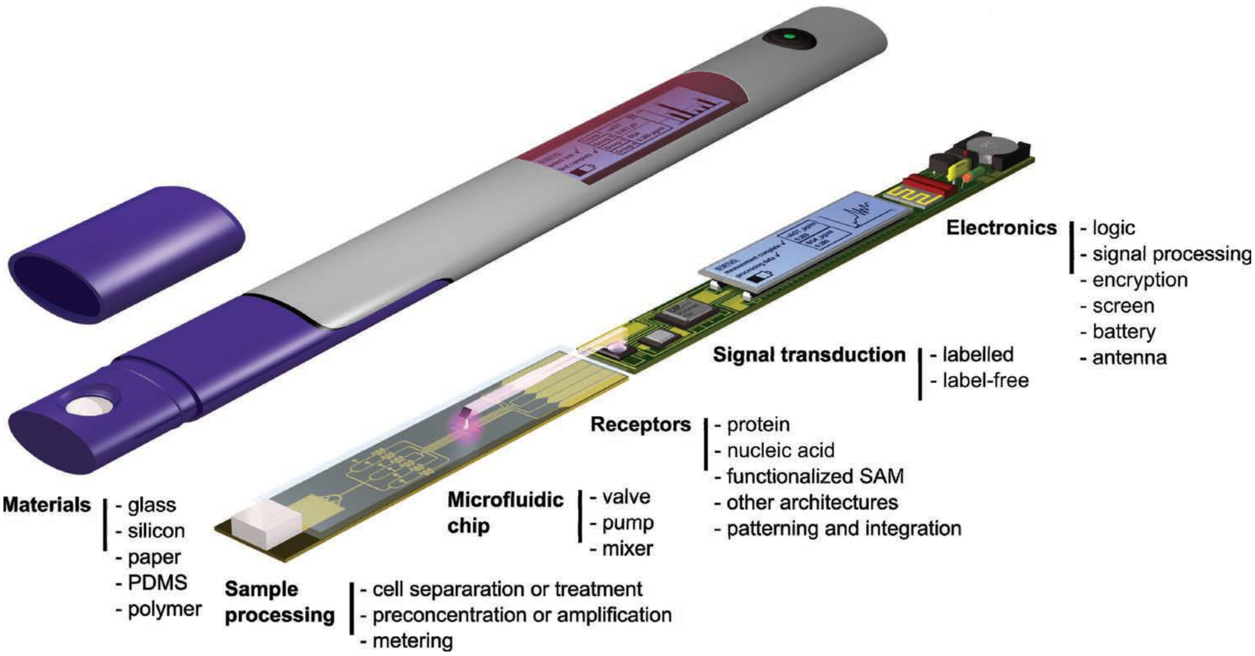

Figure 1.1 Model of the “ideal POC diagnostics device” proposed by IBM, reproduced from [1].

1.2 Porous Silicon Biosensing

1.2.1 Formation and Fabrication

PSi is a versatile material whose unique geometry and material properties have led to applications in biomedical sensing, optoelectronics, drug delivery, and energy conversion [33-37]. PSi is fabricated by the electrochemical etching of a p- or n- doped silicon wafer in a hydrofluoric acid solution. Unilateral straight pore formation aligns with the <100> Miller index of the Si crystal as a result of excess Si-H bonds found in this crystal orientation [33,38,39]. Formation of PSi occurs through Si corrosion induced by Si-H bonds at the surface of the wafer and F^- ions within the electrolytic solution. The creation of Si-F bonds is assisted by the presence of a charge carrier at the surface of the doped Si wafer. Due to the strength of the Si-F bond, the Si atom is highly susceptible to attack by fluorine and will react until the Si atom is completely removed from the surface in the form SiF_6^{2-}. After the Si atom is removed, a bare Si-H bond is exposed at the wafer surface and the process repeats, forming the pore [38-41]. The density of these surface reactions can be controlled by tuning the charge carrier density present at the surface. During formation of PSi via electrochemical etching, an ohmic contact (a conductive interface) controls the amount of charge flowing to the surface of the semiconductor, thus controlling the porosity of the film. The substrate carrier doping will additionally affect the porosity and pore size and PSi is commonly made using highly doped Si wafers. Application of modest current densities during electrochemical etching results in a film with porosities typically ranging from approximately 30% to 90%. Application of high current densities will result in electropolishing, which will lift off the full layer of Si and no formation of pores will be observed. Interestingly, the discovery of PSi was a result of this electropolishing procedure being used to thin down a Si wafer [40]. Using high current densities can also be utilized to lift off PSi films from their supporting Si substrates [42].

During pore formation, the pore walls are depleted of hole carriers preventing pore widening or lateral etching [33]. This allows the fabrication of multilayer PSi films with varying porosity. The porosity, thickness, and number of layers of a PSi film can be finely controlled by adjusting the applied current density and duration of electrochemical etching in a hydrofluoric acid solution [33]. Figure 1.2 displays a) the top view and b) cross sectional scanning electron microscope (SEM) images of the pore openings and multiple layers of varying porosity, respectively. In the SEM images, the brighter regions are silicon and the darker regions air. Hence, lower porosity PSi appear brighter than higher porosity.

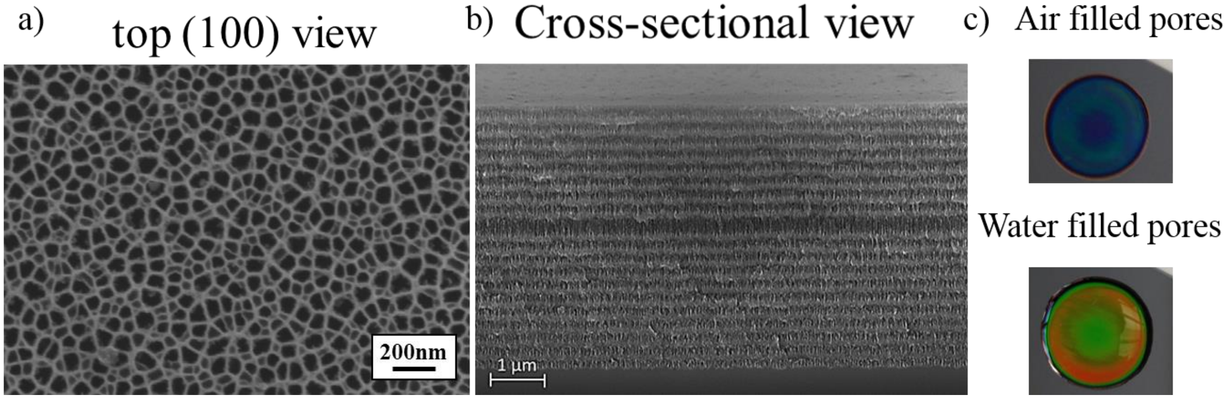

Figure 1.2 a) Top view SEM image of pore openings after electrochemical etching. b) Cross sectional SEM of a PSi microcavity with layers of alternating porosity etched at 5 mA/cm^2 (white shade) and 48 mA/cm^2 (darker shade). c) PSi multilayer sample (2 cm^2 area) with effective medium consisting of empty pores in the top image and pores filled with water causing a vibrant color change in the bottom image.

1.2.2 Effective Medium Approximation

The tunable pore dimensions between approximately 2 nm to 200 nm allow PSi films to be treated as an effective medium when incident with wavelengths that are much larger than the pore diameter, for example in the visible and IR regions [33,43]. The refractive index of a porous layer can therefore in theory be tailored between 3.5 (pure Si; 0% porosity) and 1.0 (Air; 100% porosity). In this work, the Bruggeman effective medium approximation is utilized to calculate both the refractive index and porosity of the composite materials. The porosity, P, or effective refractive index, n_{layer}, can be determined by Equation 1.1 [33,44] where $n_{skeleton}$ and n_{fill} are the refractive indices of the skeleton material (i.e. Si), and the filling material (i.e. air, water, biological analytes), respectively. The vibrant color change observed in Figure 1.2c is attributed to the large change in effective refractive index caused by changing the fill material from air to deionized (DI) water. In a similar way, for biological and chemical sensing, a spectral change results when chemical and biological agents attach within the porous layer.

$$P\frac{n_{fill}^2 - n_{layer}^2}{n_{fill}^2 + n_{layer}^2} + (1 - P)\frac{n_{skeleton}^2 - n_{layer}^2}{n_{skeleton}^2 + 2n_{layer}^2} = 0 \qquad 1.1$$

1.2.3 Porous Silicon Biosensors

PSi is an attractive label-free biosensing platform due to its highly tunable refractive index that can be exploited to form multilayered films, nonlinear properties, extremely large and accessible surface area, molecular size selectivity based on the choice of pore diameter, compatibility with standard microfluidics integration, and rapid and cost-effective fabrication. The CMOS compatible fabrication procedures for PSi and well-established surface chemistry for specific binding events designed for Si and SiO_2 surfaces make PSi a viable contender to substitute for SOI biosensors. Specific binding of several relevant molecules including DNA [45], proteins [10], explosives [46], and illicit drugs [47] to PSi platforms has been demonstrated.

PSi sensors have taken the form of many different structures ranging from single layer to multilayer films and have utilized a variety of optical and electrical transduction methods [34]. A PSi DNA sensor was first introduced by Sailor and colleagues in 1997 using a single layer PSi optical interferometer, a breakthrough that sparked significant interest in PSi as a platform for biosensing [48]. For PSi optical biosensors, capture of target molecules in the pores results in an increase in the optical thickness of the thin film due to the increase in the effective refractive index of PSi as shown in Figure 1.2c. For optical transduction methods, analytes in PSi are monitored by measuring the reflectance and transmittance [49], absorption [50,51], or photoluminescence [7,52,53] of the PSi sensor before and after exposure to the target molecules. A change in one of these optical properties suggests a positive sensor response, assuming negligible optical response to control samples such as mismatched DNA for DNA-DNA hybridization. Care must be taken in evaluating the response of a PSi sensor due to the now well-known corrosion of PSi in aqueous solutions that, especially for reflectance and transmission measurements, may lead to an opposite effect than expected due to simple material addition in the pores [54,55]. The corrosion of PSi is accelerated in the presence of negatively charged species; hence DNA detection in PSi must be carried out with charge mitigation strategies [55,56].

The large surface area of PSi, arising from the presence of nanoscale pores, allows for improved light-matter interaction, especially in PSi resonant optical structures, and therefore improved sensitivity to biomolecule binding events. Label-free sensing has been demonstrated in a wide variety of PSi resonant and non-resonant optical structures including as single-layer and double-layer interferometers [10,57], Bragg mirrors [58], rugate filters [59], microcavities [52], waveguides (WG) [25,45,60], Bloch surface wave (BSW) structures [61-64], and diffraction gratings [65]. In particular, resonant microcavities, WGs, and BSW structures have the ability to strongly confine light within a layer typically <500 nm [66]. The light-matter interaction within these thin layers leads to a more rapid detection of target molecules at a sensitivity shown to be 40 times greater than traditional nonporous SOI planar WGs [25]. Additionally, these films are of significance because they can be integrated with compact resonant devices such as ring resonators and photonic crystals [28,67]. The following sections discuss the physical properties of the films and devices.

1.3 Resonant Porous Silicon Thin Film Substrates

1.3.1 Sensitivity Definition

Microcavity, WG, and BSW structures are optical films designed to support a propagating mode. The importance of this property is the confinement of light within a thin layer that both enhances field strength and controls in-plane light propagation, representing a planar analogy to optical fiber communications. The sensitivity of these respective films is highly dependent on the intensity of light within the guided mode layer known as the active sensing region. Equations 1.2 and 1.3 define the sensitivity metric of these structures for an angular or wavelength change in the optical spectrum, where θ is the resonance angle, λ is the resonance wavelength, n_{eff} is the initial effective index of the mode, and n_p is the refractive index of the environment or prism for grating and prism configurations, respectively. The sensitivity is directly dependent on the confinement factor, Γ (Equation 1.4), which is the ratio of electric field, E, in the active sensing region, v, (the microcavity, WG, or BSW mode layer) to the total electric field, where ε is the dielectric constant [17,24]. The active sensing volumes for the microcavity, WG, and BSW are highlighted in Figure 1.3a,c,e, respectively. Although molecules are accessible to the entire porous structure, the sensor response is predominantly determined by the effective index change within the guided mode layer, and to a lesser extent by the effective index change in the Bragg mirror or cladding layer.

$$Sensitivity = \frac{d\theta}{dn} = \Gamma \cdot \frac{1}{n_p cos\theta} \qquad 1.2$$

$$Sensitivity = \frac{d\lambda}{dn} = \Gamma \cdot \frac{\lambda_{res}}{n_{eff}} \qquad 1.3$$

$$\Gamma = \frac{\int_V \varepsilon [E(r)]^2 dr^3}{\int_{-\infty}^{\infty} \varepsilon [E(r)]^2 dr^3} \qquad 1.4$$

The maximum achievable refractive index contrast between layers in PSi, approximately $\Delta n \approx 0.7$, is less than SOI for which $\Delta n \approx 2.0$. Therefore, PSi optical structures have less strongly confined modes compared to SOI photonic structures. However, the PSi WG structure can possess a detection sensitivity 10-40 times greater than a planar SOI WG for the detection of 16-mer DNA and small molecules [68]. This is due to the large active sensing volume of porous materials that overlaps with the guided mode. For nonporous materials, the active sensing volume that overlaps with the guided mode extends only about 10 nm outside the WG [17]. More than 80% of the total power is confined within the planar material and is inaccessible to the molecules [69]. In the case of PSi, molecules infiltrate the porous matrix and directly interact with the confined mode instead of the evanescent field at the surface, leading to the enhanced sensitivity. Additionally, the effective index of the mode is greatly perturbed by the infiltration of molecules changing the refractive index of the PSi layers as is described by the Bruggeman effective medium approximation [44]. The following sections describe the mechanics behind the microcavity, WG, and BSW structures.

1.3.2 Microcavities

The microcavity is one of the many PSi multilayer structures that can be straightforwardly fabricated by electrochemical etching of silicon. The microcavity consists of a pair of Bragg mirrors separated by a cavity or sensing layer deep within the structure, as shown in Figure 1.3a. The Bragg mirrors consist of alternating layers of high and low refractive index with quarter wavelength optical thickness [33]. The cavity region that breaks up the periodicity of the quarter wavelength stack introduces an allowed mode that manifests itself as a minimum in the reflectance spectrum at a designed wavelength [52]. A wavelength reflectance spectrum is shown in Figure 1.3b, with the cavity resonance highlighted in green. Strong light confinement exists in the cavity based on a photonic band gap effect further discussed in Section 1.4.2. Introduction of an analyte into the microcavity changes the overall refractive indices of the constituent layers and results in a shift of the cavity resonant wavelength as described by Equation 1.3. The microcavity spectral shift is measured using spectrophotometric measurements with near normal incident light. The need to integrate couplers such as a prism or grating that overcome total internal reflection (TIR) conditions are not required, as they are for the WG and BSW structures. Prior work has shown that the structure is very sensitive to small molecules, but sensors with sensing regions close to the top surface have been generally favored due to the concern over the time required for molecules – especially those of size only a few times smaller than the pore diameter – to diffuse into such a thick structure [60,64].

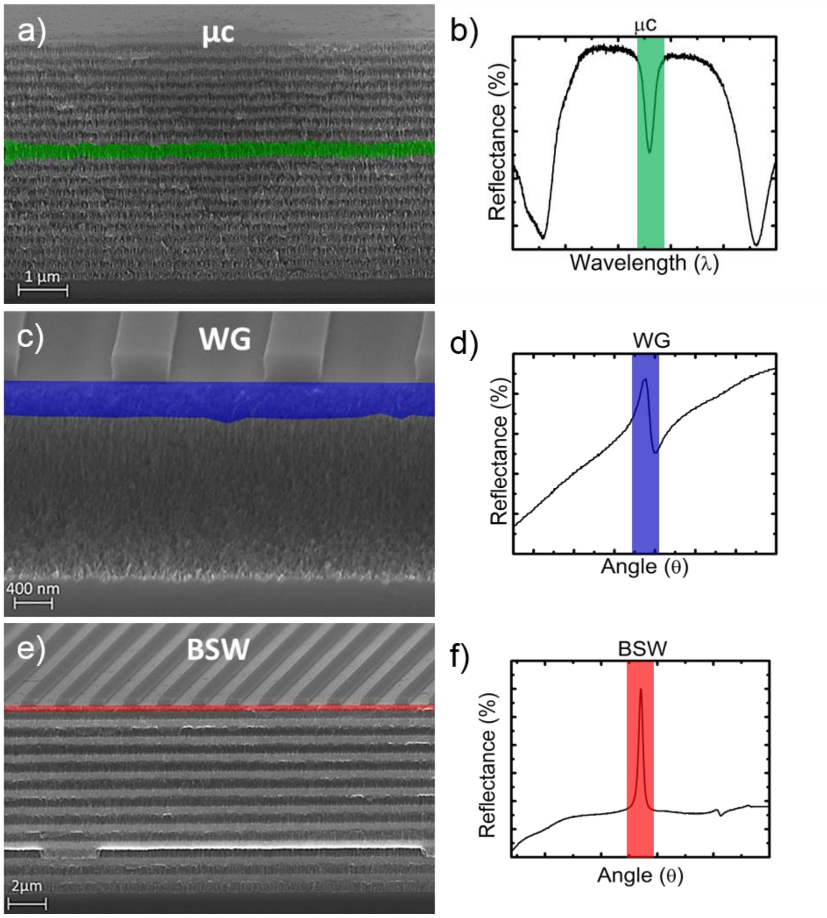

Figure 1.3 SEM image of a PSi a) microcavity, c) WG, and e) BSW structure with the active sensing region highlighted in green, blue, and red, respectively. b) Wavelength spectral measurement of the microcavity device with the resonance dip highlighted in green. Grating coupled d) WG and f) BSW angular reflectance spectra with the resonance peaks highlighted in blue and red, respectively.

1.3.3 Waveguides

The WG structure consists of a high refractive index core surrounded by cladding layers with a low refractive index. In PSi films, the WG is a two layer planar structure with a high index (low porosity) guiding layer supported by an underlying low index (high porosity) cladding layer. The cover layer commonly consists of air. Light is vertically confined by TIR within the guiding layer, which is located within the top few hundreds of nanometers of the structure. Light can be coupled into or out of the WG through use of a prism, grating, or by placing the light source (i.e., fiber-coupled laser or LED) next to the cross-section of the WG for butt coupling. Prism and grating configurations allow light to couple into the WG mode at a designated angle. Butt coupling configurations are typically administered for wavelength-resolved transmission scans.

In the grating coupled case, a transverse electric (TE) or transverse magnetic (TM) polarized light source is diffractively coupled to the WG as described by Equation 1.5 where n_{cover} is the refractive index of the cover layer above the guiding PSi layer, θ is the coupling angle measured from normal incidence, m is the diffraction order, λ_0 is the free space wavelength, and Λ is the grating pitch. At the coupling angle, the designed order of diffracted light is coupled to the high index core layer, producing a strong resonant feature in the angular reflectance spectrum [68]. Figure 1.3c shows an SEM image of a PSi grating coupled WG film. A grating coupled WG model is shown in Figure 1.4b. An example angular reflectance spectrum is shown in Figure 1.3d with the excited mode highlighted in blue.

$$n_{eff}=n_{cover}\cdot \sin\theta \pm m\cdot \frac{\lambda_0}{\Lambda} \tag{1.5}$$

$$n_{eff}=n_p\cdot \sin\theta \tag{1.6}$$

In the case of prism coupling, the second grating term on the right hand of Equation 1.5 is eliminated and the cover index is replaced by a high index prism, n_p, to give the prism coupling condition shown in Equation 1.6. A thin low index cover layer between the prism and the WG layer is required as shown in Figure 1.4a. The thickness of this cover layer may be tuned experimentally to maximize coupling efficiency; typical thicknesses are a few hundred nanometers. Light incident at the prism-cover interface will meet TIR conditions and an evanescent wave is created within the cover layer. At an incident angle defined by Equation 1.6, a phase matching condition of the evanescent field and the WG mode is met and coupling is achieved.

When liquids, gases, or molecules are introduced into the porous matrix, a refractive index change of the PSi that manifests itself as a positive change in the effective index of the WG mode causes a shift in the coupling angle to higher angle. PSi WGs have been demonstrated in both grating and prism configurations to detect DNA with limit of detection in the nM range [3,25,26,68]. For integrated biosensing applications, grating coupling is preferred because it removes the need for a bulky prism and offers the opportunity for microfluidics integration for a lab-on-a-chip platform [60]. However, angular sweeps may prove difficult in compact portable applications due to the large space and precision required for the measurements. In the butt coupling case, a wavelength sweep is utilized instead, requiring a setup with no moving components. A resonance is not observed in the spectrum, but shifts in the waveguide cutoff wavelength could be monitored for biosensing applications [70]. A preferable option for in-plane coupling is to use a cavity or ring resonator on a nonplanar WG to allow for resonant detection. In this way, either a spectral shift or change in intensity at the resonance wavelength could be monitored to monitor molecular binding events, although sensor systems monitoring intensity changes must be robust against nonspecific events that could also lead to light intensity changes. On-chip spectrometers have been demonstrated so compact spectral measurements are realizable [71].

The nonplanar WG configuration confines light in a relatively thin, high index wire. The structure is highly utilized in fiber optic communication applications and is considered the optical analog to copper interconnects in electronics. A cross sectional model of an on-chip ridge WG is shown in Figure 1.4c. The ridge WG can be integrated with a prism or grating coupler. However, most commonly, light is coupled at the edge of the structure in a butt-coupling configuration. In this configuration, an optical source is placed at the cross sectional edge of the ridge WG. Light at the air (n_1) and WG (n_2) interface must refract at a minimum designated critical angle, $\theta_{critical} = \sin^{-1}(n_2/n_1)$ in order for light to be confined by TIR [72]. Resonator devices such as the ring resonator and photonic crystal cavities integrated with ridge WGs have led to the development of on-chip optoelectronic modulators for communications applications as well as creating biosensors that can be cascaded, multiplexed, and excited from a single source [73,74]. For this reason, the study of ridge WGs in PSi have become a trending topic, with recent reports of propagation and losses [30,67,75], nonlinearities [30,76], and biosensing applications [28,67].

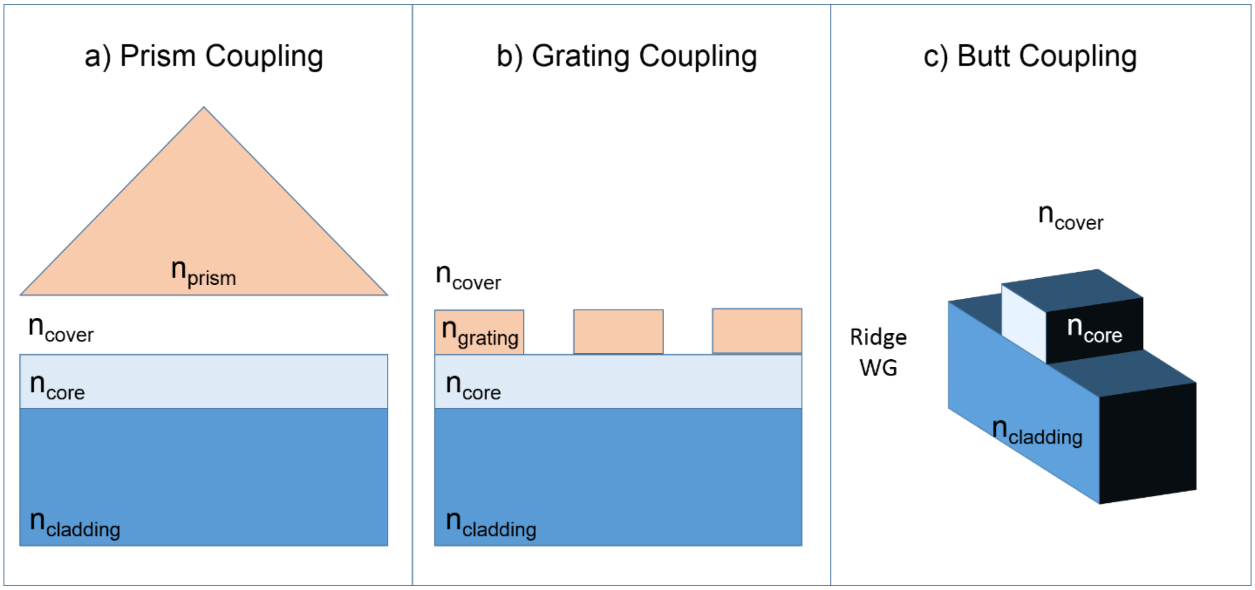

Figure 1.4 a) Prism, b) grating, and c) butt coupling configurations utilized to phase match a light source with the effective index of the core layer of a WG. Planar WGs are shown in a) and b). Nonplanar ridge WG is shown in c).

1.3.4 Bloch Surface Waves

The BSW is an optical surface state characterized by distinct field confinement at the interface between a finite 1D photonic crystal, or Bragg mirror, and an external semi-infinite medium [61,62,77]. The BSW is often considered to be the dielectric analog to the surface plasmon polariton (SPP), which provides a strong propagating field at the dielectric-metal interface due to the surface electron oscillation [78,79]. With the SPP, however, waves propagate along a lossy gold or silver surface and thus have limited propagation lengths and resonant quality factors, considerably lower than what can be achieved with all-dielectric BSW designs [78-80]. Thus, the BSW has emerged as a promising sensing platform for surface-bound molecule detection and has been experimentally demonstrated in various material platforms [61,80-83]. The BSW structure is composed of periodic layers with alternating dielectric constant similar to a Bragg mirror, but it has a truncated top layer as the surface wave guiding layer. A fabricated BSW film with integrated grating coupler is shown in Figure 1.3e. For a BSW mode, the electromagnetic field is confined to the surface of the structure due to the activation of a defect surface state within photonic band gap and total internal reflection at the air interface [80]. Note that unlike SPR modes, the BSW mode can be excited with either TE or TM polarized light. TE polarization is used for this study. In order to couple light into a BSW, mode matching between incident light and the surface wave must be accomplished. Coupling configurations similar to those employed for a WG can be used (Equation 1.5, 1.6 and Section 1.3.3). Ridge BSW structures have been previously reported [80]. The angular reflectance measurement of a grating coupled BSW film is shown in Figure 1.3f with the excited mode highlighted in red. Similar to the sensing procedure of the PSi-WG, when molecules infiltrate the PSi BSW, the effective refractive index of the PSi increases, leading to a measureable shift in the resonance angle, similarly described by Equation 1.5 where n_{eff} is the effective refractive index of the BSW mode. Moreover, molecules attached on the surface of the BSW structure will also change the effective index of the BSW mode, causing a shift in the resonance angle that allows detection of very large analytes (>1 μm in length) [66,84]. The active sensing region of the PSi BSW is at the surface of the structure where the propagating field is confined, promoting a fast sensor response to both small and large molecules as highlighted in Figure 1.3e.

1.4 Resonant Optical Devices

Optically resonant structures such as ring resonators and PhC cavities can be integrated with single mode photonic wire or ridge WGs. The objective is to design structures with small modal volume that maximize the ratio of energy stored in the cavity to the energy decaying from the cavity. The maximized ratio results in an increased confinement factor in Equation 1.4 to facilitate strong light-matter interaction and is directly measured by a high quality (Q) factor resonance. The following sections describe the mechanics of ring resonators and PhC cavities in detail.

1.4.1 Ring Resonators

The ring resonator configuration consists of a straight ridge WG in proximity to a ring shaped WG as shown in Figure 1.5a [9]. Transmitted light from the ridge WG can couple into the ring at integer multiples of the optical path length of the ring as described by Equation 1.7 where λ_{res} is the resonance wavelength, r is the radius of the ring, and m is an integer [85]. The distance between the ring and WG is tuned to achieve critical coupling, for which nearly 100% of the light is coupled to the ring.

$$\lambda_{res} = \frac{2\pi r \cdot n_{eff}}{m} \qquad 1.7$$

At λ_{res}, light from the straight WG will couple to the ring and will make multiple passes around the ring constructively interfering to create a very strong locally confined field. The discrete dependence, m in Equation 1.7, gives rise to multiple λ_{res} in the transmission spectrum separated by a wavelength interval, $\Delta\lambda_{res,}$ known as the free spectral range (FSR). Equations 1.7 and 1.8 are used to calculate the Q factor and FSR for a ring resonator, respectively, where n_g is the group index and F is the finesse which is the ratio of FSR and FWHM. The group index is used in Equation 1.9 to account for the effective index dependence on wavelength as a result of material and WG dispersion.

$$Q = \frac{\lambda_{res}}{FWHM} = \frac{n_{eff} \cdot 2\pi r}{\lambda_{res}} \cdot F \qquad 1.8$$

$$FSR = \Delta\lambda_{res} = \frac{{\lambda_{res}}^2}{n_g \cdot 2\pi r} \qquad 1.9$$

A high Q factor in optical devices is dependent on cavity design and material losses which dictate the decay rate of light within the resonant cavity. For biosensing applications, the goal is to optimize a high Q factor and a large FSR. As previously mentioned, a high Q factor yields a high detection sensitivity, and a large FSR will prevent a resonance overlap for large resonance shifts that may occur when a large quantity of molecules is bound to the sensor. If a resonance shift exceeds the FSR, a confusion in shift magnitude will arise unless continuous monitoring is performed (i.e., real-time measurements) and a false positive read-out may occur. The Q factor and FSR are inversely related to each other by the ring radius. For this reason, it is important to design a ring size that maximizes the Finesse. Figure 1.5b illustrates a typical ring resonator transmission spectrum characterized by multiple sharp resonance dips.

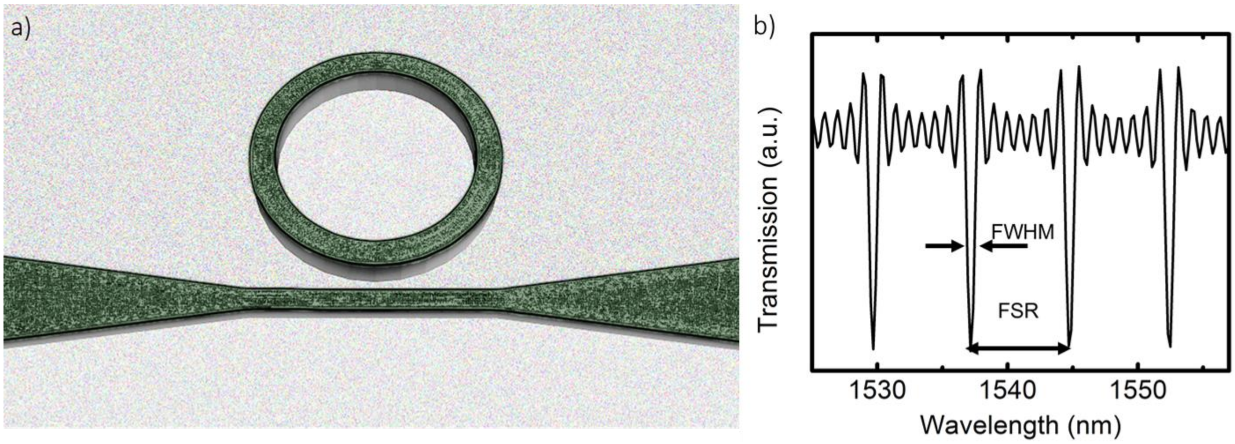

Figure 1.5. a) 3-D model of a ring resonator. b) Typical ring resonator transmission spectrum highlighting FWHM and FSR parameters.

1.4.2 Photonic Crystal Cavities

A PhC is comprised of a periodic array of alternating high and low dielectric constant materials structured to control the propagation of light. The periodic dielectric function harnesses the constructive and destructive interference properties of electromagnetic waves to create forbidden states where a mode cannot propagate known as a photonic band gap (PBG). The simplest example of a 1-dimensional PhC is a Bragg mirror (Figure 1.6a). Each layer of material has an optical thickness corresponding to one quarter of the incident wavelength of light and together the layers are designed to create constructive interference within the mirror to create a PBG, highlighted in yellow in the wavelength reflectance spectrum and dispersion relation in Figure 1.6b and c, respectively. With 100% reflectivity, no light is transmitted through the structure. At the band edge (BE), modes can exist within the dielectric mirror and are spatially concentrated within the high and low dielectric layers. Based on electromagnetic variational theorem, modes above or below the band gap will concentrate their energy in low or high dielectric constant regions known as air and dielectric modes, respectively [86].

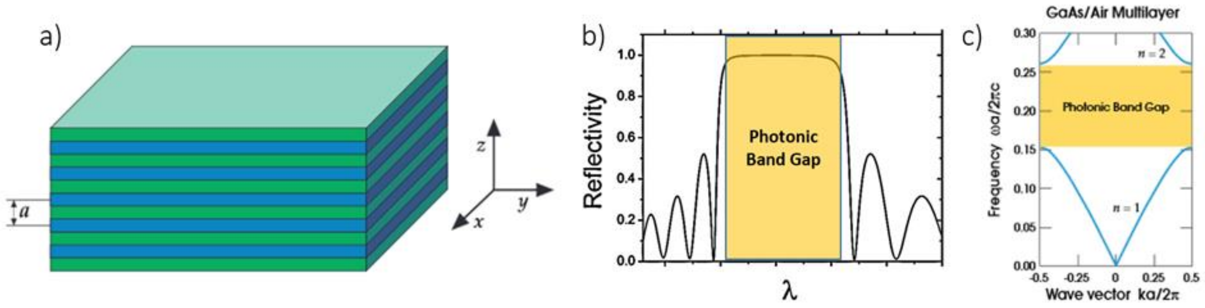

Figure 1.6. a) 1-D PhC or Bragg mirror with alternating high (green) and low (blue) dielectric constants over a period, a. b) Wavelength reflectance spectrum and c) dispersion relation of Bragg mirror shown in a). Figure adapted from [86].

Although no electromagnetic modes are allowed in the PBG, evanescent fields exponentially decay into the PBG. The evanescent field allows for the excitation of a surface or defect state that can be excited by removing, increasing, or truncating the optical thickness of a designated layer (Figure 1.7). In the case of the microcavity, the defect state was created by increasing the optical thickness of the cavity layer. These modes manifest themselves as a defect mode confined within the PBG as highlighted in the BSW dispersion relation in Figure 1.7c as an example. The BSW and microcavity are examples of a surface state and defect state, respectively. The modes of the dispersion relation are calculated by the master equation in Equation 1.10, as presented by Joannopoulos, et. al., where H(r) are the numerically solved magnetic field modes, ε(r) is the dielectric profile, ω is the angular frequency of light, and c is the speed of light [86].

$$\nabla \times \left(\frac{1}{\varepsilon(\mathrm{r})} \nabla \times \mathbf{H}(\mathbf{r})\right) = \left(\frac{\omega}{\mathrm{c}}\right)^2 \mathbf{H}(\mathbf{r}) \tag{1.10}$$

A 1-D PhC can be integrated within ridge WG to create the PhC nanobeam cavity shown in Figure 1.7b. In comparison to microcavities and ring resonators, PhC nanobeams demonstrate increased quality factor resonances and reduced modal volumes. Nanobeams are a linearly periodic array of rods or holes on a ridge WG creating a PBG [87,88]. The center of the nanobeam cavity contains a defect hole or filled-in hole that breaks the periodicity of the hole array creating the PBG and introduces a defect state. The cavity mode manifests itself as a sharp peak in the PBG in the transmission spectrum, highlighted in green in Figure 1.7d.

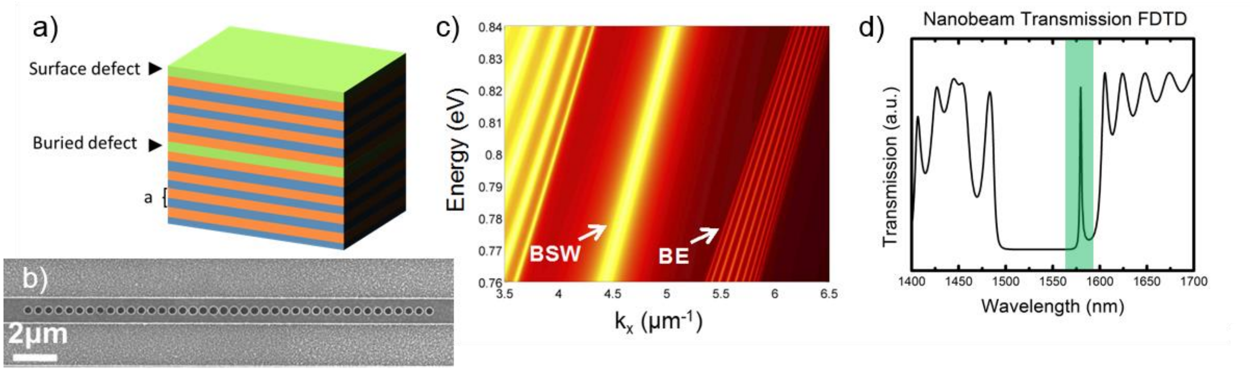

Figure 1.7. a) 1-D PhC showing surface and buried defect layers to excite a propagating mode confined by a PBG. b) PhC nanobeam etched into a ridge WG. c) The dispersion relation of the BSW surface state. d) Transmission spectrum of the PhC nanobeam shown in b) with nanobeam cavity resonance highlighted in green.

Multi-dimensional PhC configurations offer further flexibility in laterally (2-D) and completely (3-D) controlling the flow of light. Due to the nonstandard and challenging fabrication procedures of reported 3-D PhCs, research efforts have been primarily focused on 1-D and 2-D PhCs due to their versatility and compatibility with SOI WGs. An example of a 2-D PhC slab WG with defect is shown in Figure 1.8. The lattice constant or period of the 2-D rods or holes brings rise to an in-plane PBG while light is vertically confined by TIR. It has been shown that the hexagonal 2-D lattice creates a PBG for both TE and TM polarized sources and is known as a "complete PBG" as opposed to a square lattice that only supports a TM PBG [86]. In one of the simplest configurations, a slab WG and cavity can be formed by creating a line and point defect, respectively, although many other approaches have been used [89]. A line defect is created by removing or filling in a line of holes. This scenario is similar to the microcavity previously discussed. However, light is laterally confined by the PBG and total internal reflection occurs vertically. A ridge WG mode can be directly coupled to the 2-D PhC line defect [21]. A point defect created when a single hole is missing is called a Line1 (L1) defect and opens a new state within the PBG. Light can couple into this defect cavity and constructively interfere to create a high quality mode, similar to the ring resonator. Figure 1.8 shows an L3 cavity where three holes are missing [21,86].

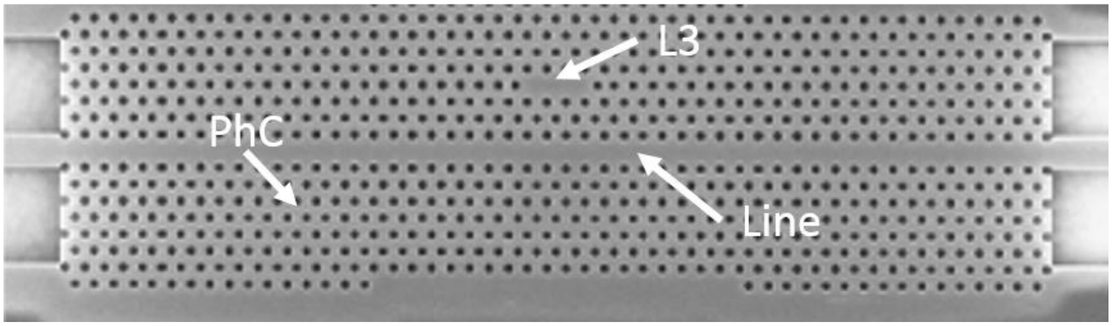

Figure 1.8. A SOI ridge WG coupled to a 2-D hexagonal PhC containing line and L3 cavity defects [21].

Ring resonator and PhC cavities structures are designed to excite strongly localized fields that facilitate strong light-matter interaction leading to highly sensitive devices in biosensing applications. These resonant structures have been extensively demonstrated in silicon and polymer WGs as biosensors, filters, and modulators, and a ring resonator based on BSW films has been theoretically reported [90]. Previous work in PSi has been limited to ridge WG and Mach Zehnder Interferometers (MZI) [28,30,91]. In this work, the ring resonators and PhC NBs are integrated in PSi for enhanced biosensing applications. Additionally, the tunability of PSi allows the first experimental realization of a BSW ring resonator in any material system.

1.5 Numerical Modeling

In this work, numerical software modeling techniques including transfer matrix method (TMM), rigorous coupled wave analysis (RCWA), and finite difference time domain (FDTD) are utilized to design and model the proposed PSi resonant films and devices. All PSi devices are modeled as effective mediums, as described in Section 1.2.2. The porous morphology is not included in simulations in order to reduce required mesh sizes for computationally efficient simulations.

TMM and RCWA algorithms are utilized to calculate reflectance and transmission spectra of PSi films in the prism and grating configuration, respectively. The TMM models 1-D multilayer films based on matrix calculations derived from Maxwell's equations and boundary conditions. The transfer matrix is a 2x2 matrix containing dielectric and thickness information of each layer, and the product at each layer interface is iteratively calculated. The Fresnel reflection and transmission coefficients can be extracted from the final transfer matrix and plotted over an angular or wavelength sweep [92-94]. The algorithm can be simply implemented as a MATLAB script and can quickly and efficiently compute spectra of very large multilayer films.

RCWA follows the identical algorithm of the TMM method. However, a scattering matrix is derived using Maxwell's equations in Fourier space. The components of the matrix are derived as a product of spatial harmonics in the plane wave domain. This derivation allows calculation of two dimensional periodic structures and is ideal for rapidly determining reflection and transmission spectra of multilayered films with periodic gratings [95-97]. Grating coupled WGs, BSWs, and 1-D and 2-D photonic crystals can be accurately modeled. RCWA is capable of modeling 1-D films but may be computationally inefficient when compared to the TMM.

The FDTD method is a simple algorithm capable of calculating optical characteristics of both finite periodic and aperiodic structures. Maxwell's equations are converted to finite difference equations that allow efficient discrete calculations of scattered fields within inhomogeneous devices made of dielectric, metal, or magnetic materials [98]. The dimensions and material properties of the structure of interest are the key input parameters. The structure is sampled into spatial intervals of a specified mesh size. The finite difference equations are calculated at each interval to monitor light interaction and field propagation within the structure [98,99]. The FDTD method is capable of generating reflection and transmission spectra as well as field and power profiles within the symmetric or asymmetric structures. Although complex structures such as the ring resonator and PhC cavities can be modeled, the algorithm is computationally expensive and may require long simulation times. Several commercial FDTD software packages are available with straightforward user interfaces.

1.6 Objectives and Dissertation Overview

The objective of this thesis is to implement ring resonator and photonic crystal nanobeam structures in PSi films for on-chip biosensing applications. These advanced photonic structures combine the strong light-matter interaction and multilayer versatility intrinsic to PSi films with the high quality factor and low modal volume advantages of resonant photonic devices.

In Chapter 2, the sensitivity and time response of microfluidic-integrated microcavity, WG, and BSW structures upon exposure to both large and small molecules is investigated. In Chapter 3, a novel Bloch surface and sub-surface wave PSi multilayer film is demonstrated that allows size selective detection of both large and small molecules by supporting both a surface wave mode and one or more guided modes within the multilayer PSi film. By facilitating large molecule detection via the Bloch surface wave, this PSi structure overcomes major limitations in the size and molecular weight of species that PSi sensors are capable of sensitively detecting. In Chapter 4, PSi ring resonators are demonstrated for the first time and exhibit a 40-fold sensitivity improvement over nonporous silicon-on-insulator ring resonator and nanobeam sensors. The ability to control some of the nonlinear properties of PSi rings is also shown in this chapter. In Chapter 5, the first experimental realization of a Bloch surface wave ring resonator is reported and is demonstrated in PSi. This new structure may open the door to new opportunities in integrated optics. A molecular sensing application is demonstrated as a first example. Chapter 6 discusses the integration of a PSi WG PhC nanobeam and how it overcomes the free spectral range challenges observed with PSi

WG ring resonators. Chapter 7 presents a concluding summary and future work. Overall, the ability to create multilayer PSi films and incorporate on-chip photonic devices enables the development of novel photonic resonator families that show particular promise for future lab-on-a-chip and sensor array devices.

CHAPTER 2

POROUS SILICON RESONANT THIN FILM SENSING

2.1 Motivation

Chapter 1 outlined the necessary requirements for a lab-on-a-chip diagnostics device such that it is highly sensitive, compact, accurate, easy-to-use, disposable or reusable, inexpensive, and compatible with both ambient and fluidic environments. Several current optical label-free biosensor designs do not meet these requirements and the applicability of these devices for point-of-care diagnostics is limited. Over the past decade, the inexpensive PSi material has become increasingly attractive for chemical and biomolecular sensing applications. The optical properties (e.g., refractive index) can be manipulated over a wide range and therefore various photonic structures can be fabricated using PSi. In particular, the strong light-matter interaction between target molecules and localized Bloch surface wave (BSW), waveguide (WG), and microcavity (μc) modes allow for highly sensitive, rapid read-out, compact sensors. Currently, PSi sensors have begun to be integrated with simple microfluidic systems for lab-on-a-chip architectures. This is a vital step in promoting micro-total-analysis systems that are cost-effective and may be measured efficiently and in real-time [60,100]. Two challenges that face PSi sensors are response time and molecular diffusion limitations. The former is limited by diffusion dynamics and binding kinetics in nanoscale pores while the latter leads to an inability to detect large molecules that cannot efficiently infiltrate inside the pores. The small molecule sensitivity, diffusion dynamics and binding kinetics performance of a PSi WG were recently investigated by Wei et al., finding an order of magnitude smaller diffusion coefficient and up to 4 orders of magnitude slower kinetic parameters in a PSi waveguide, depending on the size of the molecule, compared to sensing using a planar (non-porous) surface active region [60]. Nevertheless, it was concluded that molecular identification at near-real-time scales was possible without waiting for saturation regimes when all binding sites are filled.

In this chapter, sensitivity, response time, and target molecule size limitations of label-free PSi BSW, WG, and μc biosensors, all with microfluidic integration, are reported with related discussion of the challenges of real-time detection of both large (size >10 nm) and small (size <2 nm) molecules. The design of the grating-coupled PSi-BSW is introduced here, while a more detailed discussion is provided in Chapter 3. The designs of the grating-coupled PSi-WG [25] and PSi μc [52] biosensors follows previous work. The grating-coupled BSW and WG structures have the advantage that the thin active sensing regions confined by total internal reflection (TIR) to the upper surface of the structure allow for a rapid sensor response. Moreover, both of these structures support direct molecular interaction with the guided waves. In contrast, the PSi μc has a buried sensing region and promotes interaction of molecules with standing waves in the cavity region; however, the photonic crystal confinement of the mode does not require the addition of a coupling mechanism to overcome TIR such as the grating and thus reduces fabrication complexity of the device.

2.2 Sensor Fabrication

The PSi samples were fabricated by electrochemical etching of p-type (0.01 Ω·cm) Si(100) wafers. The Si is immersed and etched in a 15% ethanoic hydrofluoric acid solution. Varying current densities are applied as described in Table 2.1 for the three respective structures. The approximate pore diameters for the PSi layers range from about 12-25 nm [101]. In the table, d_{BSW}, d_{WG}, and d_{cavity} represent the thickness of the guiding layers or active sensing regions of the structures. The d_a and d_b layers are denoted as the low and high porosity layer thicknesses and are also denoted as the quarter-wavelength optical thickness layers of high (H) and low (L) refractive index, respectively, used for the Bragg reflectors in the μc and BSW structures. Thicknesses of the layers are determined by scanning electron microscopy (SEM) imaging and the refractive indices and porosities are estimated by fitting the reflectance spectra of single layer PSi films using transfer matrix code and the Bruggeman effective medium approximation. The BSW structure consists of an 11 period multilayer structure with a very thin top defect layer treated as the guiding layer: $(d_{BSW}L)(HL)^{11}$. The total thickness of the BSW structure is approximately 10 μm. The waveguide consists of the active sensing layer and a lower cladding layer. The total thickness of the WG structure is approximately 2 μm. The microcavity consists of a $(HL)^8(HLL)(HL)^{10}$ structure with a half wavelength thick cavity layer, d_{cavity}, located in the high porosity layer (i.e., low refractive index layer, L) of the ninth period. The depth of the cavity is approximately 2 μm from the surface and the total thickness of the μc structure is approximately 4.7 μm. Following anodization, the samples are placed in a 1.5 $mM \cdot L^{-1}$ potassium hydroxide (KOH) in ethanol solution for five minutes to widen the pores for the subsequent molecule infiltration. The samples are thoroughly rinsed with ethanol to remove any residual KOH within the pores that can present clogging and instability issues. The samples are then thermally oxidized at 500°C for five minutes in air in order to prevent damage or corrosion within the membrane caused by ambient or fluidic environments. The formed SiO_2 terminated surface also serves as the first step of surface functionalization for detection of target molecules by providing an interface between inorganic silicon and organic molecules. At this point, the μc sensor fabrication is complete. Due to the μc mode being confined by a photonic crystal periodic stack, the resonance can be excited by spectrophotometric measurements from the top side of the sample without the use of a coupling mechanism. To overcome TIR confinement of the WG and BSW modes, a coupling mechanism such as a prism, grating, or end coupler is required. Since the structures are integrated with a microfluidics channel, the use of a bulky prism is not feasible so grating couplers are designed for the respective devices by RCWA simulations. Grating couplers on the WG and BSW structures are fabricated using conventional electron beam lithography processing. Photoresist (ZEP 520A) is first spun at 6000 rpm on each sample, which results in a ~180 nm thick photoresist layer. The photoresist is subsequently patterned by using a Raith eLine EBL tool. Cross-sectional SEM images of the BSW, WG, and microcavity are shown in Figure 2.1.The BSW and WG grating periodicity are 1820 nm and 1590 nm, respectively, to efficiently couple light into guided modes within a measurable angular range. The gratings can be designed by using Equation 1.5. The WG or BSW n_{eff} is calculated using the effective index method or numerical eigenmode solvers such as MPB or Lumerical Mode Solutions. Additionally, the grating periodicity and filling fraction can be determined through iterative RCWA simulations. A reflectance intensity map varying angle and grating pitch is simulated, and the grating pitch with the highest coupling efficiency (% reflection) is chosen as the grating pitch. Similarly the fill fraction of the grating can be determined after the pitch is chosen. The effective index method and RCWA optimization procedure were utilized to maximize coupling efficiency for the WG and BSW grating pitch, respectively.

Structure	Layer	Refractive Index	Porosity	Thickness	Current Density	Time
BSW	d_{BSW}	1.79	64%	175 nm	5 mA·cm^{-2}	34 s
	d_a (H)	1.79	64%	340 nm	5 mA·cm^{-2}	63 s
	d_b (L)	1.24	83%	580 nm	48 mA·cm^{-2}	22 s
WG	d_{WG}	1.79	64%	345 nm	5 mA·cm^{-2}	65 s
	$d_{cladding}$	1.24	83%	1700 nm	48 mA·cm^{-2}	53 s
μc	d_a (H)	1.79	64%	110 nm	5 mA·cm^{-2}	14 s
	d_b (L)	1.24	83%	130 nm	48 mA·cm^{-2}	5 s
	d_{cavity}	1.24	83%	275 nm	48 mA·cm^{-2}	10 s

Table 2.1. Electrochemical etching parameters and physical characteristics of the PSi BSW, WG, and μc structures where the layers are as defined in the main text.

After samples are fabricated, a polydimethylsiloxane (PDMS) flow cell is adhered to the porous surface. The flow cell template is fabricated by soft lithography techniques to create a 10mm×4mm×0.2mm SU-8 mold. The pre-polymer solution of PDMS is mixed 10:1 with a curing agent. The polymer is then degassed by a vacuum and solidified by placing the mask and polymer in an oven at 80°C for 6 hours. Finally, the PDMS flow cell is cut and removed from the mask and holes are punched for the inlet and outlet tubing. Attachment of the PDMS membrane to the oxidized PSi surface was unsuccessful when solely using treatment of the flow cell with oxygen plasma [102]. The flow cell is treated with oxygen plasma only to promote a hydrophilic membrane. PDMS curing agent is necessary to glue the flow cell to the SiO_2 surface. A thin layer of the curing agent is spun on a glass microscope slide at 3000 rpm and placed onto the oxygen plasma cleaned flow cell. ZEP 520A surrounding the grating region is manually removed using acetone to ensure better adhesion. The device is clamped between two glass slides to prevent damage and baked overnight at 70°C for curing. Inlet and outlet microtubes are attached and solutions are introduced to the porous sensor using a Harvard Apparatus picoplus syringe pump at 0.1 $\mu L \cdot min^{-1}$. A completed microfluidic integrated grating-coupled PSi device is shown in Figure 2.1(d) [60].

The μc spectral shift is measured using an Ocean Optics USB4000 VIS-NIR miniature fiber optic spectrometer. Measurements are taken every 30 seconds with a spectral resolution of 1.5 nm. For the case of the grating coupled WG and BSW, angle resolved reflectance measurements are performed in a Metricon 2010/M instrument operated in the variable angle monochromatic fringe observance (VAMFO) mode. The prism is removed, from the Metricon, and a custom sample holder is mounted so that light is incident on the grating [68]. A TE-polarized 1550nm laser was used as the light source. The Metricon tool allows for one measurement every 105 seconds over a dynamic range of 20-55° with an angular resolution of 0.002° based on the parameters of the rotation stage and detection capabilities.

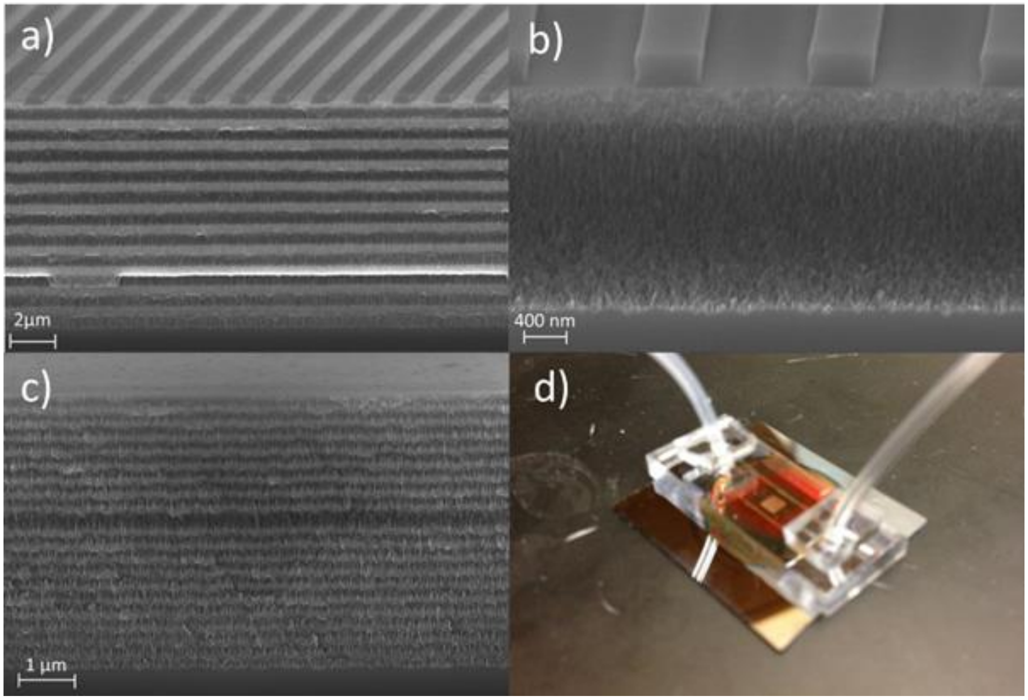

Figure 2.1. Cross sectional SEM images of a) grating-coupled PSi-BSW, b) grating-coupled PSi-WG, and c) PSi-μc. A complete microfluidic integrated device is shown in d) [66].

2.3 Surface Functionalization

The two small molecules exposed to the three PSi sensor structures were selected based on their ubiquitous usage in PSi sensor functionalization protocols: 3-aminopropyltriethoxsilane (3-APTES, 0.8 nm) and Sulfosuccinimidyl-4-(N-maleimidomethyl) cyclohexane-1-carboxylate (Sulfo-SMCC, 1.2 nm). The large molecule chosen for the study is a 40- base 5'thiol-modified DNA oligo (5'-TAG-CTA-TGG-TCC-TCG-TTA-GCT-ATG-GAA-TTC-CTC-GTA-GGC-C 3') of nominal length 13.2 nm that has been previously shown to be too large to infiltrate into porous membranes with ~20 nm diameter pores [43]. Note that the 3-APTES and Sulfo-SMCC serve as linker molecules to immobilize thiol-modified DNA so the small and large molecule studies are performed in succession. Moreover, DNA oligos have proven to be effective as probe molecules for the detection of complimentary nucleic acid sequences and as aptamers for the selective capture of a variety of other molecules so these studies are directly applicable for sensor applications [103].

The analyte solutions are prepared as follows. A 4% 3-APTES solution is dissolved in water and methanol, and Sulfo-SMCC is prepared with 4-(2-hydroxyethyl)-1-piperazineethanesulfonic acid (HEPES) buffer in a 2.5 mg·mL-1 solution. For the large molecule solution, 100µM of 40mer DNA in HEPES buffer is mixed with the reducing agent, tris(2-carboxyethyl)phosphine (TCEP) in a 1:1 mixture. TCEP with a concentration of 0.07 mg·mL^{-1} is prepared in a water/methanol solution. The 3-APTES, Sulfo-SMCC, and DNA solutions are injected into the flow cells attached to each sensor, as detailed below. With the exception of the DNA solution, all other solutions are injected at 0.1 µL·min^{-1}. The DNA solution is only statically measured due to cost of materials. HEPES buffer and a water/methanol solution are used as rinsing steps in between molecule attachments to flush away non-specifically bound molecules.

First, water/methanol is injected into the flow cell for 10 minutes and is used as the ambient media to determine the initial reference resonance angle or wavelength prior to molecule introduction. Next, 3-APTES is continuously injected for 20 minutes. The samples are then thoroughly flushed with water/methanol for 10 minutes, removed from the prism coupler sample holder, and thermally annealed at 110°C for 15 minutes to promote cross-linking. Water/methanol and HEPES buffer solutions are then injected in succession for 10 minutes each to enable the necessary reference measurement to quantify 3-APTES attachment and to prepare for the subsequent Sulfo-SMCC attachment, respectively. Next, the Sulfo-SMCC solution is injected continuously for 2 hours. HEPES buffer is then injected and flowed for one hour to remove unbound species. Again, the water/methanol solution is injected for 10 minutes to provide the necessary reference measurement. Finally, the DNA solution is injected and incubated for 1 hour, followed by a 30 minute HEPES rinse to remove unattached oligonucleotides and a water/methanol rinse for 10 minutes to provide the last necessary reference measurement.

2.4 Device Measurement

The μc spectral wavelength shift is measured using an Ocean Optics USB4000 VIS-NIR miniature fiber optic spectrometer. Measurements are taken every 30 seconds with a spectral resolution of 1.5 nm. Prior work has shown that the structure is very sensitive to small molecules, but sensors with sensing regions close to the top surface have been generally favored due to the concern over the time required for molecules to diffuse into such a thick structure [64].

Angle resolved reflectance measurements of the BSW and WG are performed in a Metricon 2010/M instrument operated in the variable angle monochromatic fringe observance (VAMFO) mode. A TE-polarized 1550 nm laser was used as the light source. The Metricon tool allows for one measurement every 105 seconds over a dynamic range of 20-55° with an angular resolution of 0.002° based on the parameters of the rotation stage and detection capabilities. At the proper coupling angle satisfying Equation 1.5 a resonance appears in the reflectance spectrum. A shift in the coupling angle is detected when molecules are introduced to the double layer waveguide structure.

2.5 Sensitivity Characterization

When molecules infiltrate the PSi devices, the effective refractive index of the PSi increases, leading to a measureable shift in the resonance angle (BSW and WG) or wavelength (μc). Moreover, molecules attached on the surface of the BSW structure will also change the effective index of the BSW mode, causing a shift in the resonance angle. Importantly, the active sensing region of the PSi-BSW is at the surface of the structure where the propagating field is confined, promoting a fast sensor response to both small and large molecules.

The sensitivity of the devices is characterized by eigenmode solution simulations for the PSi BSW and WG and transfer matrix simulations for the μc in order to predict the sensor performance. Simulations investigate effects of small molecules that change the effective medium of the porous layers and large molecules that can only attach at the surface of the sensor. Figure 2.2 (a) and (b) depict the near field intensity distribution of the BSW and WG structures, respectively, as simulated using MIT Photonic Bands (MPB) and Mas Eventos Electrodinamicos Posible (MEEP) FDTD solver. Table 2.2 presents the field confinement percentage within two regions of each sensor: 1) the guiding layer where small molecules diffusing into the pores interact with the strongly confined field and 2) the first 20 nm above the surface of the structure where large molecules that cannot enter the pores interact with the evanescent field. Note that the thickness of the BSW guiding layer is 175 nm while the guiding layer of the WG is 345 nm. The effects of both an air ambient and a fluidic environment are presented. Based on the results shown in Table 2.2, the WG is expected to provide a 1.6 times greater field confinement in the guiding layer and therefore a 1.6 times increased sensitivity for detection of small molecules in both air and water environments compared to the BSW structure. In contrast, the more prominent evanescent tail of the BSW mode allows for stronger fields near the surface and is predicted to lead to a 2.6 fold increased detection sensitivity for larger molecules in a fluidic solution compared to the WG. A slightly lower sensitivity enhancement for the BSW is achieved in air (2.4x). A Bruggeman effective medium approximation was used to estimate the refractive index of the porous silicon layers in the water environment [44].

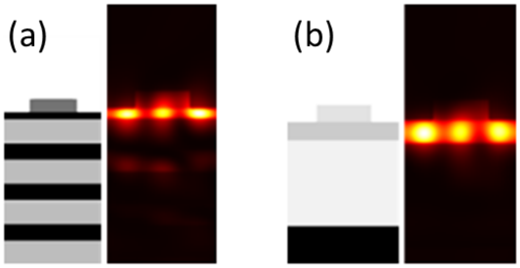

Figure 2.2. Near-field electric field distribution of a) PSi BSW and b) PSi-WG [66].

	BSW air	WG air		BSW water	WG water
Guiding layer	39.5%	63.8%		44.0%	70.0%
20 nm above surface	22.0%	9.33%		18.3%	6.97%

Table 2.2. Field confinement factor (in percentages) of BSW and WG in guiding layers and in the near-surface region for both air and water ambient.

The μc structure is analyzed by transfer matrix simulations. The cavity resonance wavelength is found to shift significantly only when the refractive index of the cavity layer or immediately adjacent layers change. Small resonance shifts occur for refractive index changes in other layers of the μc structure, but no resonance shift is theoretically observed for a refractive index change at the surface of the structure. Figure 2.3 illustrates the resonance shift due to a change in refractive index, $\Delta n = 0.03$, as a function of depth within the μc structure. A resonance shift is not observed until the refractive index change occurs within the third period of the structure. The largest resonance shift occurs when molecules are simulated to be present within the cavity layer. No resonance shift is observed for the theoretical infiltration of molecules within the last five periods of structure. This phenomenon can be explained by considering the field profile in the μc. The strongest field exists in the cavity with only evanescent wave penetration into the nearby layers. Hence, it is anticipated that only small molecules infiltrating the pores and not large, surface-bound molecules will be detected using the PSi μc structure.

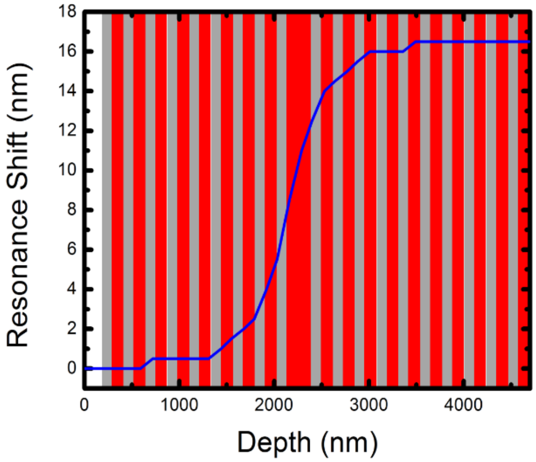

Figure 2.3. Simulated μc resonance shift as the refractive index is changed, Δn = 0.03, progressively at different depths within the structure. No resonance shift results for the theoretical infiltration of molecules within the first three and last five periods of the structure. The highest detection sensitivity is observed for molecule attachment within the cavity region. The shaded vertical bars represent the extent of each layer of the μc structure [66].

2.6 Detection of Small and Large Molecules in a Fluidic Environment

The sensing performance of the PSi BSW, WG, and μc to the small and large molecules are shown in Figures 2.4, 2.5, and 2.6, respectively. Parts (a)-(c) of each figure depict the real-time shifts of the resonance position during injection of each of the molecules into the flow cells attached to the sensors. The circular data points correspond to the resonance angles (BSW and WG) or wavelengths (μc) at different times. The resonance positions are determined based on the measured reflectance spectra and finding the local maximum for the BSW and WG and by fitting the μc resonance with a Lorentzian curve and finding the local minimum. For the small molecule injections, a rapid increase in the resonance angle or wavelength is observed followed by a slower increase approaching a saturation condition. The fast initial change is largely due to the diffusion and volume infiltration of the analyte solution, which contains a different refractive index than the rinse solution. Attachment of molecules leads to a small additional shift. A near constant concentration is assumed within the porous layers when the resonance equilibrium is achieved. All three sensors exhibit a similar, relatively quick response of less than two minutes upon the infiltration of the smallest molecule, 3-APTES (length = 0.8 nm). For the angle-resolved measurement in the Metricon tool, the equilibrium condition is reached within the first measurement point due to the relatively slow speed of the rotation stage. The slightly larger Sulfo-SMCC molecule (length = 1.26 nm) also easily penetrates the porous matrix but with a longer diffusion time as the resonance position settles in less than 20 minutes. In contrast, no significant resonance change is observed after DNA injection. This is likely due to the lack of volume infiltration of the large DNA molecules.

The square blue data points on parts (a)-(c) of Figures 2.4-6 correspond to the resonance angles or wavelengths after the reference water/methanol rinses. As discussed in Section 2.5, the angular shift due to molecular attachment is determined by comparing the resonance position before and after molecule injection when the water/methanol solution is present in the flow cell and all unbound species have been rinsed away. The magnitude of this angular shift directly correlates to the quantity of bound molecules on the sensor. For Sulfo-SMCC and DNA detection, the analyte solution is in HEPES buffer, which has a lower refractive index than the water/methanol solution; hence, the circular data points on parts (b) and (c) of Figures 2.4-6 are at lower angle or wavelength than the square data points. Note that the attachment times reported in Section 2.3 have not been optimized, and further infiltration optimization might lead to a larger resonance shift or more rapid detection of the molecules.

Part (d) of Figures 2.4-6 shows the reflectance spectra measured in the reference water/methanol solution after attachment of each molecule. For all sensor structures examined, there is a clear resonance shift after the introduction of the two small molecules, but only the BSW shows a measurable shift for large molecule attachment. Note that there are two curves for 3-APTES for the μc sensor in Figure 2.6. After removing the sample from the measurement setup for annealing, there was a slight change in the position of the sample with respect to the incident laser beam and hence the resonance wavelength changed due to slight non-uniformities in the sample and not due to the annealing step itself.

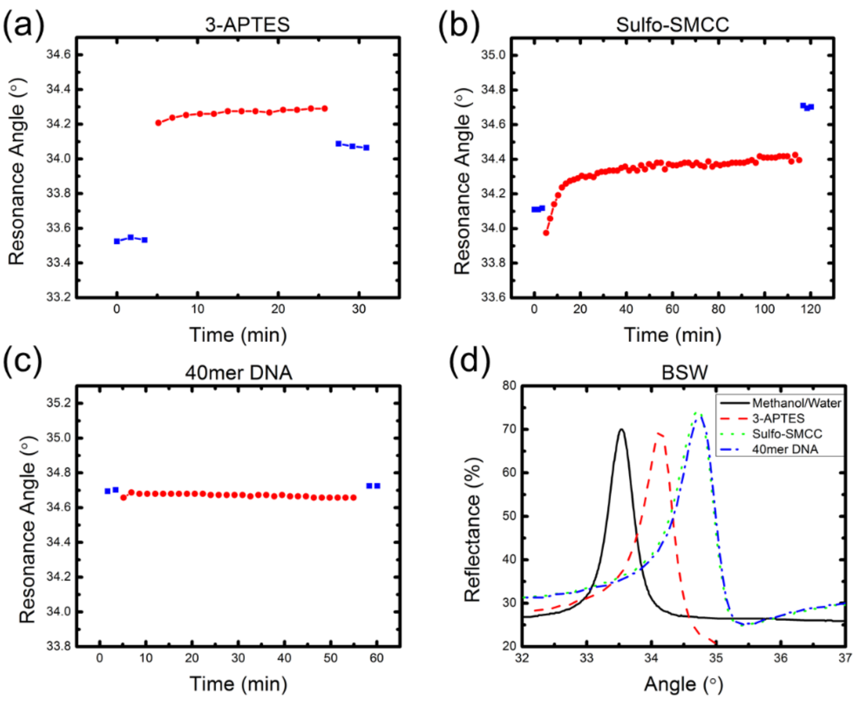

Figure 2.4. BSW real-time measurements upon exposure to (a) 3-APTES, (b) Sulfo-SMCC, and (c) 40mer DNA. The red circular data points are taken in the analyte solution and the blue square data points are taken in a reference water/methanol solution. (d) Static reflectance measurements indicating the resonance positions after each functionalization step [66].

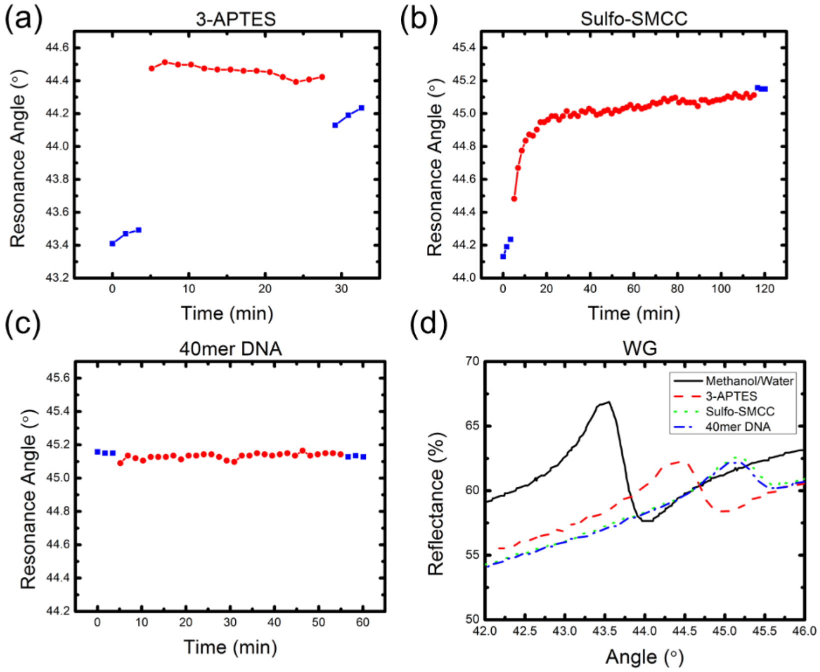

Figure 2.5. WG real-time measurements upon exposure to (a) 3-APTES, (b) Sulfo-SMCC, and (c) 40mer DNA. The red circular data points are taken in the analyte solution and the blue square data points are taken in a reference water/methanol solution. (d) Static reflectance measurements indicating the resonance positions after each functionalization step [66].

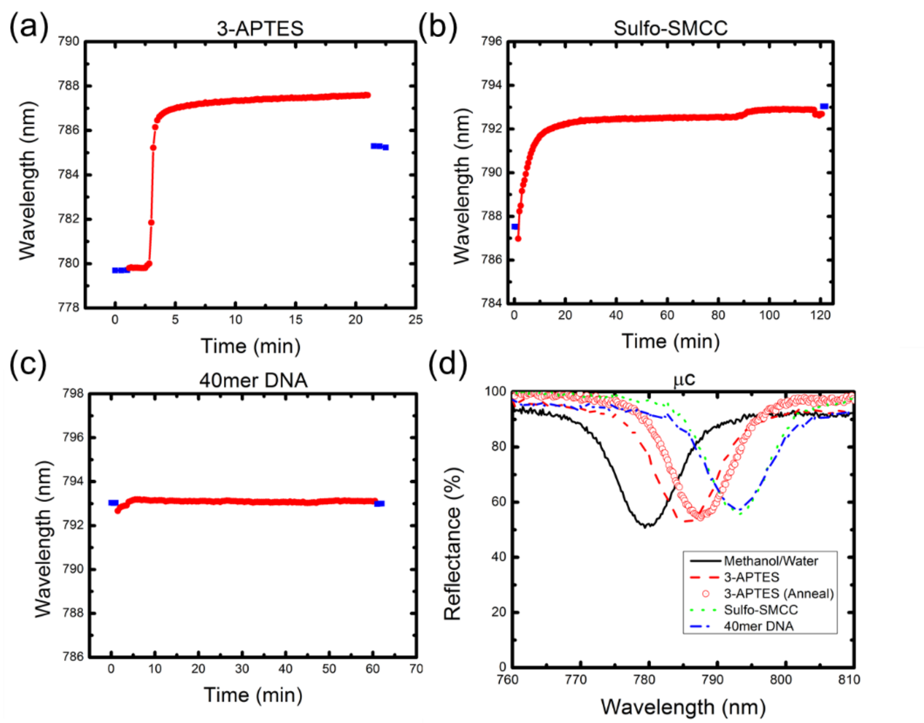

Figure 2.6. μc real-time measurements upon exposure to (a) 3-APTES, (b) Sulfo-SMCC, and (c) 40mer DNA. The red circular data points are taken in the analyte solution and the blue square data points are taken in a reference water/methanol solution. (d) Static reflectance measurements indicating the resonance positions after each functionalization step [66].

A summary of all the experimentally measured resonance shifts are shown in Table 2.3. The angular shift of the WG and BSW were converted to wavelength shifts by using the following difference equation derived from Equation 1.5, where Δλ is the wavelength shift, Λ is the grating pitch, θ is the incident angle, and Δθ is the angular shift.

$$\Delta\lambda = \Lambda \cdot \cos(\theta) \cdot \Delta\theta \qquad 2.1$$

The FWHM of the resonances for each sensor structure plays a significant role for the structure and is a motivator for creating sharp spectral resonances with ring resonators and PhC cavities. The FWHM of the WG was found to suffer the largest increase when the ambient medium was changed from air to a liquid environment. Fluidic and molecular infiltration into the pores causes a different refractive index change in PSi layers with different porosity, as described by the

Bruggeman effective index approximation: higher porosity layers experience a larger refractive index change than lower porosity layers. Confinement of light in the WG becomes significantly weaker with the reduced index contrast at the interfaces both above and below the guiding layer. However, the BSW, with light partially confined by the photonic band gap of the Bragg mirror below the guiding layer, and the μc, with light completely confined by the photonic band gap of the surrounding Bragg mirrors, are less susceptible to confinement decay caused by the reduced index contrast from liquid infiltration. The multilayer Bragg mirror can provide strong confinement with a reduced index contrast in the constituent layers if there are a sufficient number of periods present in the mirror structure. Our PSi-μc has a large FWHM of approximately 9 nm. The design could be further optimized; prior reports suggest that cavity linewidths below 1 nm are achievable using a temperature controlled electrochemical etching technique. [104]. Notably, the detection of small molecules (< 2 nm) is not affected by the thickness or depth of the active sensing region, as the diffusion times are comparable between the three sensor structures. For the large molecule detection, Table 2.3 shows that only the BSW sensor gives a measurable and reliable response. The BSW mode exhibits a resonance shift of 0.03° when surface bound DNA molecules are attached. Compared to the measured resonance shifts for small molecule attachment, the smaller shift for large molecule attachment is attributed to the reduced surface area available for surface sensing when molecules do not infiltrate the pores. However, the large molecule detection sensitivity for the BSW is comparable to previous planar SOI WG surface sensing experiments [25].

	Resonance shifts (Angle/Wavelength)		
	3-APTES	Sulfo-SMCC	40mer DNA
BSW	0.58° / 15.27 nm	0.59° / 15.35 nm	0.03° / 0.78 nm
WG	0.76° / 15.30 nm	0.76° / 15.11 nm	-0.01° / -0.19 nm
μc	-- / 5.6 nm	-- / 5.8 nm	-- / 0.0 nm

Table 2.3. Measured resonance shift of the PSi BSW, WG, and μc for the detection of two small molecules, 3-APTES and Sulfo-SMCC, and one large molecule, 40mer DNA.

2.7 Summary

A grating-coupled PSi-BSW integrated with a with microfluidics flow cell has been demonstrated as an effective biosensor that provides similar sensitivity as the PSi WG in detection of small molecules in a liquid solution and the capability to detect large molecules that only bind to the surface and do not infiltrate the pores. The BSW structure provides significantly higher field strength in the cover region near the surface of the structure, which allows detection of surface bound large molecules that cannot be effectively detected using other traditional resonant PSi sensor structures. All three PSi thin film sensor structures investigated in this work (BSW, WG, and μc) exhibited similar detection capabilities for small molecules. Moreover, all three structures can be easily implemented in a real-time sensing device, although detection of molecules in a liquid environment reduces the effective index change of the sensors upon molecular binding, which reduces the detection sensitivity compared to measurements in air. Overall, PSi sensors integrated with microfluidic membranes have great potential for fast, portable, highly sensitive, label-free lab-on-chip systems for point-of-care diagnostics.

In the next chapter, we utilize the results of this chapter to develop a novel thin film structure that concatenates the surface sensitivity of the BSW with the high internal sensitivity and filtration properties of the WG and μc. The creation of additional defect layers near the surface but within the multilayer regions of the BSW structure creates a device with unique surface and sub-surface modes that allow selective detection of both small and large molecules within the same device.

CHAPTER 3

BLOCH SURFACE AND SUB-SURFACE WAVES

3.1 Introduction

In PSi, large surface area, arising from the presence of nanoscale pores, allows for improved sensitivity to biomolecule interactions, while tunable pore dimensions (~2 nm to >100 nm) enable size-selective detection and filtration of larger contaminant species [43]. PSi sensors have been demonstrated for the detection of larger molecules such as bovine serum albumin (8 nm width) and anti-MS2 antibodies (15 nm width) [57,105]. However, molecules approaching the average pore diameter clog the pore and hinder molecular infiltration, which significantly deteriorates the transduced signal. For example, it has been shown that 40 base DNA (~13 nm in length) cannot efficiently infiltrate 20 nm pores [43,84]. Hence there is a significant challenge in detecting biological entities such as viruses, bacteria, and blood cells that typically have sizes much larger than those of the pores. Alternative measurement techniques for the detection of surface bound molecules on PSi include monitoring fluorescent labels and changes in reflectance intensity for the detection of MS2 bacteriophage [105] and E. coli bacteria [106], respectively. However, emerging interest in lab-on-a-chip technologies has placed focus on label-free refractometric based sensors in order to avoid the additional expense of fluorescent labels. In addition, refractometric sensing configurations are a popular choice due to the compact size, small active sensing region, ability to transduce molecular interaction with an electric field into a refractive index change, and ability to array and multiplex devices allowing several biosensors on a single chip. For example, silicon-on-insulator (SOI) waveguides (WG) and surface plasmon resonance structures have been commercialized as label-free refractometric sensing devices; these devices utilize evanescent fields to detect refractive index changes due to the attachment of surface bound molecules of all sizes [20,107]. The advantage of the PSi WG, compared to these evanescent wave-based sensing devices, is the demonstrated sensitivity which is an order of magnitude greater than SOI WGs due to the direct interaction of small molecules with the guided field inside the porous layer. However, surface bound large molecules present a detection challenge in PSi WGs due to the weak evanescent fields at the surface [25,66,84].

As shown in Chapter 2, the BSW structure holds great promise for sensitively detecting large molecules on the surface of the sensor while the WG and μc showed the greatest response to small molecules. In this chapter, a novel label-free method for size-selective sensing of both small (<2nm) and large (~10nm) low molecular weight molecules (<15 kDa) using grating-coupled BSW and Bloch sub-surface wave (BSSW) optical modes of a PSi multilayer is presented. The PSi BSW/BSSW biosensor offers the possibility to uniquely detect both small molecules that infiltrate the pores and large molecules attached to the sensor's surface [84]. The BSW mode, as discussed in Chapter 1, is a surface state excited within the truncated defect layer at the surface of a multilayer Bragg mirror, and has been previously reported in PSi sensing applications [61,64,77,80]. The BSW mode is confined on one side by the multilayer mirror and on the other side by total internal reflection at the air interface. The novel BSSW mode, which is described in detail later in this chapter, is confined by a step or gradient refractive index change within the multilayer and can selectively detect small molecules attached within the pores with an enhanced sensitivity (>2000 nm/RIU) in comparison to band edge modes of the multilayer, microcavities, or traditional WG modes [61,66,84]. The BSSW mode utilizes a near-surface PhC defect, similar to the buried μc defect, to achieve rapid, highly sensitive detection of only small molecules. The BSW and BSSW modes are each manifested as a distinct resonance peak in the reflectance spectrum, and the angular shift of each peak can be used to quantify the number of molecules attached to the sensor. By utilizing a one-dimensional integrated grating at the surface of the structure, coupling can be achieved by far field excitation at a unique resonant angle [25,65] while also eliminating the need for a bulky prism and air gap tuning that would preclude potential microfluidics applications [45].

In this chapter, the first fabricated grating-coupled PSi-BSW/BSSW platform is benchmarked against a grating-coupled PSi-WG [25] and demonstrates a larger sensitivity to both small and large molecules. Next, the device optimization of a step index and an optimized gradient index PSi BSW/BSSW biosensor are presented. Large molecule detection is demonstrated with M13KO7 bacterial viruses, 60 nm diameter latex nanospheres, and 40mer DNA strands that cannot efficiently enter the pores. The small molecules used to demonstrate the size selective detection scheme are 3-aminopropyltriethoxysilane (APTES), Sulfo-SMCC, and gluteraldehyde (GA).

3.2 Materials and Methods

3.2.1 Fabrication of Initial BSW/BSSW and WG Sensors

The initial BSW/BSSW porous silicon structures (hereafter referred to as initial-BSW/BSSW) and benchmarking WGs were fabricated by electrochemical etching of p+ (~0.01 Ω cm) Si(100) wafers. By placing the silicon in a solution containing 15% HF in ethanol and varying the applied current density and duration, the resulting PSi layer thickness and porosity can be tuned. Table 3.1 shows the current densities and times used to fabricate the structures used in this work. A two second etch break (no current applied) is employed between the formation of each layer. The etching parameters were chosen based on rigorous coupled wave analysis (RCWA) simulations to yield structures with clear optical resonances [95]. The etched samples were placed in a 1.5 $\mathrm{mM \cdot L^{-1}}$ KOH in ethanol solution for five minutes to widen the pores for enhanced molecule infiltration. The samples were then thermally oxidized in air ambient at 500°C for five minutes. The nominal refractive index of each layer is approximated by fitting the measured reflectivity spectrum of the layer with a thin film simulation that incorporates the scanning electron microscopy (SEM) measured thickness of the layer. For the initial-BSW/BSSW sensor, reflectance spectra of the entire structure were used to fit the multilayer refractive index gradient that gives rise to the BSSW mode. The refractive index gradient was linearly varied from n_{i1}=1.62 – 1.72 and n_{i2}=1.22 – 1.26 for the low current density and high current density layers, respectively. In this first demonstration of the BSW/BSSW sensor, it was found that the combination of standard etching, brief KOH treatment, and oxidation produced a natural and reproducible gradient in the optical properties of the multilayer. We postulate that the dominant contribution to the natural gradient refractive index arises from the diffusion time of the KOH and the duration of KOH exposure to the PSi membrane. This hypothesis is supported by additional tests performed on initial-BSW/BSSW samples with different KOH exposure times for which the BSSW resonance was either not visible or shifted to different angles. The fabrication is optimized in the next section where the necessary refractive index profile is formed by appropriately tuning the PSi etching conditions.

Structure	Layer	Current Density	Time	Refractive Index	Thickness
BSW/BSSW	d_{01}	5 mA/cm^2	34 s	Gradient from 1.62 to 1.78	175 nm
	d_{i1} for i = 1 to 10	5 mA/cm^2	63 s		340 nm
	d_{i2} for i = 0 to 10	48 mA/cm^2	22 s	Gradient from 1.22 to 1.26	580 nm
WG	d_{wg}	5 mA/cm^2	65 s	1.79	345 nm
	$d_{cladding}$	48 mA/cm^2	53 s	1.24	1700 nm

Table 3.1. Electrochemical etching parameters used for device fabrication

The grating couplers were fabricated by electron beam lithography (EBL). ZEP 520A resist was spun at 6000rpm to create a ~300 nm thick layer and then patterned using a Raith eLine EBL tool. The WG and BSW couplers have grating pitches of Λ_{WG}= 1590 nm and $\Lambda_{BSW/BSSW}$ = 1820 nm, respectively. After development, the grating duty cycles were measured to be approximately 66% (air: silicon).

3.2.2 Optimized Fabrication of PSi BSW/BSSW Devices

As will be discussed in Section 3.3.1, the BSW/BSSW modes can be excited in two different structures called the step and gradient configurations. In Section 3.2.1, the gradient configuration was implemented through the natural index variability of the fabrication procedure. This section describes the fabrication of optimized step and gradient structures (hereafter referred to as optimized-BSW/BSSW) used after the initial discovery and analysis of the BSW/BSSW device. The step and gradient refractive index profiles are created during the electrochemical etching of p+ (~0.01 Ω•cm) Si (100) in a 15% hydrofluoric acid solution. The number of periods of the multilayer and the depth of the step and gradient refractive index layers were determined based on transfer matrix and rigorous coupled wave analysis (RCWA) simulations. The optimized-BSW/BSSW multilayer contains periods of alternating high (H) and low (L) refractive index layers with the first layer being truncated as shown in the cross-sectional scanning electron microscope (SEM) image in Figure 3.1a. Etch parameters for each H layer of the step and gradient index profiles are described in Figure 3.1b and 3.1c, respectively, where the top number is the current density in mA/cm^2 and the bottom number is the etching duration in seconds. All L layers are etched with a 48 mA/cm^2 current density for 22 s. The samples are then placed in a 1.5 mM·L^{-1} potassium hydroxide in ethanol solution for five minutes and oxidized for five minutes at 500°C in air. Gratings of pitch 1820 nm and 1650 nm are patterned onto the gradient and step index optimized-BSW/BSSW structures, respectively, via electron beam lithography on a 250nm thick ZEP 520A photoresist. The indices and thicknesses shown in Figure 3.1b and 3.1c were determined after fabrication through SEM images and by matching measured angular reflectance spectra with RCWA simulations. The field intensities shown in Figure 3.1b and 3.1c will be discussed in Section 3.3.4.1.

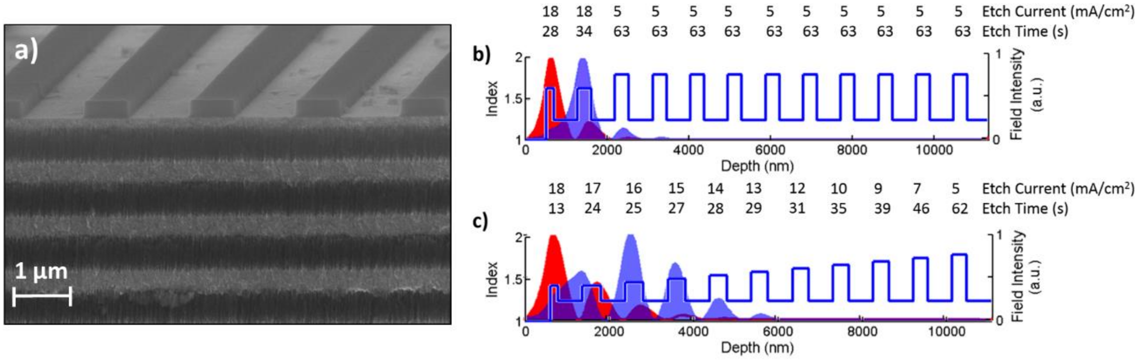

Figure 3.1. (a) SEM cross-sectional image of BSW/BSSW sensor. Refractive index profiles of (b) step and (c) gradient index BSW/BSSW sensors where the numbers shown above each layer represent the etch current (mA/cm^2) and etch time (s), respectively [108].

3.2.3 Measurement Technique.

The reflectance spectra of the BSW/BSSW and WG structures were measured using a Metricon Model 2010/M Prism Coupler. In the case of the grating coupled devices, the prism was removed to allow for far-field coupling. A 1550 nm TE polarized laser was used as the light source in the variable angle monochromatic fringe observance (VAMFO) mode. A depiction of the setup is illustrated elsewhere [25]. A resonance condition is distinctly excited when the effective index of a BSW or BSSW mode is matched by the coupling conditions of either a prism or diffraction grating. Prism coupling is compatible with existing surface plasmon resonance biosensing instrumentation. Grating coupling allows for more compact devices, which could be used for point of care diagnostics with microfluidics integration [60].

3.2.4 Large 40 mer DNA Functionalization

The initial-BSW/BSSW device was demonstrated for the detection of small linker molecules and a large 40mer DNA sequence as a size selective proof of concept. Each sample was soaked in a 4% 3-aminopropyltriethoxysilane (3-APTES) solution in methanol and water for 20 minutes, followed by a soak in methanol for 10 minutes to remove the excess silane. Although 3-APTES multilayers are difficult to prevent [109], the 10 minute methanol soaking procedure enables a consistent attachment of the molecule. The samples were then thermally annealed at 100°C for 10 minutes to promote cross linking between the surface silicon oxide and amino group. A 2.5 $mg \cdot mL^{-1}$ Sulfosuccinimidyl-4-(N-maleimidomethyl)cyclohexane-1-carboxylate (Sulfo-SMCC) in 4-(2-hydroxyethyl)-1-piperazineethanesulfonic acid (HEPES) buffer solution was incubated with the samples for 2 hours at room temperature, followed by a one hour soak in HEPES solution to remove excess material. Then, 100 μM DNA, (5'-TAG-CTA-TGG-TCC-TCG-TTA-GCT-ATG-GAA-TTC-CTC-GTA-GGC-C 3'), was prepared in HEPES buffer and then mixed with the reducing agent, TCEP (tris(2-carboxyethyl)phosphine) (Pierce) in a 1:1 mixture of methanol and water. The samples were soaked in the 50 μM DNA mixture for one hour, followed by a 30 minute soak in HEPES buffer to remove unattached oligos.

3.2.5 Latex Nanosphere Functionalization

Size-selective molecular detection using the optimized-BSW/BSSW structures was demonstrated using the small chemical molecule, APTES (size ≈ 0.8 nm), and large, 60 nm carboxyl latex nanospheres. A 4% APTES solution was prepared in methanol and water and an aliquot was placed on the PSi sample for 10 minutes. The sample was subsequently immersed in methanol for 10 minutes to rinse away excess APTES molecules not attached to the PSi and then thermally annealed for 10 minutes at 150°C. The sample was then rinsed with methanol to remove any remaining unbound APTES molecules. A 4% w/v solution of carboxyl terminated latex nanospheres (Invitrogen™) was placed on the optimized-BSW/BSSW sensor for one minute followed by a thorough methanol and DI water rinsing. Attachment and quantification of the small and large species were determined by monitoring the angle-resolved reflectance spectrum in between molecular attachments. The attachment of the nanospheres was additionally verified by SEM imaging as shown in Figure 3.2a. No spheres were observed to penetrate the porous matrix in cross-sectional images (Figure 3.2b).

3.2.6 M13KO7 Bacteriophage Functionalization

Viruses are infectious agents that can cause disease in humans, plants and animals. Antibodies are typically used in immunoassays to detect viruses in biological samples. The M13KO7 bacterial virus was used as a model system to determine if the large (~2μm length; 16,400kDa) M13KO7 could be directly bound to and detected on the PSi optimized-BSW/BSSW sensor surface. The M13KO7 bacteriophage is a low cost, readily available, nonhazardous E. Coli bacterial virus that can be readily detected using commercially available antibodies. [18, 19]. The virus was covalently cross-linked to the optimized-BSW/BSSW surface via APTES and GA linkers. APTES was attached as described in Section 3.2.5. GA is a homobifunctional cross-linker that can bind to and covalently link molecules through their free amines. A 2.5% GA in phosphate buffered saline (PBS) buffer solution was used to cross-link the APTES free amines on the sensor surface to the free amines on M13KO7 suspended in solution on the sensor surface. After a 30 minute GA incubation step, a 1% sodium cyanoborohydride (Aldrich) in PBS buffer solution was applied, followed by 30 minute incubation step to stabilize the Schiff base bonds formed during GA cross-linking [20]. The M13KO7 (0.32mg/ml carbonate/bicarbonate buffer, pH~10) was diluted to a final concentration of 32 μg/ml in PBS buffer (final pH ~9.5) and applied to the sensor surface for

20 minutes at room temperature. The device was thoroughly rinsed with DI water. Figure 3.2c shows a top view SEM image of the M13KO7 bacteriophage immobilized on the PSi surface. Coulombic interactions prevent a uniform self-assembled monolayer due to the negatively charged nature of the virus.

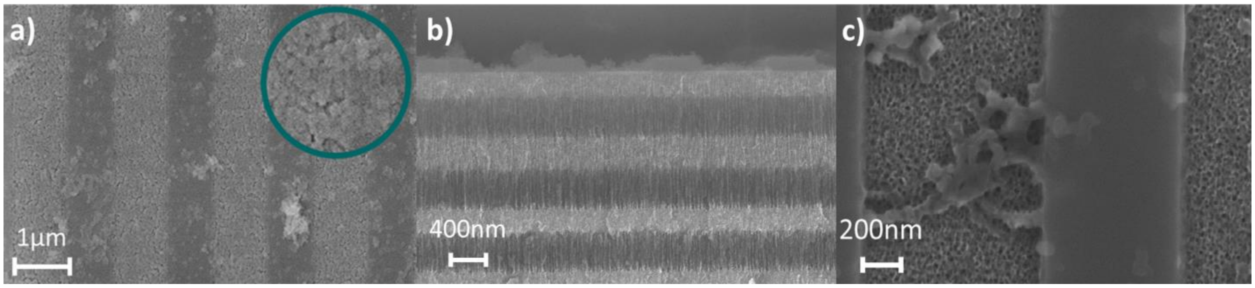

Figure 3.2. Top view SEM images of (a) 60nm latex nanosphere and (c) M13KO7 bacteriophage attachment to the PSi optimized-BSW/BSSW surface [108]. (b) Cross sectional view showing no latex nanospheres infiltrated the porous film.

3.3 Results and Discussion

3.3.1 Mechanism of PSi Bloch Surface and Sub-Surface Waves Device

Figure 3.3a shows the basic design of a PSi-BSW/BSSW structure. The key distinction between this structure and a traditional BSW structure is the introduction of an appropriately designed gradient or defect in the optical thickness of the layers of the 1-D photonic crystal, which creates a localized region of strong optical confinement just below the terminated 1D photonic crystal surface. Such a sub-surface wave mode (i.e., BSSW) had not been previously demonstrated in any material system. As explained in detail below, the BSSW is distinguished from waveguide and band edge modes and promotes both improved sensitivity and faster sensing response. The combination of BSW and BSSW modes in a PSi device thus provides a unique platform wherein larger molecules, filtered out by the pores, are readily detected with the BSW and smaller molecules passing into the pores are detected with the BSSW. The BSW mode is confined by the band gap created by the Bragg mirror and by total internal reflection near the surface. Similarly, by reducing the optical thickness of one or more layers within the multilayer through the introduction of a step or gradient refractive index profile, BSSW modes with different effective indices can be supported within the multilayer. The implementation of a single step to break the periodicity of the Bragg mirror refractive index profile shifts the band edge of the Bragg mirror and gives rise to a single BSSW mode confined within the corresponding layer with reduced optical thickness. By creating a gradient refractive index profile, a varying band edge within the multilayer allows a distinct mode within each H layer until prohibited by coupling losses or a band gap is no longer sustained [84]. Although a large sensitivity is important in biosensor design, a sharp and distinct resonance will enhance the minimum detectable shift for an improved detection limit. Therefore, in the design of the step and gradient profile structures, a tradeoff between sensitivity of the resonance position to small changes in refractive index and the resonance intensity was considered. A very small step or gradient refractive index change leads to a very large BSSW sensitivity. However, similar to a WG, the resonance intensity and mode confinement is reduced with a small refractive index contrast between H and L layers due to the reduced mirror strength of the multilayer. For very large refractive index changes within the multilayer, field confinement is increased, resulting in a sharp and distinct resonance. However, BSSW sensitivity decreases as a result of decreased surface area for molecular capture [44].

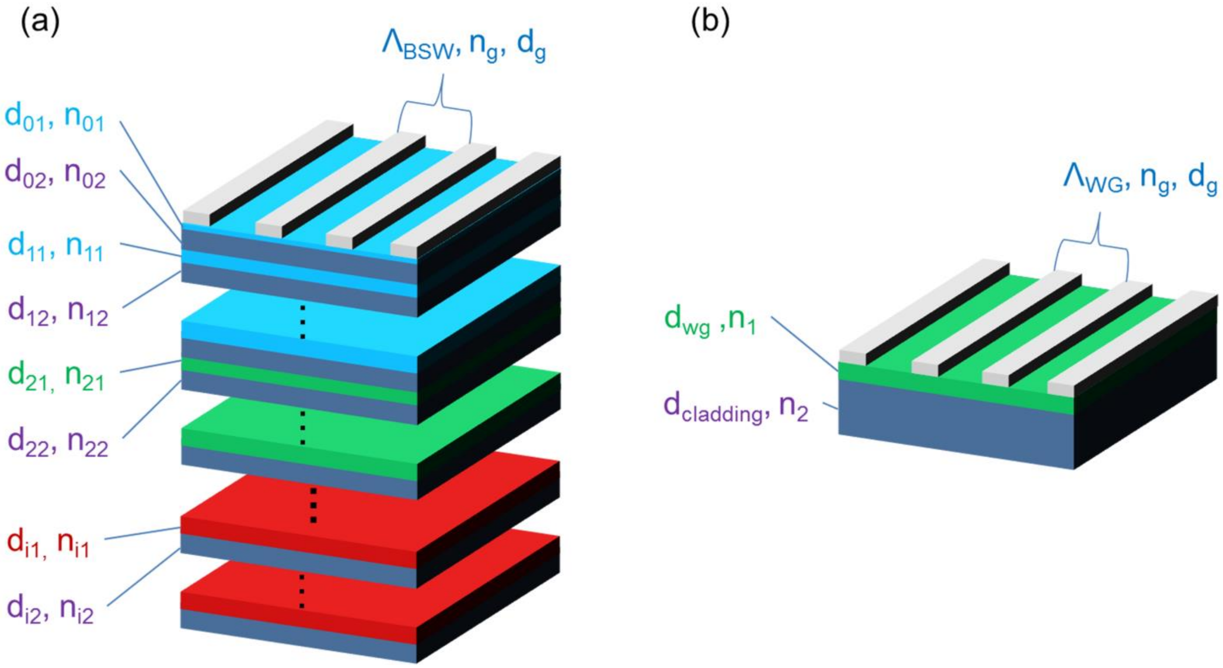

Figure 3.3. Refractive index profiles of the PSi grating-coupled a) BSW/BSSW and b) WG sensors with corresponding thickness, d, and refractive index, n. Λ is the grating pitch [110].

Dispersion relations and field profiles were calculated by transfer matrix theory to highlight the difference between BSSW and band edge (BE) modes. Figure 3.4 illustrates the dispersion relation and field profiles for two prototypical 1D PSi-BSW/BSSW structures (without grating couplers), designed for operation at 1550nm (~0.8eV) and excited through the Otto configuration using a high index n = 2.5 prism with a constant 500 nm air gap. In Figure 3.4a and c the BSW (red) is formed at the multilayer-air interface, where the 1D photonic crystal multilayer is nominally defined with layer thicknesses $d_{i1} = 340$nm, $d_{i2} = 580$nm and refractive indices $n_{i1} = 1.79$, $n_{i2} = 1.24$, respectively. Here, *i* is an integer (0-N) indicating the period iteration. The i = 0 period features a reduced optical thickness with $d_{01} = 175$nm, $n_{01} = 1.62$, which brings the BSW mode further into the band gap and away from the BE. The BSSW (blue) is introduced by reducing the optical thickness of layer, d_{11} (*i.e.*, the first high index layer below the surface), in this case by reducing the refractive index to $n_{11} = 1.62$. We refer to this particular structure as the *step index* BSSW. The step index geometry breaks the translational symmetry of the 1D photonic crystal forming a sub-surface defect state (BSSW) similar to how the multilayer-air interface of the terminated 1D photonic crystal forms a surface defect state (BSW). As shown in Figure 3.4a, the BSSW mode falls inside the BE and has a higher effective index than the BSW. The BSSW is characterized by strong field localization just below the multilayer-air interface. In the step index BSSW, the peak field is centered in layer d_{11} and rapidly decays both toward the surface and into the multilayer. This field profile is clearly distinguished from BE modes (black) wherein the field is distributed broadly across many layers deep within the multilayer (Figure 3.4c). In previous PSi-BSW studies, the sensitivity of the BE modes to small bulk refractive index changes has been shown to be less than the BSW resonance [61].

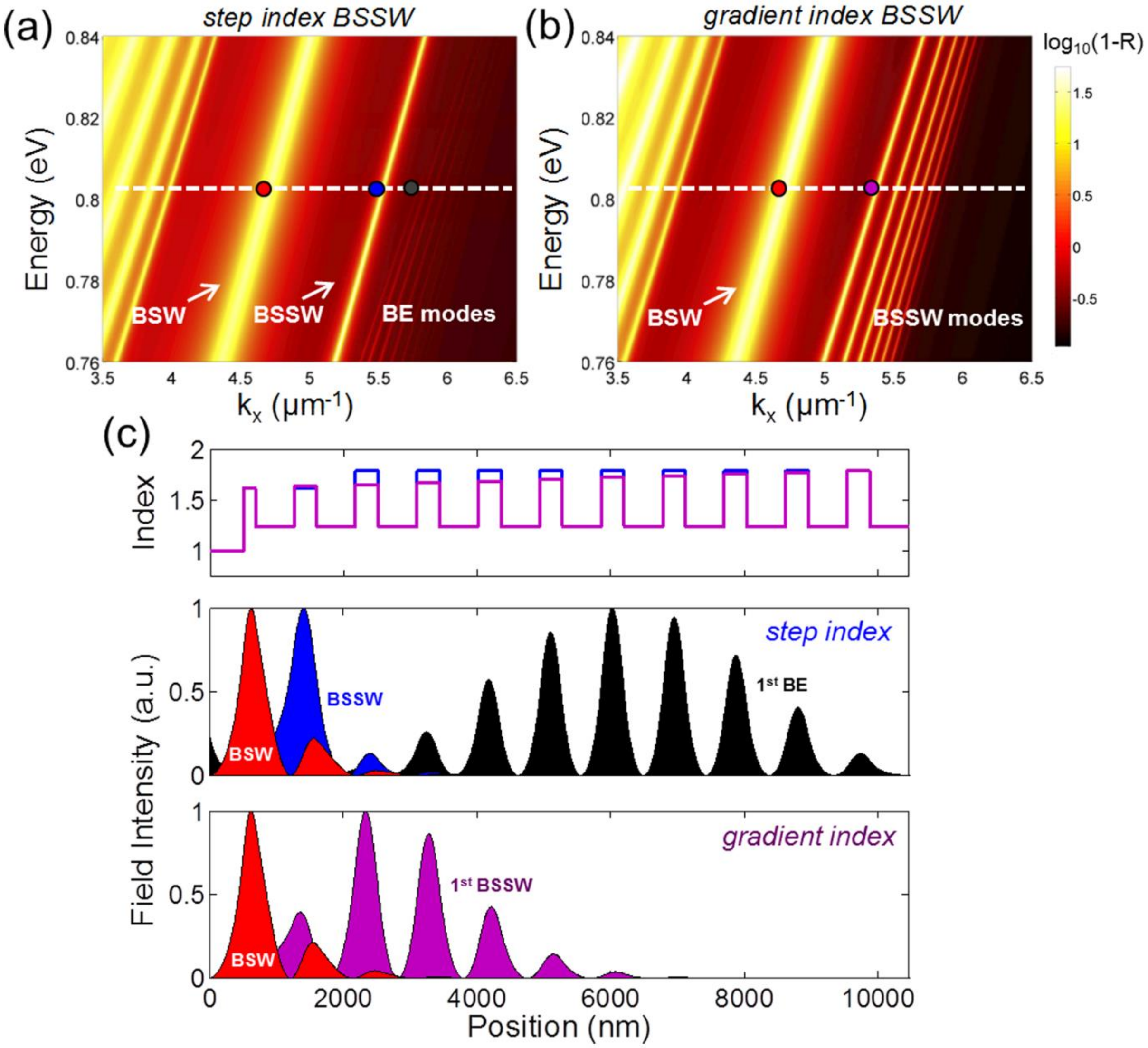

Figure 3.4. Dispersion relation of the BSW/BSSW sensor for the (a) step and (b) gradient refractive index distributions. (c) Refractive index profile for step (blue) and gradient (purple) index BSW/BSSW along with electric field confinements of the step (red/blue) and gradient (red/purple) index BSW/BSSW compared to the traditional band edge modes (black) [110].

A BSSW mode can also be introduced by gradually changing the optical thickness of the multilayer, forming what we refer to as the *gradient index* BSSW. In the gradient index structure, the index of layers d_{i1} and d_{i2} are gradually increased from 1.62 to 1.79 and 1.22 to 1.26, respectively. This effectively produces a locally varying band edge position and introduces numerous BSSW modes within the band gap (Figure 3.4b). The 1st order BSSW mode (purple) is characterized by a field distribution confined to the first few periods below the multilayer-air interface, and is akin to a BE mode that is biased toward the sensor surface. In principle, the gradient index BSSW can function in the same manner as the step index BSSW by providing a method for sensing analyte species that infiltrate the porous matrix just beneath the sensor surface. Owing to the gradual confinement provided by the gradient index structure, we anticipate that BSSWs excited in this configuration could provide sharp, high quality factor resonances, thereby promoting improved analyte detection. This is analogous to the reduction of radiation losses caused by tapering the Bragg mirrors of a microcavity, which results in an improved quality factor [111]. Moreover, unlike the BSW mode or modes of a PSi-WG, the BSSW is localized completely within the porous matrix, with almost no evanescent field leaking into the air cladding. This promotes increased sensitivity toward small molecules, as the BSSW can take full advantage of the increased surface area provided by the pores.

3.3.2 Modeling and Theoretical Sensing Performance

To demonstrate the principle functionalities of the grating-coupled PSi-BSW/BSSW sensor, rigorous coupled wave analysis (RCWA) simulations were employed [95]. The theoretical performance capabilities of the PSi-WG have been discussed elsewhere [25,68]. In Figure 3.5, we present four example analyte sensing scenarios to demonstrate the size selective advantage for the detection of small and large molecules using the BSW/BSSW structure. The location of the BSW and BSSW peaks in air (black curve) are 21.2° and 27.5°, respectively. Here, we utilize a gradient index BSSW structure, matching the simulated fitting parameters for our experimentally fabricated grating-coupled PSi-BSW/BSSW examined later. The four scenarios (a-d) illustrated in Figure

3.5, represent four different analyte attachment/infiltration geometries by modeling a change in refractive index in a specific highlighted area: (a) a refractive index change, $\Delta n = 0.5$, 0-10 nm above the surface of the structure, not including the grating, to simulate molecules that do not penetrate the pores, (b) a refractive index change, $\Delta n = 0.03$, in the entire structure to simulate small molecules uniformly distributed within the pores in addition to large molecules, with refractive index change $\Delta n = 0.5$, bound 0-10nm above the surface, (c) a refractive index change, $\Delta n = 0.03$, only in the BSW guiding layer and $\Delta n = 0.5$ 0-10nm above the surface for molecules that partially diffuse or clog the porous surface, and (d) a refractive index change, $\Delta n = 0.03$, only in the multilayer to simulate a theoretical scenario where small molecules only infiltrate the multilayer region. Many chemical and biological molecules can be modeled with reasonable accuracy using a refractive index of ~1.5 [25]. For typical biomolecule sizes and surface densities within the porous matrix, $\Delta n = 0.03$ is a typical effective index change, which may be expected following the monolayer attachment of small molecules according to the Bruggeman effective medium approximation [44]. Similarly, the displacement of air, $n = 1$, by densely packed large molecules with $n = 1.5$ at the surface will create an effective refractive index change of $\Delta n = 0.5$ when assuming a monolayer coverage.

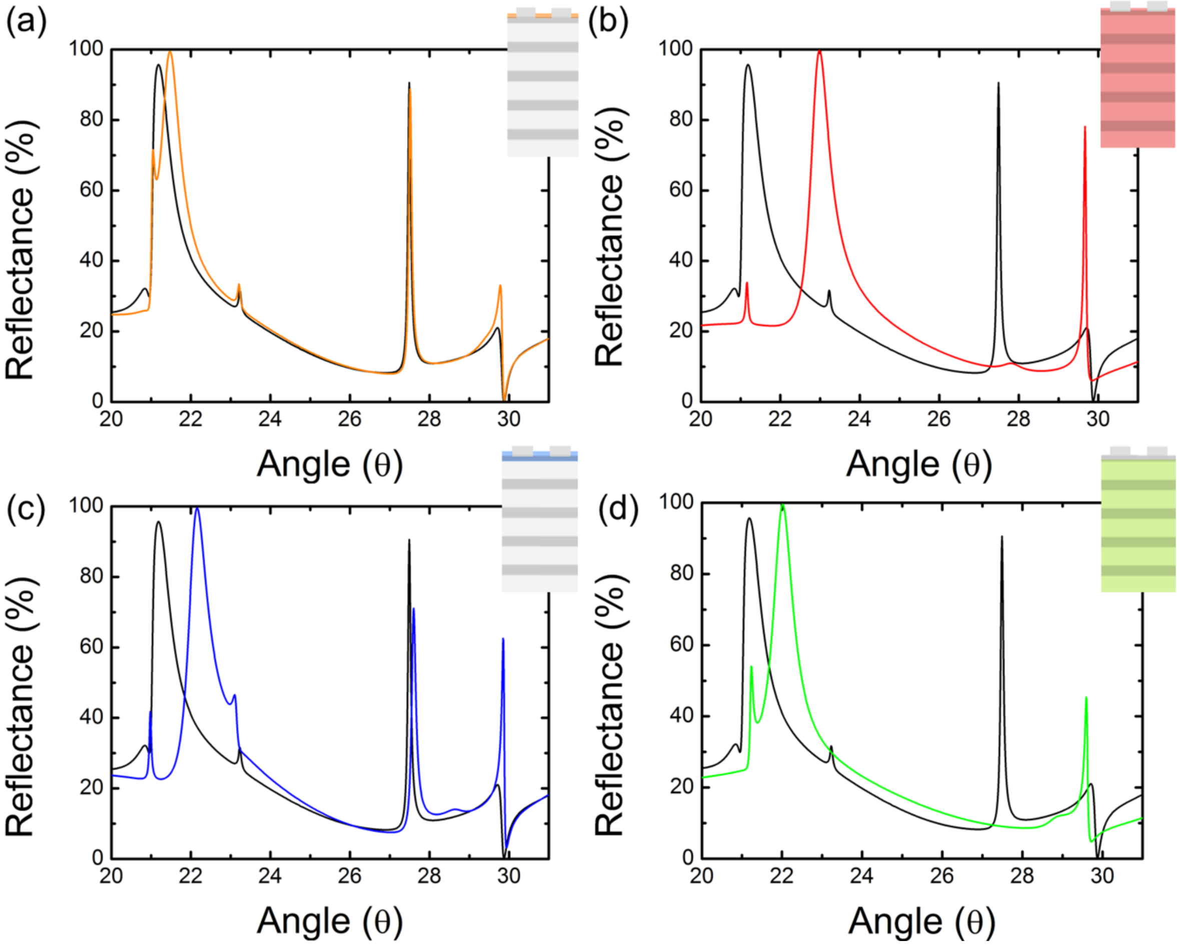

Figure 3.5. Simulated reflectance spectra shifts caused by the change in refractive index at a specified location in the BSW/BSSW sensor. a) Δn = 0.5 for 10nm above the surface. b) Δn = 0.03 for all layers and Δn = 0.5 for 10 nm above the surface. c) Δn = 0.03 for the top layer and Δn = 0.5 for 10 nm above the surface. d) Δn = 0.03 for only the multilayer [110].

In Figure 3.5a, modeling large molecules attached to the surface produces a 0.31° shift in the BSW resonance and a 0.02° shift in the BSSW resonance. As expected, the magnitude of the respective resonance shifts scales with the degree of spatial overlap between each mode and the simulated molecules , with the BSW mode interacting much more strongly with surface-bound molecules than the BSSW. In Figure 3.5c, a similar result is observed with slightly larger shifts observed for both the BSW and BSSW due to the simulated molecule infiltration into the guiding layer as well as attachment to the surface. Note that the pore size of the guiding layer can be optimized to allow for the infiltration of large molecules without affecting the coupling of the BSW by appropriately adjusting the thickness of the layer, as previously shown [64]. Figure 3.5b illustrates the presence of both large molecules 0-10nm above the surface and small molecules infiltrating throughout the multilayer. The presence of both molecules induces a large resonance shift for both the BSW and BSSW. As shown in Figure 3.5d, when only the refractive index of the multilayer is changed instead of the entire structure as in Figure 3.5b, the BSW resonance shift is reduced because a smaller fraction of the BSW mode is interacting with the simulated molecules. Note that the majority of the BSW mode that extends into the porous silicon structure exists in the guiding layer and only a small fraction extends further into the multilayer. Hence, the BSW resonance shifts observed in Figure 3.5c and Figure 3.5d are similar. Meanwhile, the BSSW resonance shift shown in Figure 3.5d is relatively unchanged compared to the case shown in Figure 3.5b because the BSSW mode has no significant field extending within the top guiding layer or surface as confirmed by the lack of a significant BSSW resonance shift in Figure 3.4c. Therefore, the BSSW is not sensitive to large molecules sitting on the surface of the sensor, but the BSW can be affected by both large and small molecules within the PSi layers due to the field overlap within the first two layers of the Bragg mirror. The BSSW sensitivity derived from Figure 3.5b is approximately 72°/RIU or 2038 nm/RIU and the large molecule sensitivities derived from the BSW shown in Figure 3a and c are approximately 0.6°/RIU (17 nm/RIU) and 31°/RIU (967 nm/RIU) for surface and top layer detection, respectively. In the next section, we demonstrate the application of our PSi-BSW/BSSW sensor.

3.3.3 Experimental Analysis of Initial BSW/BSSW Device

3.3.3.1 Device Characterization

Figure 3.6 shows SEM images of the fabricated PSi initial-BSW/BSSW and PSi WG structures used in this work. As discussed in section 3.2.1, our fabrication protocol produces a gradient index type PSi-BSW/BSSW structure. The gradient refractive index is confirmed by fitting the experimental angle-interrogated reflectance with RCWA simulation. As shown in Figure 3.7, the experimentally measured BSW and first order BSSW resonances are located at 21.2° and 27.5°, respectively. Additional BSSW modes can be seen at higher angles in both simulation and experiment. Importantly, the BSSW modes would not appear in this 28-35° angular range without the presence of a gradient or step index within the multilayer. Traditional BE modes were found in simulated structures at higher angles as demonstrated in Figure 3.4.

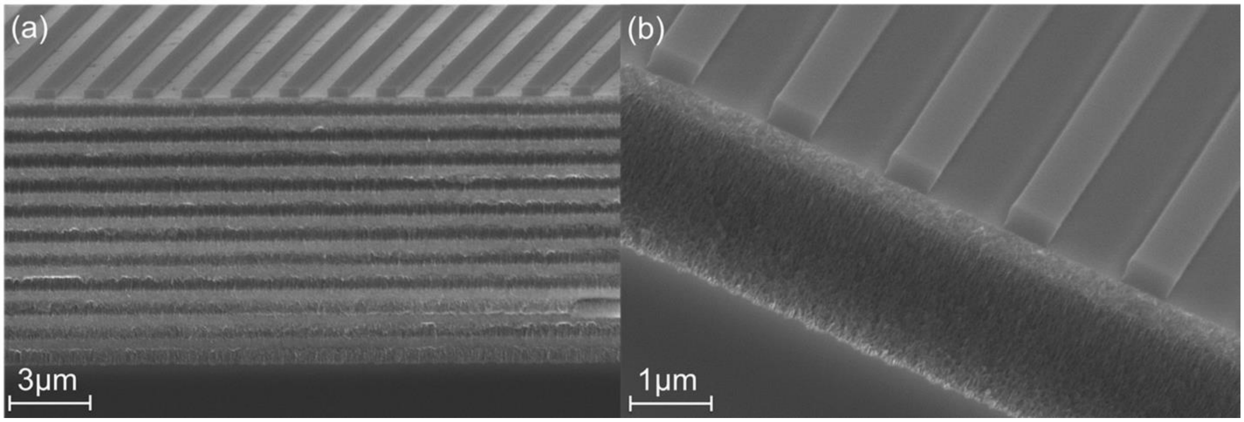

Figure 3.6. SEM cross-sectional images of the a) initial-BSW/BSSW and b) WG sensors [110].

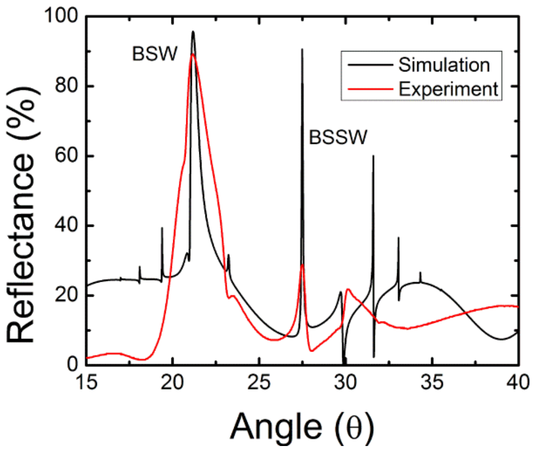

Figure 3.7. Comparison of simulated and experimental performance of the initial-BSW/BSSW sensor [110].

3.3.3.2 Sensing Performance

The sensing performance of the grating-coupled initial-BSW/BSSW and WG platforms in response to large (~10 nm) and small molecules (<2 nm) is shown in the attenuated total reflectance curves of Figure 3.8a-c. As model small molecules, 3-APTES (0.8nm) and Sulfo-SMCC (1.26nm) were attached in succession to the two sensor platforms [11,112]. Conveniently, these small molecules also serve as linker molecules for the immobilization of our chosen large molecule, a 13.2 nm long 40mer thiol modified probe DNA. This 40mer DNA has previously been used in studies on PSi-WGs and was shown to be unable to effectively infiltrate the ~20 nm pores of the high index PSi layers [43].

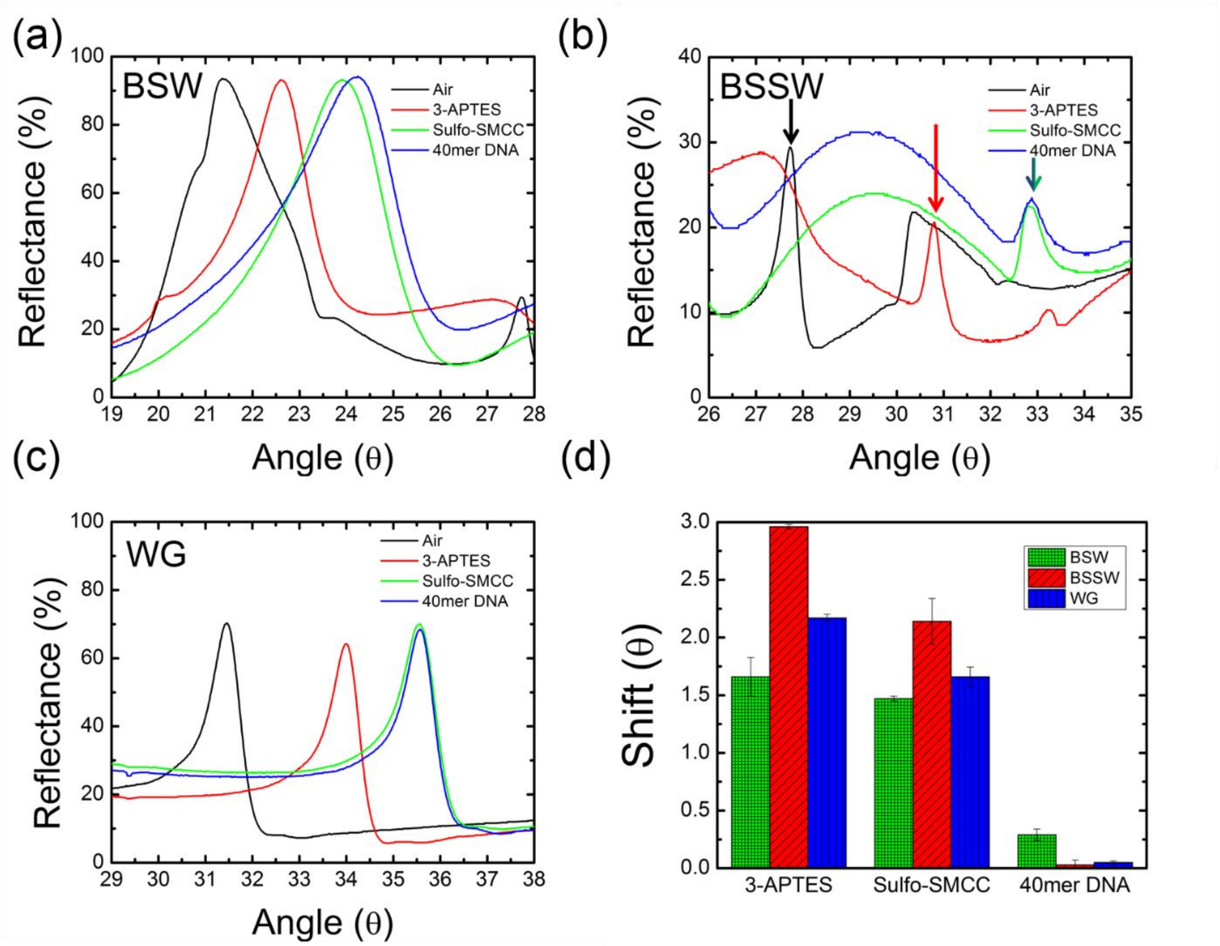

Figure 3.8. Angle-resolved reflectance spectra after small and large molecule attachment in PSi: a) BSW, b) BSSW, and c) WG structures. The arrows shown in (b) highlight the BSSW mode. d) Comparison of the BSW, BSSW, and WG detection sensitivity to different molecules, normalized by the initial resonance angle [110].

In this experiment, the 3-APTES and Sulfo-SMCC small molecules produce large resonance shifts (>1 degree) for all three resonant modes, indicating that they can readily penetrate the porous matrix. Experimentally measured resonance shifts for the small molecule attachment in the multilayer of the BSW/BSSW sensor correspond to a gradient effective refractive index change of approximately $\Delta n = 0.03 - 0.05$ for 3-APTES and $\Delta n = 0.01 - 0.03$ for Sulfo-SMCC. Sensor sensitivity to these small molecules can be ranked by increasing order: BSW, WG, and BSSW.

The BSSW shows the largest response to small molecule attachment with a 33% enhancement over the benchmark WG sensor (Figure 3.8d).

In response to 40mer DNA attachment, the BSSW and WG show very small angle normalized resonance shifts of ~0.03° and ~0.05°, respectively, indicating that the large molecules are only weakly detected by these optical modes. The BSW mode, meanwhile, shifts ~0.29°, demonstrating a ~6 fold enhancement when compared to the WG. The experimentally measured resonance shifts for DNA attachment suggest an effective refractive index change of approximately $\Delta n = 0.3$ in the region 10 nm above the surface of the BSW/BSSW sensor. If the porosity of the top layer is increased, improved molecule infiltration into the top layer may occur, leading to even higher large molecule detection sensitivity. The normalized resonant responses to large and small molecule attachment across the different sensors are summarized in Figure 3.8d and show that the BSW and BSSW modes exhibit the largest sensitivity to large or small molecules, respectively. The normalized resonant response are not dependent on the angle of the excited mode. As deduced from Equation 1.2, the angle dependency can be eliminated by multiplying the sensitivity by $\cos(\theta)$. As the BSW and BSSW are excited in the same structure, this importantly demonstrates size selective sensing. Specific and selective detection of target molecules using the BSW/BSSW sensor can be conducted in a similar manner as has been reported for other PSi biosensor structures. Potential applications for high accuracy specific binding events previously demonstrated in PSi biosensors include small or large DNA [25], proteins [57], and enzymes [61]. Moreover, the enhanced sensitivity gives PSi-BSW/BSSW sensors a powerful advantage when benchmarked against the PSi-WG, which itself has previously been shown to have a significant sensitivity advantage in comparison to other platforms such as planar SOI waveguide sensors [25].

3.3.4 Experimental Analysis of Optimized-BSW/BSSW Device

3.3.4.1 Device Characterization

Figure 3.9 shows both the simulated (RCWA) and experimental angle-resolved reflectance spectra of an optimized grating coupled step and gradient index BSW/BSSW sensor. In Figure 3.9a, the BSW resonance is located at ~21° and the single step BSSW mode is located at ~25°. In Figure 3.9b, the BSW mode is located at ~15° and the remaining peaks correspond to the different BSSW orders created by the gradient index profile. The different resonance angles are a result of the different refractive index step and gradient depth profiles used in the optimization. Good agreement is observed between the simulations and experiment. Minor deviations are likely a result of a nonlinear refractive index gradient or step caused by the KOH etch [84]. Both the step and gradient BSW/BSSW designs are suitable for size selective sensing applications. However, the step index sensor has a higher detection sensitivity due to the single well-confined BSSW resonance, as shown in the field profile in Figure 3.1b, while the gradient index sensor with multiple BSSW modes spatially distributed within several high index layers of the multilayer allows for the determination of the depth of infiltration of molecules within the multilayer.

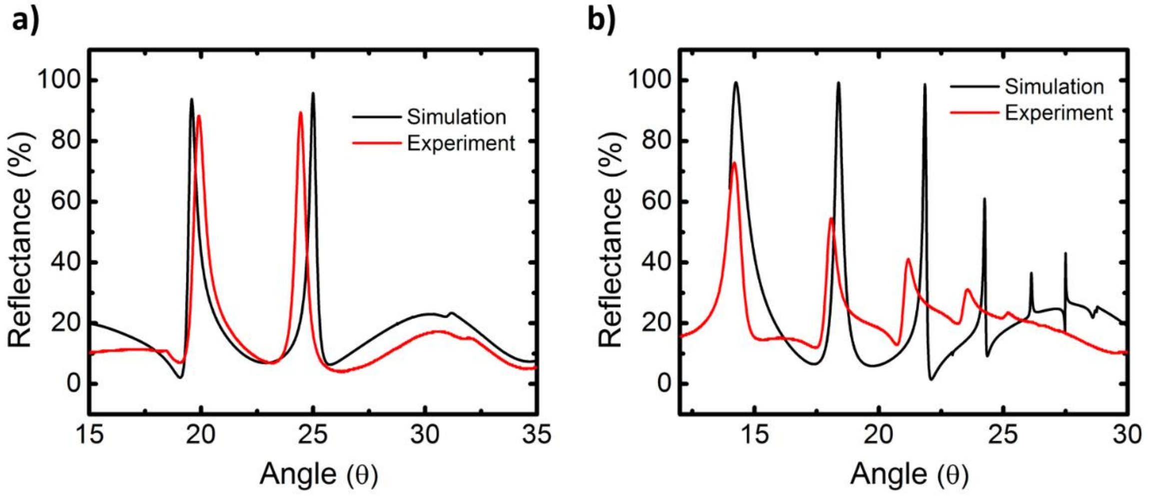

Figure 3.9. Simulated and experimental reflectance spectra of optimized (a) step and (b) gradient index PSi BSW/BSSW sensors in air [108].

3.3.4.2 Size Selective Detection of Large Latex Nanospheres

In order to demonstrate the sensing capabilities of the step and gradient index optimized-BSW/BSSW, small APTES molecules that bind primarily within the porous matrix and large nanospheres that may only bind onto the surface of the PSi are exposed to the sensors (Figure 3.10a). Results of the attachments of APTES and nanospheres to the step (grating-coupling configuration) and gradient (prism-coupling configuration) index sensors are depicted in Figure 3.10b and c, respectively. The step index profile gives rise to a single BSSW mode while the gradient index profile has three BSSW modes due to the varying band edge within the multilayer. The spectrum label "air" was measured after oxidation of the BSW/BSSW structure. The subsequent attachment of APTES and then nanospheres leads to a redshift in the spectrum corresponding to the addition of material to the sensor. When APTES is attached, both the BSW and BSSW(s) modes shift in resonance positions due to APTES infiltrating all regions where the fields are confined. When the nanospheres are attached to the APTES functionalized sensor, they cannot penetrate the layers where the BSSW field is primarily confined and therefore do not cause a significant shift to the BSSW resonance position. The evanescent field of the BSW is able to detect the presence of nanospheres in both the prism and grating coupled configurations. Table 3.2 contains the angular resonance shift data of the step and gradient index BSW and 1st order BSSW shown in Figure 3.10. The 2nd and 3rd order BSSWs of the gradient index BSW/BSSW sensor demonstrate a detection sensitivity that is similar to that of the 1st order BSSW. The larger sensitivity of the step index sensor compared to the gradient index sensor derives from the smaller refractive index step depth as shown in Figure 3.1a and b. Additionally, higher sensitivity in grating coupled structures has been observed in comparison to prism coupled structures [68]. The slight blue shift reported for the gradient index BSSW after exposure to the nanospheres may be attributed to loss of a small fraction of the immobilized APTES molecules that could occur during the rinsing stage as a result of APTES molecules' compromised stability in water [109].

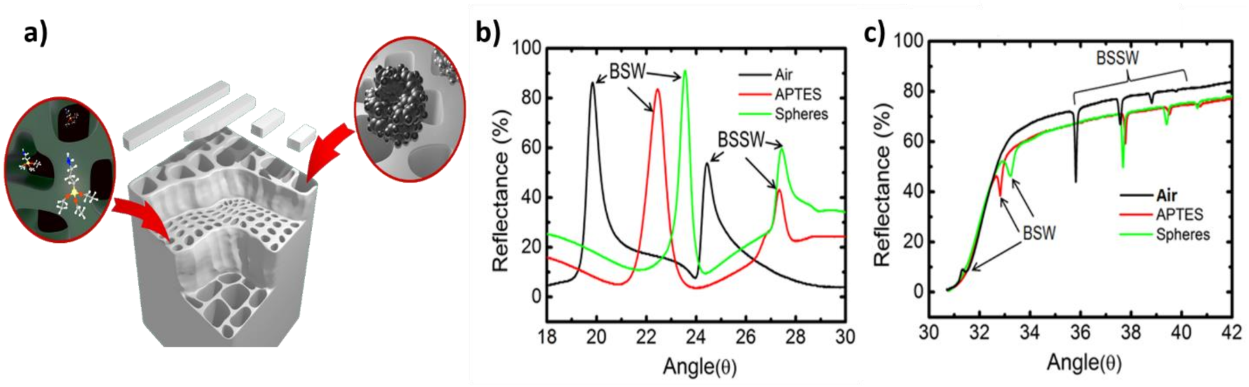

Figure 3.10. (a) Schematic illustration of size selective sensing experiment in which both small and large species are exposed to the PSi BSW/BSSW sensor. Reflectance spectra of (b) grating coupled step index and (c) prism coupled gradient index optimized-BSW/BSSW sensors after exposure to small (APTES) and large (Spheres) species [108].

Molecules	BSW (Step)	BSSW (Step)	BSW (Gradient)	BSSW (Gradient)
APTES	2.60°	2.88°	1.32°	1.96°
Spheres	1.11°	0.25°	0.42°	-0.08°

Table 3.2. Resonance shifts illustrated in Figure 3.10.

3.3.4.3 Bacteriophage Detection

In order to demonstrate the feasibility for detecting large biological organisms that have previously presented a challenge in PSi sensors, the M13KO7 bacteriophage was immobilized onto a grating-coupled gradient index optimized-BSW/BSSW sensor. APTES and GA are small chemical linker molecules that infiltrate the pores and are therefore detected by both the BSW and BSSW modes as shown in Figure 3.11a. Resonance shifts for APTES and GA for the BSW and 1st BSSW mode are (1.6°; 2.18°) and (1.97°; 2.66°), respectively. The large M13KO7 bacteriophage does not infiltrate the 20 nm pores and is solely detected by the BSW with a resonance shift of 0.31° (Figure 3.11b). The BSSW shows a small shift of 0.01° that can be attributed to the small evanescent field of the BSSW at the surface (Figure 3.1c). In future applications, the M13KO7 virus can be selectively bound to the surface using an antibody probe method similar to that reported in Ref. [105]. The response of the BSW to the model virus leads to the conclusion that the BSW mode is able monitor changes in refractive index to detect large organisms such as cells, bacteria, and viruses that are selectively bound to the surface using appropriate chemical functionalization. The BSW/BSSW is a versatile sensor with possible integrations with lab-on-a-chip technology to detect small molecules with an extremely high sensitivity (>2000nm/RIU) and will not be limited in detecting large species that cannot infiltrate the pores.

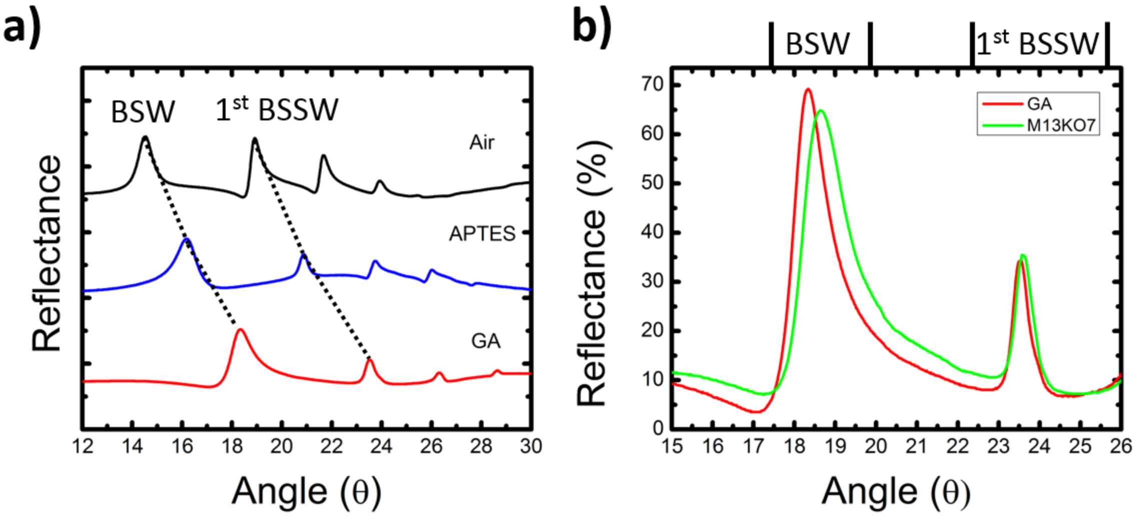

Figure 3.11. (a) Angular reflectance spectra of a gradient index optimized-BSW/BSSW sensor with the attachment of APTES and GA. (b) Resonance shifts after the attachment of M13KO7 bacteriophage to the GA functionalized gradient index optimized-BSW/BSSW sensor shown in (a) [108].

3.4 Summary

This chapter demonstrates, through simulation and experiment, a grating-coupled PSi BSW sensor that supports BSSW modes. The BSW and BSSW modes enable high sensitivity and size-selective sensing of both large surface-bound molecules and small molecules that infiltrate the pores. The BSW mode demonstrated a 6-fold improvement in detecting large molecules when compared to BSSW and WG modes. The novel BSSW mode demonstrated ~33% enhancement in small molecule sensitivity when compared to a WG mode, owing to the improved field overlap and full use of the porous matrix in both core and evanescent field regions.

The optimized fabrication and realization of step and gradient index BSW/BSSW sensors was additionally demonstrated. The excitation of both BSW and BSSW modes within the same structure in both grating and prism coupled configurations allowed for simultaneous detection of APTES and GA with both modes and the detection of large 60 nm nanospheres and the large M13KO7 bacteriophage with the BSW. The strong confinement of the BSSW minimizes the overlap with surface immobilized analytes for high sensitivity, high selectivity applications. The evanescent field of the BSW allows for detection of very large molecules that could not be detected in typical PSi devices such as interferometers, microcavities and waveguides. Size-selective detection using the same sensor platform is expected to be a significant advantage for future multi-analyte detection schemes using a microfluidics approach. In the next chapter, we explore the use of PSi WG and BSW films to laterally confine light using ring resonator and photonic crystal cavities.

CHAPTER 4

POROUS SILICON WAVEGUIDE RING RESONATORS

4.1. Introduction

Optical biosensors based on microring resonators are among the most promising biosensor platforms due to their long temporal light-matter interaction with surface bound molecules leading to competitive refractometric detection sensitivities, their ability to be cascaded together to make arrays, and their compact size for integration into portable lab-on-a-chip platforms. In particular, SOI rings have been well-characterized and demonstrated for the detection and kinetics analysis of various chemical and biological molecules relevant to the military, the environment, food safety, and medical applications [19,73]. The primary limiting factor for the detection sensitivity of traditional ring resonator sensors (typically near 160 nm/RIU or 0.158 nm/nm) [73,85] is related to their fabrication on planar (i.e., non-porous) SOI and polymer materials. For planar materials, the majority of the electric field distribution associated with a WG mode is inside the WG, which is inaccessible to chemical and biological molecules. Spatial overlap of target molecules and the optical mode occurs only at the WG surface where the evanescent tail of the mode exists [113]. Approaches to overcome this challenge have been pursued, including incorporating a slot in the WG ring or exciting the transverse magnetic (TM) mode to create a discontinuous electric field at the interface between the guiding layer and surface, generating a stronger molecular interaction with the evanescent tail of the mode. These design approaches have led to improved detection sensitivities near 246 nm/RIU and 0.290 nm/nm, respectively, for ring resonator sensors [14,19,85]. In this work, an alternate strategy of using a porous material, PSi, for the ring resonator waveguide is pursued to allow molecular infiltration into the guiding layer for direct interaction of target molecules with the resonant optical mode.

The only prior report of using a porous material for ring resonator structures is for a porous polymer ring resonator. However, the TM measurements performed and the very low porosity achievable for the polymer resulted in only a 94 nm/RIU bulk sensitivity [114]. In this chapter, we demonstrate the first PSi ring resonator structure and its application for chemical and biomolecular sensing. In comparison to traditional SOI ring resonators, the PSi ring resonator exhibits more than a factor of two increase in bulk detection sensitivity and an order of magnitude improvement in surface sensitivity for specific molecular detection. Section 4.2 presents the design, fabrication, measurement setup, surface functionalization method, and analyte preparation procedures. In section 4.3, we report on the characterization of the PSi ring resonator through computations and experiments, demonstrate its capabilities as a highly sensitive biosensor, and investigate the nonlinear properties of PSi that result from changes in input laser power and ambient temperature.

4.2. Materials and Methods

4.2.1 Design

Figure 4.1 shows a schematic of the ring resonator and identifies the various design parameters. Rings with radius size r = 10 μm and 25 μm are patterned with coupling gaps, g = 200 nm. The 200 nm gap size was experimentally tuned to achieve critical coupling. The effective index method was used to design a WG with a single TE mode. The ring WG width, w_{wg}, is 1.2 μm with height, h_{wg} = 600 nm and $h_{cladding}$ = 1.4 μm on a silicon substrate as shown in the inset of Figure 1. The design consists of a double layer PSi WG on a silicon substrate with refractive indices n_{wg} = 1.79, $n_{cladding}$ = 1.24, and n_{sub} = 3.5, respectively. In addition, the ridge WG is tapered linearly from w_{taper} = 20 μm to w_{wg} = 1.2 μm over a length l_{taper} = 500 μm to reduce coupling losses. The 1.2 μm WG width is extended for l_{wg} = 1.2 mm with the ring of corresponding radius located at the center.

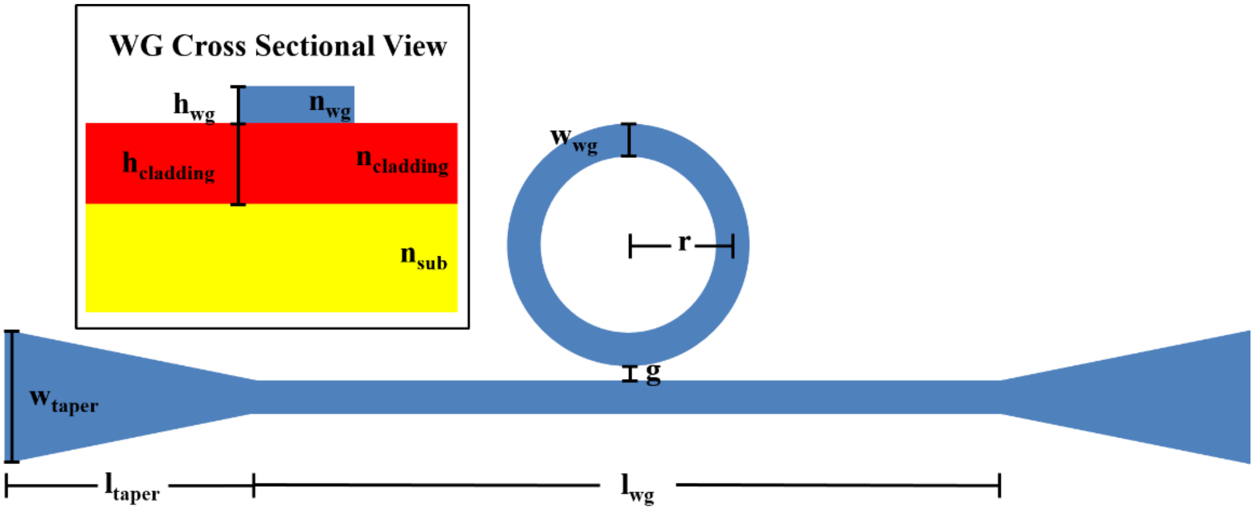

Figure. 4.1. Labeled schematic of PSi ring resonator employed in this work [67].

4.2.2 PSi Ring Resonator Fabrication

PSi slab WGs were fabricated by electrochemical etching of p+ (0.01 Ω·cm) Si (100) wafers in a 15% solution of hydrofluoric acid (HF) in ethanol. The guiding layer was created by applying a 5 mA/cm^2 current density for 114 seconds. The cladding layer was then etched at 48 mA/cm^2 for 53 seconds. A 1.5 mM·L^{-1} potassium hydroxide solution in ethanol was placed on each PSi WG for five minutes to widen the pores to improve molecular infiltration. Finally, the samples were oxidized at 500°C in air for five minutes to activate the surface for subsequent chemical functionalization. The resulting WGs had a 600 nm thick guiding layer with refractive index of 1.79 and a 1450 nm thick cladding layer with refractive index of 1.24. The thicknesses were determined from SEM images and the refractive index parameters were determined by fitting reflectance spectra with transfer matrix simulations.

Rings were patterned on the slab waveguides using standard electron beam lithography (EBL) and reactive ion etching (RIE). EBL resist, ZEP 520A, was spun at 5000 rpm onto each PSi sample to create a 300 nm resist film. The rings of various sizes were then patterned by a JEOL

JBX-9300-100kV EBL tool, followed by a 30 second development in xylenes and rinsing in isopropanol. The patterned rings were then etched with an Oxford Plasmalab 100 RIE tool using $C_4F_8/SF_6/Ar$ gases for approximately 8 minutes and 30 seconds to transfer the ring pattern into the guiding layer of the PSi WG. It was found that the short thermal oxidation step facilitated etching smooth sidewalls of the PSi ring resonator. Samples were etched to the WG and cladding interface as verified by top view and cross sectional SEM images. Finally, a 10 minute O_2 plasma clean was performed to remove residual ZEP 520A resist. A scanning electron microscope (SEM) image of the entire ring is shown in Figure 4.2a. The top view SEM image in Figure 4.2b illustrates the different porosities of the guiding and cladding layers and the cross-sectional SEM image in Figure 4.2c shows the smooth PSi WG sidewall with photoresist on top of the high index layer. The rough interface between the high and low index layers in Figure 4.2c is a result of the sample being manually cleaved.

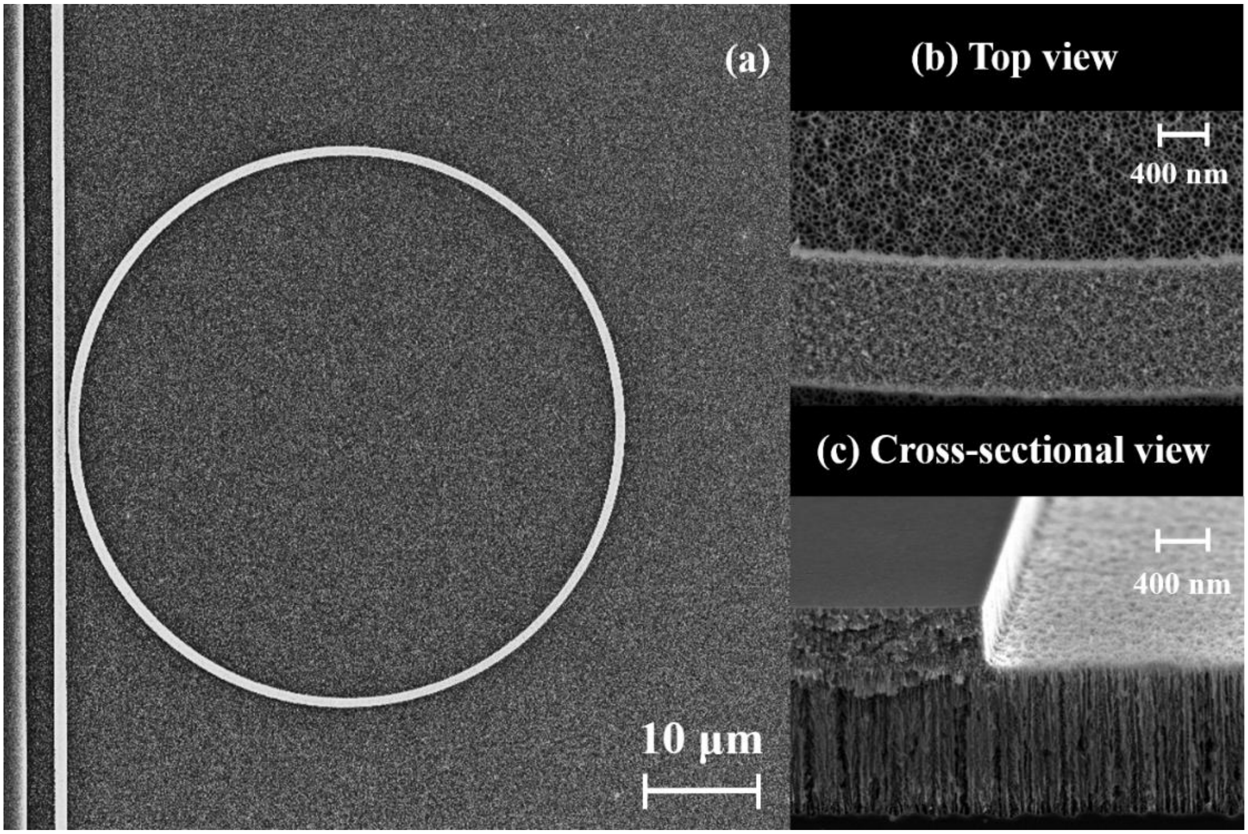

Figure 4.2. SEM images of (a) 25µm radius PSi ring resonator WG, (b) top view porosity profile of the WG (small pores) and cladding (large pores) layers, and (c) cross section of the ridge WG post RIE etch [67].

4.2.3 Measurement Setup

The PSi ring resonator chips were cleaved to an approximate 2.5 mm WG length and placed on a piezo-controlled XYZ stage. A tunable continuous wave laser (Santec TSL-510) was coupled into the tapered ridge WG using lensed fiber (OZ Optics Ltd.). The TE polarized laser was swept from 1500-1630 nm with step size of 0.05 nm. The transmission was detected using a fiber-coupled photodiode receiver (Newport 2936-C). The tapered input and output fibers were positioned manually on each WG with the assistance of an infrared camera. All samples were measured at room temperature and a constant input power to minimize resonance wavelength fluctuations caused by thermo-optic effects. Additional reflectance measurements on unpatterned PSi slab

WGs were performed on a Varian Cary 5000 UV-VIS-NIR spectrophotometer. The unpatterned PSi slab WG was exposed to the same processing conditions as the PSi ring resonator described in section 4.2.2, with the exception of the EBL exposure step such that no pattern was transferred to the slab waveguide.

4.2.4 Surface Functionalization

The bulk sensitivity of the PSi ring resonators was determined by exposure to several salt water concentrations. Refractive indices of the salt water solutions were found using a birefringence refractometer (Leice Abbe II). A 7.5 μL aliquot of each salt water solution was drop cast on the PSi ring resonators to ensure complete coverage of the rings during measurements. The PSi rings remained wet throughout the transmission measurements. In order to verify that the salt water concentration stayed constant during the measurements, control experiments were performed in which the time-dependent shift of the resonance wavelength was measured after a salt water solution was drop-cast onto the PSi ring resonator. Less than a 0.01 nm shift was observed during the first minute, corresponding to the measurement window for the bulk sensitivity measurements, confirming that evaporation effects are negligible. Following each salt water solution measurement, the PSi rings were rinsed with deionized (DI) water to remove residual salt from within the porous matrix, and then dried with nitrogen gas.

The surface sensitivity of the PSi rings was determined through specific detection of 16mer target peptide nucleic acid (PNA). Similar to Ref. [22], a 4% solution of 3-aminopropyltriethoxisilane (3-APTES) in methanol and water was placed on the rings for 15 minutes, and then the rings were rinsed with methanol, thermally annealed for 10 minutes at 100°C, and soaked in methanol for an additional 10 minutes. Next, a 4.0 mg/mL solution of succinimidyl 3-(2-pyridyldithio)propionate (SPDP) in ethanol is placed on the 3-APTES functionalized rings for 30 minutes, followed by a 30 minute soak in ethanol. SPDP is used as a linking molecule to immobilize 100 μM thiol-modified 16mer probe DNA (5'TAG CTA TGG TCC TCG T-3') in 4-(2-hydroxyethyl)-1-piperazineethanesulfonic acid (HEPES) buffer. The DNA is reduced by immobilized tris(2-carboxyethyl)phosphine (TCEP) disulfide reducing gel (Pierce). The DNA solution is placed on the functionalized rings for 1 hour, followed by a 30 minute rinse in HEPES buffer. The prepared PSi ring resonator sensor is then submerged in a 500 nM solution of complementary PNA (ACG AGG ACC ATA GCT A) in DI water for one hour. Finally, the sample is soaked in DI water for 30 minutes to remove non-hybridized PNA strands and dried with nitrogen gas.

4.3. Results and Discussion

4.3.1 Propagation and Bending Losses

The propagation losses were determined by measuring the maximum transmission of PSi ridge WGs of different lengths without coupling tapers or ring patterning. The fabrication procedure is identical to that specified for the PSi rings in Section 4.2.2 and the measurement procedure is identical to that specified in Section 4.2.3. The inset of Figure 4.3 shows the propagation losses for two sets of identical PSi ridge WGs of lengths 2.53 mm, 3.38 mm, 4.33 mm, and 5.63 mm with the transmission referenced to the shortest WG. The variation in measured transmission for WGs of the same length is likely a result of the manual alignment of the fibers used for butt coupling with the 1.2 μm wide WG. The propagation loss for the 1.2 μm wide WG is estimated to be near 2.75 dB/mm at 1550 nm, as determined from the slope of the linear fit ($R^2 = 0.87$) shown in the inset of Figure 4.3. This value agrees with previously reported propagation losses for PSi films with similar oxidation conditions [27]. Although it is possible to reduce the propagation losses to < 1.5 dB/mm by increasing the oxidation time, the Q-factor of the ring resonator would decrease due to the resulting reduced refractive index contrast between the two oxidized porous layers of the WG.

In order to estimate bending losses in the PSi ring resonators, PSi ridge WGs with two 90° bends were fabricated as shown in the SEM image in Figure 4.3. The bending losses for 10 μm and 25 μm radius bends were determined to be <1 dB/90° bend, as the propagation losses dominated in both cases, which is comparable to reports for SOI WGs [115].

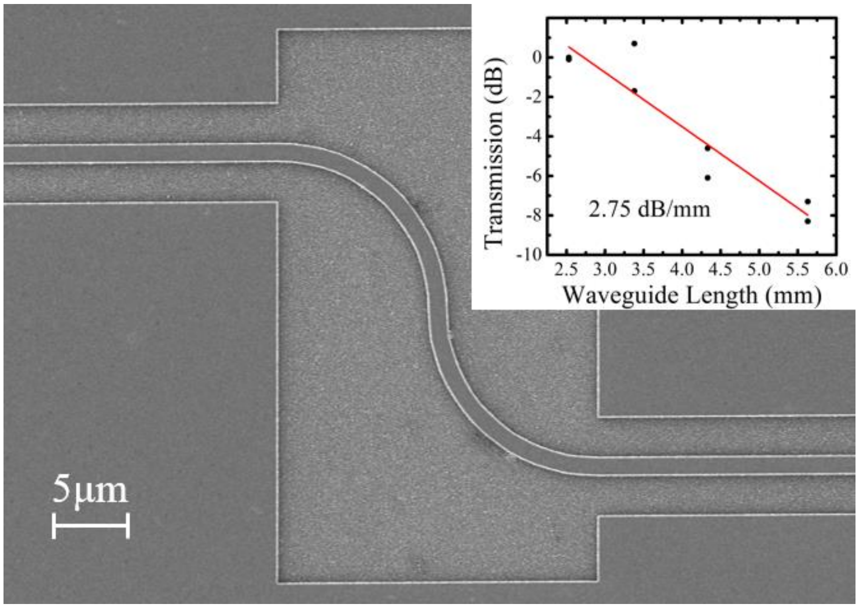

Figure 4.3. SEM image of two 10 μm radius 90° bends in a PSi ridge WG used to characterize bending losses. Bending losses are estimated at <1 dB/90° bend. The inset image shows the relationship between measured transmission and PSi WG length, yielding PSi propagation losses of 2.75 dB/mm [67].

4.3.2 Spectral Characterization

Figure 4.4a presents the simulated and experimentally measured transmission spectra of a 25 μm radius PSi ring resonator. The simulated spectrum was obtained using 3-dimensional finite-difference time-domain (FDTD) analysis with the WG parameters given in section 4.2.1. The experimentally measured spectrum is in good agreement with simulation and shows a 7.6 nm free spectral range (FSR). The small, 40 pm deviation in resonance position is attributed to a slight difference in the simulated and actual PSi refractive index profile. A 2 nm deviation in resonance position was observed amongst all measured samples, which is attributed to slight variations in fabrication conditions. The Q-factor of the 25 μm radius PSi ring is estimated to be 9100 based on a Lorentzian fit of the measured resonance shown in Figure 4.4b. The Q-factor for the 10 μm radius PSi ring is 6400 near 1557 nm with a FSR of 18.8 nm, as shown in Figure 4.4c. In an aqueous environment, the Q-factors of the 10 μm and 25 μm PSi rings were estimated to be 3400 and 4000, respectively. The lower Q-factors in water are a result of water infiltrating the pores, which reduces the refractive index contrast between the two layers of the PSi WG.

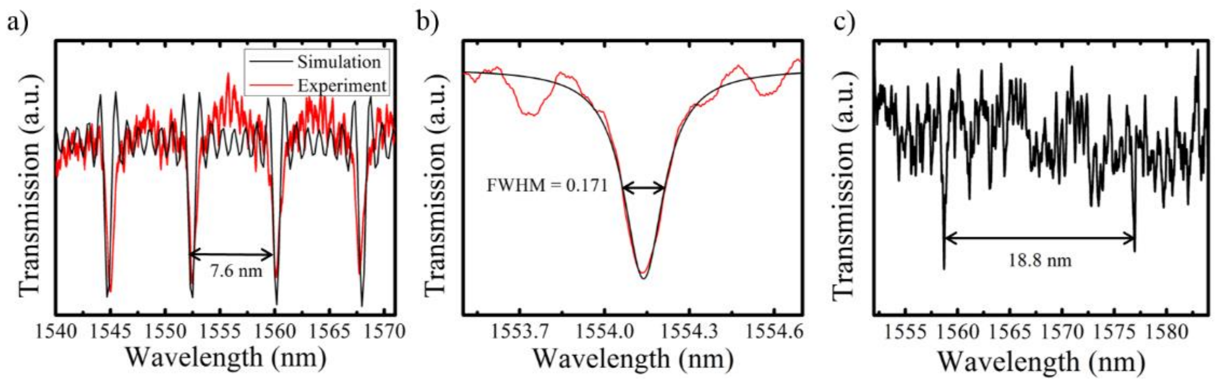

Figure 4.4. (a) FDTD simulation (black) compared to measured transmission spectrum (red) of a 25 μm PSi ring. Good agreement of FSR = 7.6 nm and resonance wavelengths is observed. (b) Lorenzian fit of resonance near 1554 nm, which indicates a Q-factor of 9100. (c) Transmission spectrum of a 10 μm PSi ring with FSR = 18.8 nm and Q-factor of 6400 near 1558 nm [67].

4.3.3 Bulk Sensitivity Measurements

Exposure to different salt water solutions is a common approach for determining the bulk sensitivity of a biosensor due to the well characterized refractive index of varying NaCl concentrations in water and the low cost of the mixtures [60,73]. Accordingly, different salt water solutions are placed on PSi rings of 10 μm and 25 μm radius to determine their bulk sensitivity. The diffusion of the NaCl solution into the pores is nearly instantaneous due to the small size of NaCl [60,116]. Transmission measurements are conducted immediately after the 7.5 μL aliquot is placed on each ring. Between each salt water measurement, the PSi ring is rinsed with DI water and the transmission spectrum is measured to verify that the resonances return to their initial wavelengths, confirming that no salt remains in the rings. The shift of each resonance upon exposure to a given salt water concentration is measured relative to the DI water reference resonance wavelength of the PSi ring. The bulk sensitivity of the PSi ring is then estimated by a linear fit to the data with R^2 values greater than 0.99. As shown in Figure 4.5, the bulk sensitivity of the 10 μm radius PSi ring is 384 ± 3.7 nm/RIU and that of the 25 μm PSi ring is 380 ± 4.5 nm/RIU. The bulk sensitivity values are the largest reported for ring resonator sensors and are achieved because the porous nature of the ring allows the salt water to penetrate into the volume inside the ring where the majority of the optical mode is confined. The modal profile of a PSi WG and its sensitivity comparison to SOI WGs has been previously reported [25]. We believe this increased light-matter interaction in the pores is the dominant factor in the bulk sensitivity increase and that longer temporal interactions arising from the ring resonator geometry play only a minor role. Due to the large sensitivity of the PSi rings, the FSR becomes a limiting factor for the detection of very large index changes. Accordingly, the maximum detection limits of the 10 μm and 25 μm PSi rings are $\Delta n = 0.05$ and 0.02, respectively, for single point measurements such as those conducted in this work. Larger refractive index changes would result in a resonance shifting by more than one FSR, confounding quantitative analysis. This maximum limit of detection may be circumvented if a real-time measurement system using microfluidics to enable continuous monitoring is incorporated.

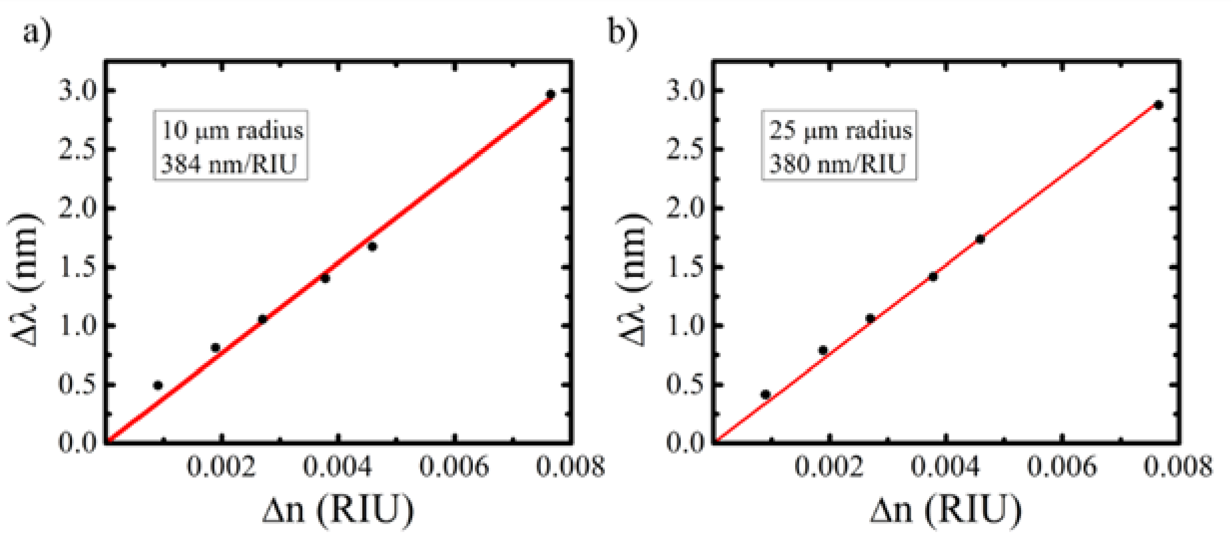

Figure 4.5. Bulk sensitivity of (a) 10 µm and (b) 25 µm radius PSi ring resonators as determined based on exposure to different salt water concentrations referenced to deionized water. The sensitivity of both rings is approximately 380 nm/RIU [67].

4.3.4 Surface Sensing Measurements

The APTES, SPDP, and probe DNA functionalization described in section 4.2.4 is performed to prepare the PSi ring resonators for detection of a 500 nM target PNA solution. Due to the large sensitivity (>1000 nm/RIU) of the PSi WG to small molecules in ambient conditions [25], the APTES and SPDP surface functionalization steps cannot be unambiguously quantified by the PSi rings resonators because the resonance shift exceeds the FSR. However, the detection of the aforementioned functionalization steps were verified by reflectance measurements on an unpatterned PSi slab WG. As shown in Figure 4.6a, the reflectance shift due to APTES and SPDP is 50 nm and 46 nm, respectively. APTES and SPDP are known to form monolayers of approximately 0.8 nm and 0.68 nm, respectively, which leads to the large spectral shift when they are attached to the internal pore walls. The 10 µm radius PSi ring (FSR ≈ 19 nm) can unambiguously detect the attachment of 100 µM probe DNA, which leads to a resonance shift of 11.10 nm, as shown in Figure 4.6b. This large concentration of probe DNA was used to ensure maximal probe coverage in the pores. Both the 10 μm and 25 μm radius PSi rings are able to detect the capture of 500 nM target PNA. As shown in Figure 4.6b and c, PNA hybridization leads to a resonance shift of 2.00 nm and 1.48 nm for the 10 μm and 25 μm radius PSi rings, respectively. The difference in resonance shift upon PNA attachment is attributed primarily to variation in molecular adsorption on the two samples. Based on the similar bulk sensitivity of the 10 μm and 25 μm radius PSi rings, it is anticipated that the surface sensitivity of the rings should be similar, as well. Accordingly, based on the experimental results, the surface sensitivity of the PSi ring resonators is approximately 4 pm/nM for detection of nucleic acid molecules. The high quality and high sensitivity of the rings demonstrates an order of magnitude increased detection sensitivity compared to traditional SOI ring resonator sensors [18,22]. The detection sensitivity of PSi ring resonator sensors may be further improved by optimizing the probe molecule density in the pores using an in-situ synthesis process for probe DNA or PNA attachment that yields increased DNA-PNA hybridization [55,117,118]. We calculate the limit of detection and intrinsic limit of detection for our device as reported in [19] and [119]. The limit of detection (3σ/sensitivity, where 3σ = 12 pm is the smallest spectral shift that can be reliably measured, as estimated by three times the standard deviation of the resonance wavelength drift due to temperature fluctuations and measurement system noise contributions) for target PNA is 3 nM. The intrinsic limit of detection (FWHM/sensitivity, where FWHM = 0.17 nm is the full-width at half-maximum of the PSi ring resonator resonance) is 42 nM.

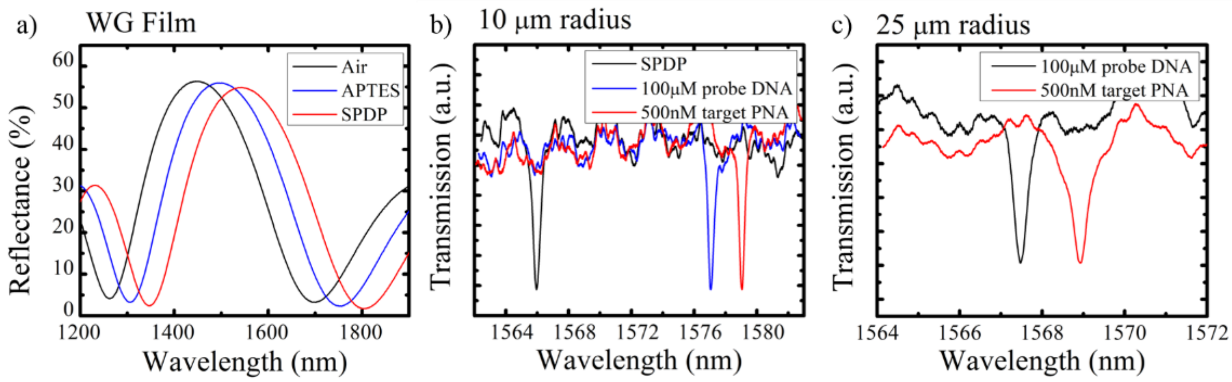

Figure 4.6. (a) PSi slab WG reflectance fringe shifts caused by APTES and SPDP attachment. (b) Resonance shifts of 10 μm radius PSi ring due to attachment of DNA and PNA to a SPDP functionalized surface. (c) Transmission spectra of 25 μm radius PSi ring before and after DNA-PNA hybridization [67].

4.3.5 Nonlinear Response

4.3.5.1 Background

Fluctuations in temperature and laser power will cause refractive index changes in Si, greatly impacting the wavelength position of a high Q factor resonance. This phenomenon is caused by nonlinear effects such as the thermo-optic effect, Kerr effect, free carrier absorption and free carrier dispersion [29,120]. The thermo-optic effect describes the change in refractive index dependent on temperature (dn/dT). In Si, the thermo-optic effect is the dominating nonlinear process ($1.8*10^{-4}$ RIU/K) and is represented by a red shift of the transmission spectrum as temperature is increased [29,120-122]. The centrosymmetric crystal structure of Si results in a strong nonlinear effect on the refractive index properties (known as the Kerr effect) described by the third order susceptibility (χ^3) of the material system [123]. The Kerr effect is manifested as a change in refractive index caused by the carrier response to an applied electric field. In the case of an optical cavity, the light produces the electric field. In Si, the Kerr effect ($4.2*10^{-14}$ cm^2/W) is greatly dominated by the thermo-optic effect in a high Q cavity, but contributes to the net red shift in the wavelength transmission spectrum [29,30]. The free carrier dispersion ($3.5*10^{-21}$ cm^3) and absorption effects ($1.45*10^{-17}$ cm^2) are the changes in the refractive index and absorption coefficients caused by carrier depletion or accumulation, respectively [30,124]. Free carrier absorption can account for cavity heating as laser input power is increased [120]. Free carrier dispersion is the injection of carriers into the supporting substrate, directly affecting the refractive index of the cavity mode and causing a blue shift in the transmission spectrum [29,30,120,124,125]. These nonlinear effects are coupled and their impact on the resonance wavelength position is based on the superposition of each contributing nonlinear shift.

Control of resonance position using these nonlinear effects has been utilized in opto-electronic modulation applications where an intentionally applied electric field or temperature change creates the digital on and off state [125,126]. However, when conditions such as temperature or input laser power change without an intentional trigger, the presence of nonlinear effects can be detrimental to light-matter interaction applications where critical importance is placed on the resonance position (e.g. refractometric-based biosensors). In particular, high Q factor cavity devices such as ring resonators and photonic crystals are particularly susceptible to nonoperational states if an unanticipated wavelength shift occurs due to the small linewidth of the resonance [29]. This effect can result in a false positive in field applications and restrict the biosensor to a controlled lab environment requiring expensive tunable lasers and thermal stages making lab-on-a-chip applications a challenge. Some approaches to stabilize the transducer and avoid nonlinear effects include coating the cavity device with a material that neutralizes the Si thermo-optic effect [122,127], implementing on chip heaters and control systems [126], and dispersion engineering [128].

In this work, the nonlinear response of a PSi ring resonator is evaluated and a novel method to achieve nonlinear stability is proposed. Previous nonlinear studies of PSi have determined that the Kerr coefficient in PSi is 50% smaller than that SOI [30], but the free carrier absorption and dispersion in PSi can be many times greater than in SOI waveguides as a result of high carrier doping [30,129]. Straining Si, for example through formation of SiGe, can also amplify the free-carrier dispersion effect by reducing the conductive effective mass of holes within the film, as can be determined from the Drude model [124]. PSi films can be strained by subjecting the sample to increasing oxidation conditions [130]. When PSi is oxidized, the combination of Si and SiO_2 crystal lattices causes material strain, which increases the carrier effective mass leading to the amplified plasma dispersion effect [124]. Increasing the oxide thickness in the porous network amplifies the plasma dispersion effect. If strained to an appropriate degree, the free carrier dispersion in PSi can compensate for the effects of the thermo-optic coefficient, Kerr coefficient, and free carrier absorption under certain circumstances (e.g., at a fixed temperature but over a broad range of input laser powers). In such a case, it is possible to fabricate a PSi ring resonator whose operation is not affected by input laser power fluctuations if the temperature remains relatively constant. This section presents the nonlinear response of ring resonator samples oxidized at varying conditions when measured at fluctuating temperatures and input laser powers.

4.3.5.2 Nonlinear Response of PSi Ring Resonators

The nonlinear properties of PSi ring resonators are explored over a temperature range of 20°C to 87°C by employing a Physitemp TS-4MP Temperature Controller. At each temperature investigated, the input laser power is adjusted such that the measured output power is swept from 100 nW to 5000 nW. A transmission spectrum is measured at each temperature and power interval.

As has been previously shown, the temperature-dependent optical response of PSi is greatly impacted when the PSi film is subjected to varying oxidation conditions [130,131]. For no or native oxidation, the thermo-optic effect dominates the temperature dependent optical response and a red shift of the transmission or reflection spectrum is observed with increasing temperature between 25°C to 100°C. As oxidation temperatures increase to 400°C, material strain occurs due to oxide growth and a blue shift due to free carrier dispersion is observed at low temperatures (20°C to 40C°). A red shift, caused by the thermo-optic effect, is observed at higher temperatures (from 40°C to 95°C), creating a polynomial temperature response [131]. This is contrary to bulk Si, which shows a linear temperature response between 20°C to 100°C [121]. The PSi polynomial trend can be seen in Figure 4.7a and previous reports [130,131]. High temperature oxidation (900°C) of PSi causes sufficient material strain such that only a resonance blue shift is observed for a temperature sweep from 25°C to 95°C [131]. The minimum of the polynomial can be tuned by adjusting the oxidation conditions of PSi.

The dependence of the resonance wavelength on temperature and laser power was studied for PSi ring resonators with the following oxidation conditions: 300°C for 5 minutes with no ramp; 400°C for 5 minutes with no ramp; 500°C for 5 minutes with no ramp; and 500°C for 5 minutes with a 20 minute ramp. No ramp means the samples were directly placed in the furnace at the corresponding temperature. The 20 minute ramp means that samples are placed in the oven at room temperature, the oven is then ramped over 20 minutes to the target temperature, the samples are held at the target temperature for the stated oxidation duration, and then the samples are directly removed from the oven.

The results of the thermal and laser power sweeps for the PSi rings oxidized at 500°C with and without the temperature ramp are shown in Figures 4.7 and 4.8, respectively. Figure 4.7a and 4.8a trace the PSi ring resonance shift over a temperature sweep and verify the expected polynomial shaped trend. The decreasing and increasing slope, dλ/dT, at the specified temperature directly corresponds to the expected resonance shift caused by power fluctuations. This may be attributed to the enhanced free carrier absorption in PSi resulting in cavity heating. However, the effects from the Kerr effect and free carrier dispersion will also contribute to the net shift resulting from power fluctuations. As shown in Figure 4.7b and 4.8b, the PSi shows a very large blue shift for an increase in power near room temperature (20°C and 30°C). This blue shift can be deduced from the negative slope (dλ/dT) at the corresponding temperatures in Figures 4.7a and 4.8a. Similarly, a positive dλ/dT slope predicts a red shift in the resonance position as power is increased at a fixed external temperature. This result is verified in Figure 4.8d where input power is swept from 100 nW to 5000 nW at a fixed temperature of 80°C. The red shift for the experiment in Figure 4.7 is not shown. Due to thermal vibrations, a steady output power could not be measured above 80°C which is also attributed to the nonlinear red shift observed in Figure 4.8d.

For each oxidation condition, there is a temperature at which the free carrier dispersion balances the thermo-optic effect, Kerr effect, and free carrier absorption (i.e., minimum of the parabolic curve in Figures 4.7a and 4.8a) leads to a resonance shift of dλ/dT = 0. This zero thermo-optic response leads to a stable resonance wavelength that does not fluctuate with changes in input power. For the ramped 500°C sample, the minimum is located at 77°C as outlined in Figure 4.7a. Figure 4.7c depicts a power sweep from 100 nW to 1000 nW at the dλ/dT = 0 point and shows the resonance is not affected by input power fluctuations. Measurements above a 1000 nW output were not carried out. By comparing Figures 4.7a and 4.8a, we find that reducing the oxide thickness in the PSi ringlowers the temperature at which the resonance is immune to laser power fluctuations due to a smaller free carrier dispersion effect.

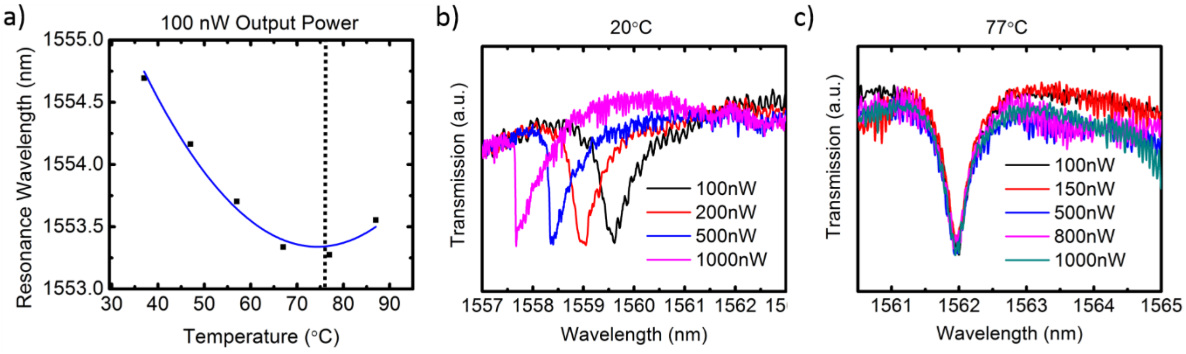

Figure 4.7 a) Temperature response of PSi ring resonator oxidized at 500°C for 5 minutes with a 20 minute ramp. b) Resonance blue shift as the output laser power is increased at a fixed temperature of 20°C. The trend correlates with th negative dλ/dT seen in (a). c) Nonlinear equilibrium is observed at a fixed temperature of 77°C for an output power sweep from 100 nW to 1000 nW.

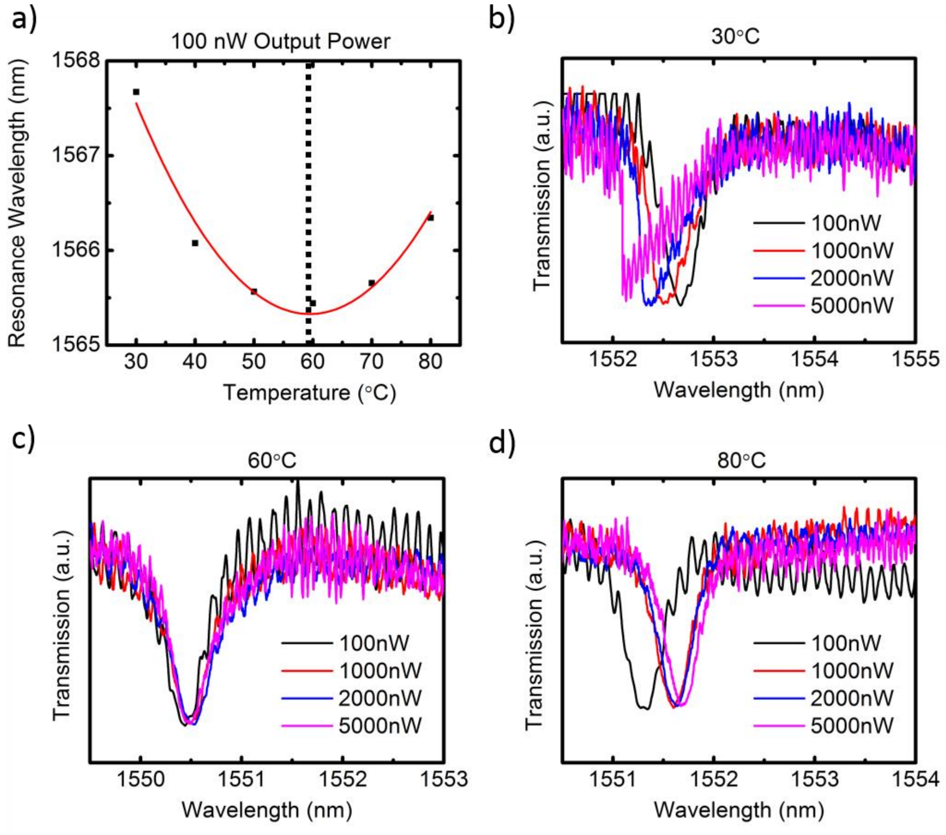

Figure 4.8 a) Temperature response of a PSi ring resonator oxidized at 500°C for 5 minutes with no ramp. b) Output power sweep at 30°C shows a resonance blue shift. c) No resonance shift is observed at a sample temperature of 60°C, corresponding to the zero slope temperature in (a). d) A red shift in the resonance position is observed at 80°C correlating with the positive dλ/dT slope shown from 60°C to 80°C in (a).

The temperature response of samples oxidized at 300°C, 400°C, and500°C for 5 minutes with no ramp and the sample oxidized at 500°C for 5minutes with a 20 minute ramp are shown in Figure 4.9. A continuous resonance blue shift over the temperature sweep is observed for samples oxidized at 300°C and 400°C. We postulate laser-induced oxidation occurs within the cavity, attributed to heating caused by free carrier absorption and the long lifetime of the resonant mode. Laser-induced oxidation has been previously demonstrated in non-resonant PSi films with laser powers as low as 48 mW [132]. The fact that the resonance wavelength does not return to its initial position after the temperature sweep supports this hypothesis. Additionally, it has been found that samples oxidized below 500°C are not stable for biosensing applications. These samples have incomplete oxide coatings that result in low coverage and poor attachment of target molecules [133]. The nonuniform or patchy oxide growth leads to bare Si within the porous matrix that may be susceptible to laser-induced thermal oxidation.

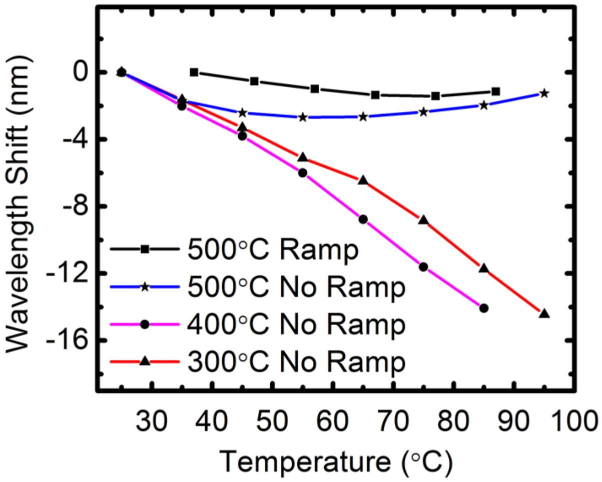

Figure 4.9. Resonance wavelength shift as a function of external temperature. Samples thermally oxidized at 300°C and 400°C are further oxidized by free carrier absorption and heating within the cavity as temperature and input power are increased. The low oxidation temperature samples do not have conformal oxide coverage on the silicon pores walls, making the samples susceptible for additional oxidation. Samples oxidized at 500C for 5 minutes or longer exhibit the polynomial temperature response due to a uniform oxide coating within the porous matrix.

4.3.5.3 Outlook of Nonlinear Stability

In this section, a novel approach to achieve nonlinear stability to power fluctuations is presented. The ability to cause a strain effect by oxidizing PSi amplifies the free carrier dispersion effect, thereby effectively reducing the contributions of the thermo-optic effect, Kerr effect, and free carrier absorption to the cumulative resonance shift upon input laser power modulation. Oxidation conditions of 500°C for 5 minutes with no ramp led to the lowest experimentally demonstrated nonlinear equilibrium at 60°C. By increasing the oxidation conditions, the equilibrium temperature is increased to achieve resonance stability to laser power fluctuations at higher temperatures.

However, reduced oxidation conditions resulted in unstable samples that were susceptible to laser-induced oxidation making room temperature nonlinear equilibrium a challenge. To achieve stability at room temperature, the idea presented here can be extended to other strained material platforms such as Si_xGe_{1-x} [124]. Tuning the material strain based on percentage of Ge in the SiGe alloy can lead to applying the mechanism proposed in this section to achieve stability near room temperature. To achieve both broad temperature and power stability, this novel method may be coupled with temperature stability techniques such as incorporating material platforms that negate thermo-optic coefficients [130]. Additionally, the profound use of SiGe in CMOS electronics can lead to the application of stable optoelectronic modulators that will not be affected by changes in transmitted optical power caused by propagation or cavity losses within the waveguide or fluctuations in the light source itself.

4.6 Summary

This work presents the first demonstration of a PSi ring resonator. Passive characterization of 10 μm and 25 μm PSi rings showed that the structures exhibit Q-factors near 10,000, propagation losses near 2.75 dB/mm, and bending losses less than 1 dB/90° bend. The nonlinear characterization leads to a novel method of achieving power stability at a fixed temperature through dispersion engineering dependent on material strain. Active characterization of the PSi rings demonstrated a bulk detection sensitivity near 380 nm/RIU based on salt water measurements and a surface sensitivity near 4 pm/nM with a limit of detection of 3 nM based on nucleic acid detection. The superior sensing performance of PSi ring resonators compared to traditional ring resonators arises due to the enormous internal surface area of PSi and the resulting strong light-matter interaction between the guided mode and target molecules in the pores. The high detection sensitivity of relatively compact PSi ring resonators along with their capability to detect molecules in a liquid environment opens the door to future microfluidics integration and real-time lab-on-a-chip applications. In Chapter 6, single mode PhC NBs are implemented in PSi to circumvent the FSR challenge observed in the PSi ring resonator.

CHAPTER 5

POROUS SILICON BLOCH SURFACE WAVE RING RESONATORS

5.1. Introduction

As discussed in Chapter 2, light confinement near the surface of a photonic structure is highly advantageous for PSi biosensing. The BSW has the advantage of being able to detect large molecules that cannot infiltrate the porous region; a pitfall that was suffered by both the WG or microcavity structure in Chapter 2 [66,108,110]. The BSW is a propagating mode, similar to the WG. However, instead of being supported by TIR at the substrate cladding interface, light is confined by a PhC Bragg mirror [134]. Prism, grating, and fiber coupled configurations have been demonstrated in BSW ridge and film technology [61,63,64,78,80,83,110,135].Given the similar nature of WG and BSW modes, it is surprising that integrated optical structures, such as ring resonators or photonic crystals, have not been realized on a BSW substrate. Only very recently have optical ring resonators based on BSW films been theoretically proposed [90]. In this work, the effective index method was utilized to design the BSW ridge mode, allowing the design of the ring structure to follow conventional WG based ring designs [85,90].

The simplicity and cost of fabricating a BSW or WG multilayer film in PSi is identical, leading to the natural combination of the work presented in Chapters 2 – 4 to enable the first experimentally demonstrated BSW ring resonator in any material system. This work confirms the theoretically proposed BSW ring resonator device through fabrication and characterization of a ring on a periodic PSi dielectric stack supporting BSWs. The PSi BSW ring is applied for the detection of both large and small molecules. The large molecules are detecting using the BSW surface mode and long-period interference fringes observed in the transmission spectrum allow the detection of very large spectral shifts exceeding the FSR of the device. Hence PSi BSW rings can overcome the upper limit of detection reported in traditional PSi WG ring resonators in Chapter 4 when the spot and dry method of sensing is applied. This first experimental presentation of a BSW ring resonator opens the door to future prototypical photonic resonant devices such as BSW PhC NB cavities or microcavity-based ring resonators, as discussed in the Future Work section in Chapter 7.

5.2. Materials and Methods

5.2.1 Design

FDTD simulations are performed to design the BSW ridge guided mode. Figure 5.1a depicts the conventional ridge modal profile with an approximate n_{eff} of 1.14. An $n_{eff} = 1.16$ was calculated using the effective index approach [90]. The following parameters were determined following the layout and variables in Figure 4.1 in Chapter 4. The width of the BSW ridge is $w_{BSW} = 6$ µm. An r = 105 µm radius ring is patterned with g = 100 nm from the feeding waveguide. No taper is used in these devices to reduce coupling into multilayer modes. The step BSW configuration described in Section 3.2.2 and Figure 3.1b is utilized as the supporting multilayer film structure. A model of the ring resonator supported on a BSW film structure is depicted in Figure 5.1b.

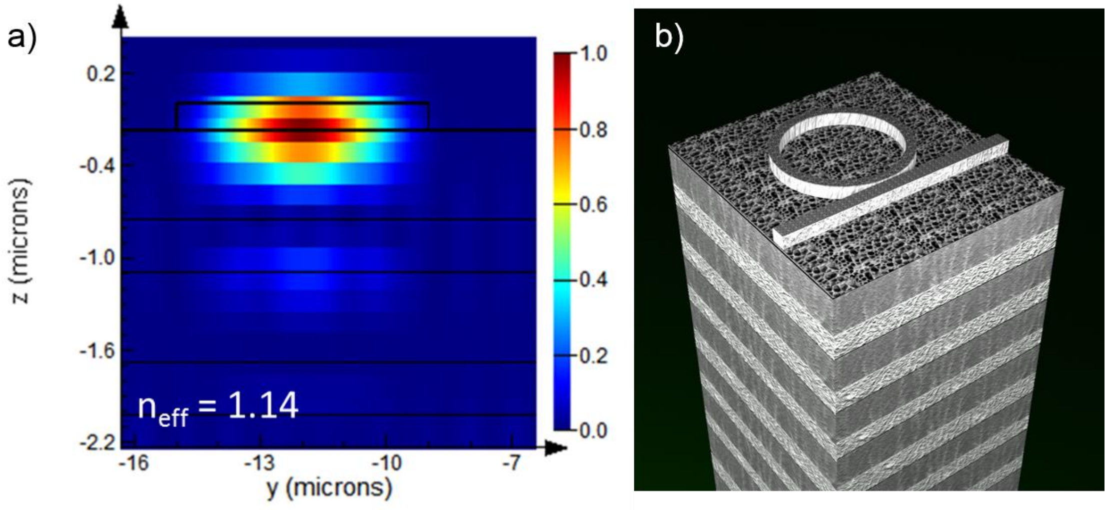

Figure 5.1 a) Cross sectional electric field profile (FDTD simulation) of the BSW ridge guided mode with n_{eff} = 1.14. b) Schematic of a step BSW multilayer supporting a ring resonator device.

5.2.2 Fabrication and Measurement

The fabrication of the BSW multilayer structure is identical to the step configuration described in section 3.2.2. The step configuration is utilized because it is found to reduce coupling of incident light into multilayer modes and evanescently decaying fields excited by a fiber-coupled light source as further discussed in section 5.3.1. A measurable signal could not be realized for a gradient or uniform BSW multilayer using the fiber coupled configuration. The ring resonator pattern is transferred to the first layer of the BSW multilayer structure by EBL as discussed in Section 4.2.2. The RIE etch time was reduced to 1 minute 30 seconds to etch the pattern only into the thin BSW guided layer. Photoresist is removed in a 70°C N-methyl-2-pyrrolidone bath for one hour. Transmission measurements in a fiber coupled system are repeated as described in Section 4.2.3.

5.2.3 Sensor Functionalization

The biosensing application of the PSi BSW ring resonator is examined by the detection of small linker molecules and the capture of the target protein, streptavidin (SA). SA is widely used in the detection of proteins in western blots due to its strong affinity to biotin, a small molecule that conjugates to antibodies and other proteins [136]. The oxidized surface of the PSi BSW ring resonator is silanized using the APTES procedure described in Section 4.2.4. Next, a 3 mM solution of biotin in DI water is drop cast on the sample for thirty minutes to form a near-monolayer biotinylated surface. The sampled is then rinsed with DI water and dried with nitrogen. Next, a 100 nM solution of SA in DI water is placed on the sample for thirty minutes, followed by a DI water rinse and nitrogen drying. Transmission measurements are carried out in between each functionalization step.

5.3. Results and Discussion

5.3.1 BSW Ring Characterization

Figure 5.2a shows a top view SEM image of a patterned BSW ring resonator with parameters discussed in Section 5.2.1. Figure 5.2b shows a cross-sectional view of the step multilayer structure with inset showing the edge of the BSW ridge. The 3-dimensional FDTD simulation of a 10 μm BSW ring resonator results in the transmission spectrum shown in Figure 5.2c. A smaller ring is simulated to reduce computation time. The larger 105 μm ring is utilized in the experimental work because it was found to reduce scattering losses and produced a larger observed Q factor. The full BSW multilayer structure is modeled within the simulation. In Figure 5.2c, ring resonances observed in the transmission spectrum begin at the 1510 nm wavelength and have an FSR of 21 nm. The experimentally measured transmission spectrum of the fabricated 105 μm radius PSi BSW ring is shown in Figure 5.2d. The FSR and Q-factor of the PSi BSW ring resonator are 2.5 nm and 1,000, respectively. The Q factor is estimated based on a Lorentizan fit of several of the resonances. The resonances are excited within relatively long period (~20 nm) sinusoidal oscillations caused by intermodal scattering, where the BSW propagating mode couples into multilayer evanescent modes, as depicted in Figure 5.3a. For clarity, the fringes are not shown in Figure 5.2 but can been seen in Figure 5.3a.

Due to the excitation of multilayer modes and evanescently decaying fields within the multilayer structure [137], resonances for the BSW rings with regular periodic or gradient refractive index profiles could not be resolved using the fiber coupled measurement configuration due to the intensity of multilayer modes. The step configuration was used to reduce the intensity of multilayer modes which is attributed to the extended photonic band gap caused by the step index within the Bragg mirror discussed in Section 3.3.1. Although the step profile reduced the intensity of multilayer modes, intermodal scattering between the propagating BSW and BSSW modes was introduced, resulting in a reduced Q factor when compared to WG based ring resonators. Excited decaying modes within the mirror bring rise to long transmission fringes that allow an accurate trace of very large spectral shifts in biosensing applications as demonstrated in the next section. The presence of multilayer modes can be circumvented by implementing a grating coupler configuration as opposed to the in-plane fiber coupling configuration enacted in this work.

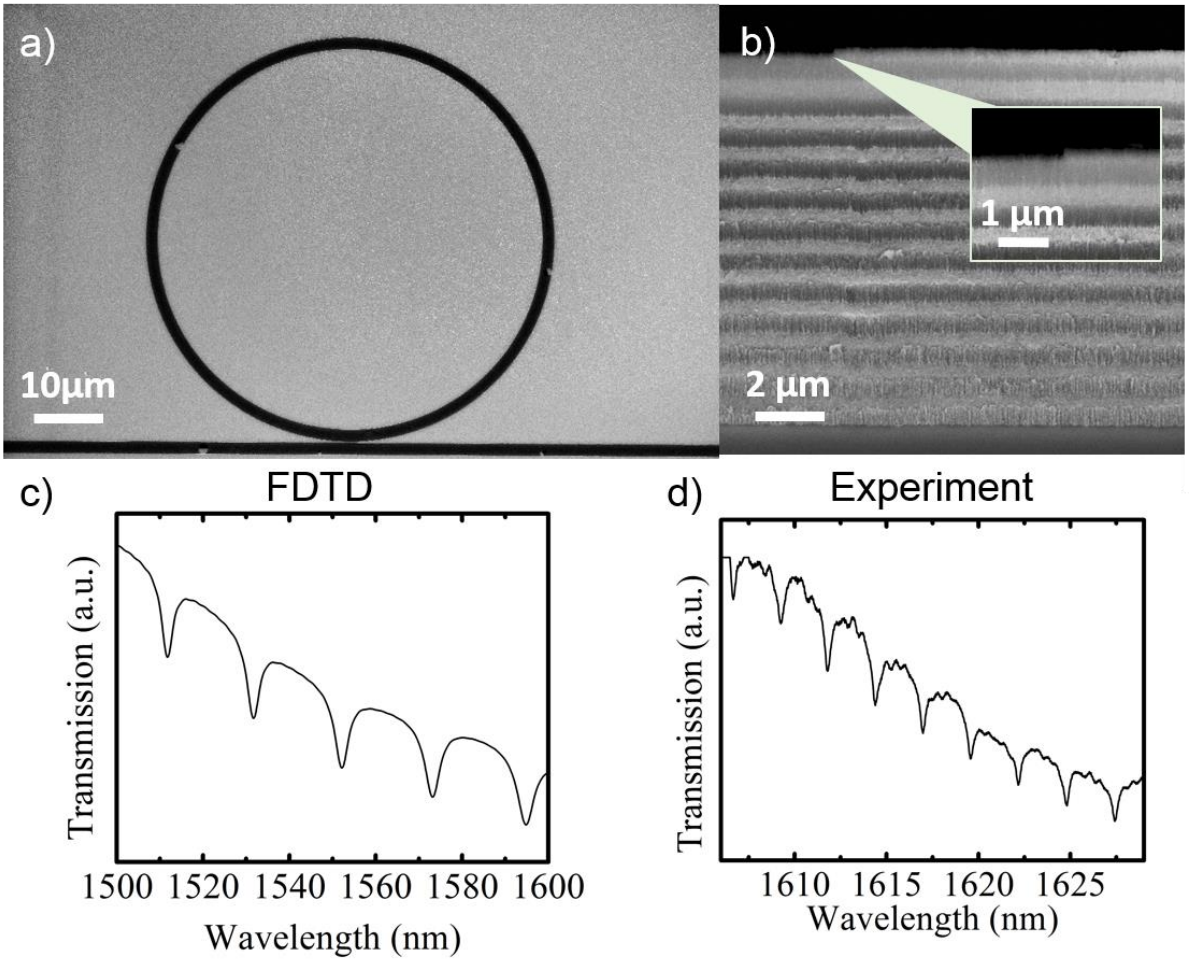

Figure 5.2. a) Top view SEM image of a PSi BSW ring resonator covered with photoresist to clearly outline the ring pattern. b) Cross sectional SEM profile of the multilayer BSW film and the ridge BSW formed by RIE. Inset displays sidewall of etch. c) Transmission spectrum calculated by 3-D FDTD simulation of a 10 μm BSW ring. d) Experimentally measured transmission spectrum of a 105 μm BSW ring.

5.3.2 Sensing Results

The primary advantage of BSW rings for biosensing applications is the long evanescent tail of the mode: in PSi BSW rings, this allows for the detection of large molecules that cannot infiltrate the pores and for other materials, this allows for stronger light-matter interaction between the mode and surface-bound target molecules than can be obtained in a standard ring waveguide geometry [110,138]. In addition, PSi BSW rings can reliably detect the presence of small molecules infiltrating the pores due to interference fringes resulting from the multilayer region of the BSW ring. Figure 5.3a shows long-period transmission fringes of the PSi-BSW that allow for the detection of large spectral shifts near 30 nm caused by attachment of biotin to the APTES coated surface. The ring resonance dips can be observed within the large fringe. Figure 5.3b shows that the surface wave enables detection of the surface-bound SA molecules at 100 nM concentration, leading to a 1.5 nm resonance shift. A surface sensitivity of 15 pm/nM is therefore estimated for SA detection after an incubation time of thirty minutes. These results compare very favorably to those of the PSi WG ring resonator, which cannot uniquely determine the resonance shifts upon capture of modest concentrations of small molecules (e.g., APTES and biotin) due to shifts exceeding the FSR of the ring, and PSi WGs cannot accurately detect the presence of SA molecules that do not enter the pores.

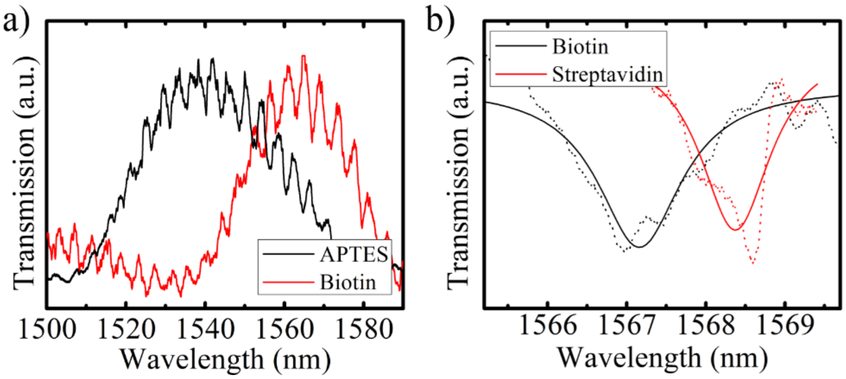

Figure 5.3. a) Wavelength shift of the long period transmission fringes after attaching biotin to an APTES functionalized BSW ring resonator sample. The shorter period BSW ring resonator resonances shift by significantly more than one FSR upon biotin binding. b) Label-free detection of 100 nM of SA protein attached to the biotinylated PSi BSW ring surface using a BSW ring resonance. Lorentzian fits are shown in the solid lines to more clearly outline the BSW resonance before and after SA binding.

5.4. Summary

We report the first experimental demonstration of a BSW ring resonator in any material system where the ring cavity is supported by a photonic crystal substrate in one direction and surface TIR confinement in 2.5 dimensions. The BSW ring resonator was realized in PSi, a material system with an easily tunable refractive index and thickness, allowing quick and economic fabrication of a complex multidimensional cavity structure. This experimental demonstration suggests that other photonic resonator structures could also be realized within the BSW multilayer structure (e.g. a nanobeam or 2-D photonic crystal cavity). Furthermore, the ability to concatenate photonic cavity devices with non-waveguide based supporting films, such as the BSW ring resonator in this chapter, leads to the study and development of novel photonic resonator families that show particular promise for future lab-on-a-chip and sensor array devices.

CHAPTER 6

POROUS SILICON PHOTONIC CRYSTAL NANOBEAMS

6.1 Introduction

On-chip resonant photonic structures including previously discussed ring resonators [14,19,73,139] and multidimensional photonic crystal (PhC) cavities [21,22,74,140-143] have been extensively researched on silicon-on-insulator (SOI) substrates for refractometric-based biosensing applications. PhC one-dimensional nanobeams (NBs) and two dimensional PhC defect cavities in SOI have achieved the highest Q factors (10^7-10^9) and smallest modal volumes (~ 0.7 $(\lambda/n)^3$) [88,144], leading to detections sensitivities ranging from 70 nm/RIU – 90 nm/RIU [142,145]. However, as motivated in Chapter 4 for ring resonators, such detection sensitivities are not competitive with many commercial refractometric-based biosensors including surface plasmon resonance sensors with sensitivities near 1400 nm/RIU [146]. In an effort to improve the detection sensitivity of SOI photonic sensors while preserving the advantages of CMOS fabrication compatibility and miniaturization, slotted PhC NBs [147], air mode PhCs [143], and PhCs with TM polarized modes [148] – all demonstrating the potential for stronger light-matter interaction between the guided mode and target molecules – have been proposed; a significantly improved detection sensitivity near 500 nm/RIU has been predicted [143].

In this work, another approach to improving the detection sensitivity of PhC NB sensors is taken wherein standard lithographic patterning is performed to pattern PhC NBs on high surface area PSi planar waveguide films. Previously, standard lithography as well as patterning based on either selective laser-induced oxidation or the direct imprintation of porous substrates method [149] have been carried out on porous silicon planar waveguides to define PSi ridge waveguides [27,30], MZIs [28], and ring resonators [67,150]. All of these structures are amenable to on-chip integration with photonic and optoelectronic circuits and with microfluidic channels. Relatively high Q factors near 10^4 were presented in PSi ring resonators in Chapter 4, facilitating their ability to experimentally demonstrate the highest reported detection sensitivities (380 nm/RIU in a fluidic environment) among all ring resonator platforms [67]. One limitation of the PSi ring resonator platform arises due to the FSR of the ring. Accentuated by the high detection sensitivity of the PSi ring resonator, large resonance shifts resulting from the attachment of a large concentration of low molecular weight species inside the PSi ring resonator lead to overlapping of the periodic resonances. Hence, except for real-time sensing applications in which the resonance wavelength is continuously monitored, the dynamic sensing range of high sensitivity PSi ring resonators has an upper limit of detection that precludes the unique quantification of even modest concentrations of small molecules such as the common chemical linker, APTES. In this work, we address this challenge, as well as the challenge of increasing the limited detection sensitivity of traditional SOI NB sensors, by employing a newly proposed single mode PSi-PhC NB with a Q-factor of approximately 4,000 and an estimated detection sensitivity of 1130 nm/RIU. The single resonance peak of the PSi NB allows for a large dynamic sensing range for the molecules captured inside the PSi film. We follow a deterministic design approach for the PSi NB that has been previously demonstrated for the efficient and high Q factor design of PhC NBs in low index contrast polymeric materials [87,151]. The dielectric mode PSi NB cavity is shown to outperform a traditional dielectric mode SOI NB cavity for the detection of both chemical molecules and nucleic acid targets.

6.2 Materials and Methods

6.2.1 Device Fabrication and Measurement

The PSi PhC NBs are fabricated similar to the PSi ring resonator in Chapter 4 [67]. PSi waveguides are fabricated by electrochemical etching of p+ (0.01 Ω·cm) Si (100) in a 15% hydrofluoric acid solution in ethanol and water. A current density of 5 mA/cm^2 is applied for 100 seconds to create a 535 nm guiding layer. Next, a 48 mA/cm^2 current density is applied for 100 seconds to form a 2500 nm cladding layer. A 1.5 mM solution of KOH in ethanol is drop cast on the films for five minutes to enlarge the pore diameters, followed by a thorough ethanol rinse. The samples are then thermally oxidized at 500°C for five minutes. The refractive indices of the guiding and cladding layers post fabrication processing are 1.86 and 1.3, respectively, as determined by fitting transfer matrix simulations with measured reflectance spectra using film thicknesses extracted from SEM images. NB patterns are transferred to the PSi waveguide films via electron beam lithography and reactive ion etching. SOI wafers were processed in parallel using the same lithographic and etching techniques in order to form SOI NBs for comparison to the PSi NBs. ZEP 520A is spun at 2000 rpm and exposed by a JEOL JBX-9300-100kV electron beam lithography tool. Samples are then developed in Xylenes for 30 seconds. Next, the NB pattern is etched into the porous guiding layer of the PSi waveguide and the silicon device layer of the SOI wafer with an Oxford Plasmalab 100 reactive ion etcher using C_4F_8/SF_6/Ar gases. Residual photoresist is removed in an N-methyl-2-pyrrolidone bath for 1 hour at 70°C. Samples are manually cleaved to be a width of 1.5 mm. Transmission measurements are carried out using a tunable laser (Santec TSL-510) and fiber coupled setup as previously described [67].

6.2.2 Chemical Preparation

The surface sensitivity of the PSi NBs are first benchmarked based on the non-specific detection of small chemical linker molecules and the specific detection of a 16-base target peptide nucleic acid (PNA) sequence. Oxidized PSi NBs and SOI NBs are functionalized with 3-aminopropyltriethoxysilane (APTES) and succinimidyl 3-(2-pyridyldithio)propionate (SPDP), small linker molecules that form near-monolayers on the PSi and SOI surfaces to capture a thiol-modified probe DNA sequence (5'TAG CTA TGG TCC TCG T-3'). A 4% APTES solution in methanol and deionized (DI) water is placed on the NBs for 15 minutes, followed by a 15 minute soak in methanol to remove excess material. Next, the samples are thermally annealed for 15 minutes and rinsed with methanol. A 4.0 mg/mL solution of SPDP in ethanol is placed on the NBs post APTES attachment for 30 minutes, followed by a 30 minute soak in ethanol to remove unbound molecules. A 100 μM solution of thiol-modified 16-base probe DNA in 4-(2-hydroxyenthyl)-1-piperazineethanesulfonic acid (HEPES) buffer is reduced by tris(20carboxyethyl)phosphine disulfide reducing gel (Pierce) and placed on the SPDP functionalized NBs for one hour. The samples are then soaked in HEPES for 20 minutes and rinsed with DI water. The functionalized samples are soaked in a 1 μM complimentary target PNA (ACG AGG ACC ATA GCT A) solution for one hour followed by a 20 minute soak in DI water. Transmission measurements are performed between each functionalization step.

6.3 Results and Discussion

6.3.1 Nanobeam Design and Theoretical Performance

The PhC NB is a symmetric structure consisting of a periodic array of air holes centered in a ridge waveguide, creating a cavity region surrounded by two mirror sections. Changing the diameter of the holes, while keeping the center-to-center spacing fixed, enables formation of the cavity. The mirrors create a photonic band gap and the cavity creates a defect within the photonic band gap that gives rise to a resonant mode. The mirror segments are designed to quadratically taper to the cavity segment to gently confine light and minimize scattering losses. This approach has been previously shown to result in high transmission (>95%) and radiation-Q limited cavities [87]. The MIT Photonic Bands (MPB) eigensolver (Johnson and Joannopoulos 2001) is used to select the appropriate dimensions for realizing PSi and SOI NBs.

The PSi design consists of a single mode ridge waveguide with 1200 nm width and 700 nm height. The periodicity, *a*, of the holes, which is determined from the effective index (n_{eff}) of the guided mode at $\lambda_0 = 1550$ nm, is $a = \lambda_0/(2\cdot n_{eff}) = 550$ nm. MPB simulations of air hole segments with various filling fractions (i.e., ratios between the hole area and the area of the unit cell) produce the mirror strength plot in Figure 6.1a similar to reference [88]. The air holes constituting the mirror section of the PSi NB are designed with a radius of 170 nm, corresponding to the filling fraction with maximum mirror strength. The radius of the air holes quadratically tapers from the mirror section to the cavity with an air hole radius of 220 nm, which is the filling fraction with zero mirror strength. A zero length cavity is selected to minimize mode volume and maximize the Q factor. To minimize computational time, in simulation we choose 10 mirror segments and 10 taper segments. The field distribution of the PSi NB dielectric-mode calculated using finite difference time domain (FDTD) simulations is shown in Figure 6.1b. In the case of the SOI NB, the same design approach was followed. The SOI ridge waveguide has a 500 nm width and 220 nm height with hole periodicity of 350 nm. The mirror segments consist of air holes of radius 55 nm, and the air hole radius quadratically tapered to 75 nm in the cavity. Again, 10 mirror segments and 10 taper segments were selected in simulation to minimize computation time. Mirror strength and field distribution of the SOI cavity mode have been previously reported for a similar design (Quan and Loncar 2011).

Figure 6.1c and 1d show the FDTD simulated field intensity at the center of the cavity (cross-section) for the PSi and SOI NBs, respectively. The anticipated sensitivity enhancement of the PSi NB is estimated by comparing the field confinement factor of the two designs. The field confinement factor, Γ_s, is described by Equation 1.4.

Figure 6.1c and d are used in the field confinement factor calculation. The sensing area of the PSi PhC NB is considered to be the entire cross-section multiplied by the porosity of the guiding layer, including the evanescent field within the cladding layer and 5 nm from the surface of the device. The field extends <100 nm from the surface of the device, but it is assumed for small molecule sensing applications that only the field within 5 nm of the PSi surface is necessary to fully encompass the molecular extent. As illustrated in the bottom graphic of Figure 6.1c, the pores allow direct interaction of target molecules with the propagating mode. The porosity of the guiding layer is 59%, as determined by Bruggeman effective medium approximation, resulting in $\Gamma_s = 40.54\%$. For the SOI NB, the field within the guiding layer is inaccessible to the molecules, as illustrated in Figure 6.1d, and therefore the sensing area is only the evanescent field in the air cladding, resulting in $\Gamma_s = 1.15\%$. The active sensing field extends <100 nm from the surface of device. The sensor confinement factor of PSi is 35-fold larger than that of SOI due to the large internal surface area promoting direct light matter interactions within the material.

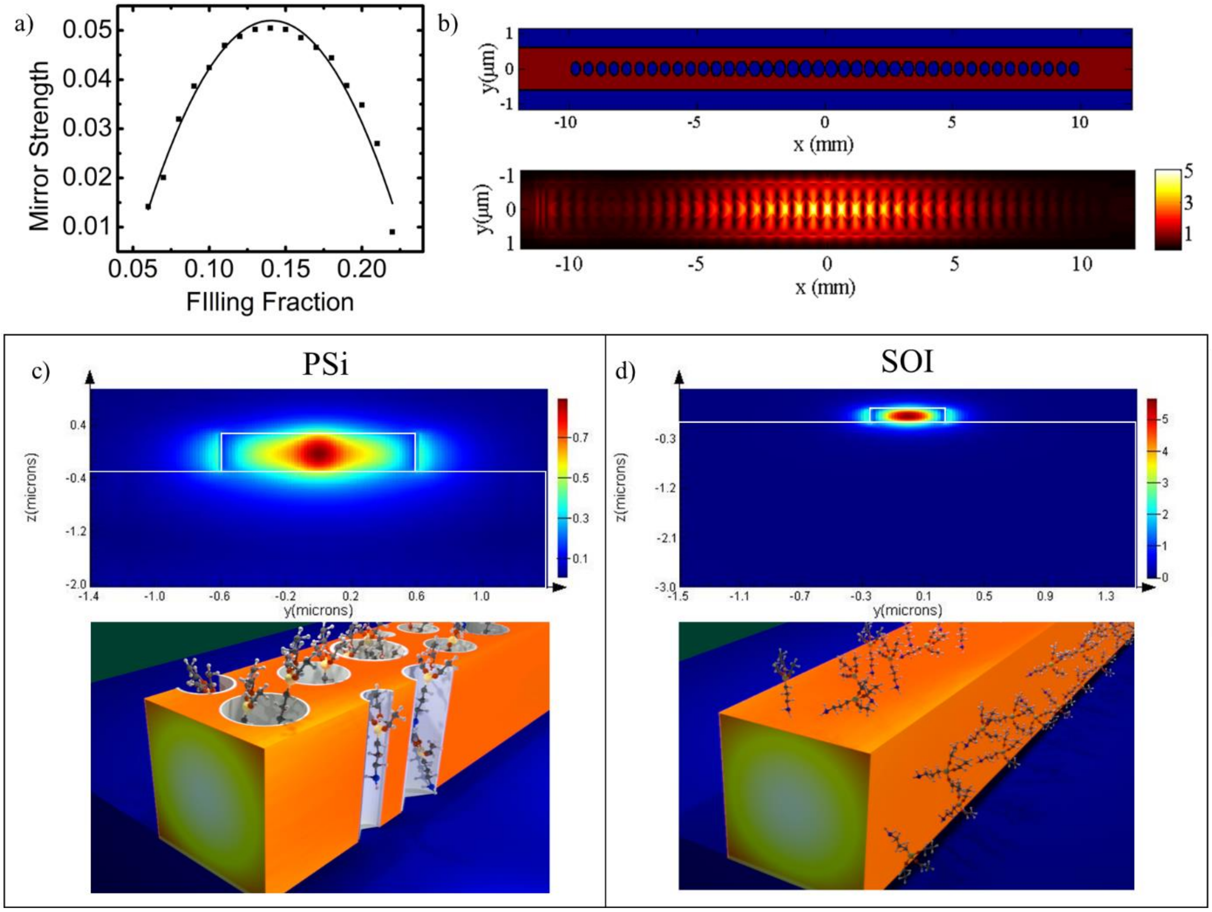

Figure 6.1. a) Mirror strength of different hole filling fractions in PSi ridge waveguide unit cell. b) Field profile of cavity mode in PSi PhC NB (lower) and refractive index profile (upper) where red and blue represent high and low index, respectively. The cross sectional field of the (c) PSi NB and (d) SOI NB used to calculate the field confinement factor. The accessible sensing surface area of PSi (bottom image in (c)) includes the porous regions in the guided layer while only the evanescent field of the SOI NB mode is accessible to target analytes (bottom image in (d)).

6.3.2 Experimental Realization

The SEM images of our fabricated PSi PhC NB are shown in Figure 6.2. Figure 6.2a shows the entire structure consisting of 30 mirror segments and 25 cavity segments. The number of respective segments were determined by optimizing the Q factor of the cavity resonance. A transmission resonance could not be observed for a greater number of mirror and cavity segments. A decrease in the number of segments resulted in NBs with reduced Q factor. Figure 6.2b is a close up SEM image of the mirror segments that illustrates the uniformity of holes in PSi achieved by our fabrication method, and shows the different sized pores of the guiding and cladding layers. The roughness of the ridge and air holes is largely dictated by the pore size. The coupling PSi ridge waveguide is shown in the cross-sectional SEM image of the structure in Figure 6.2c.

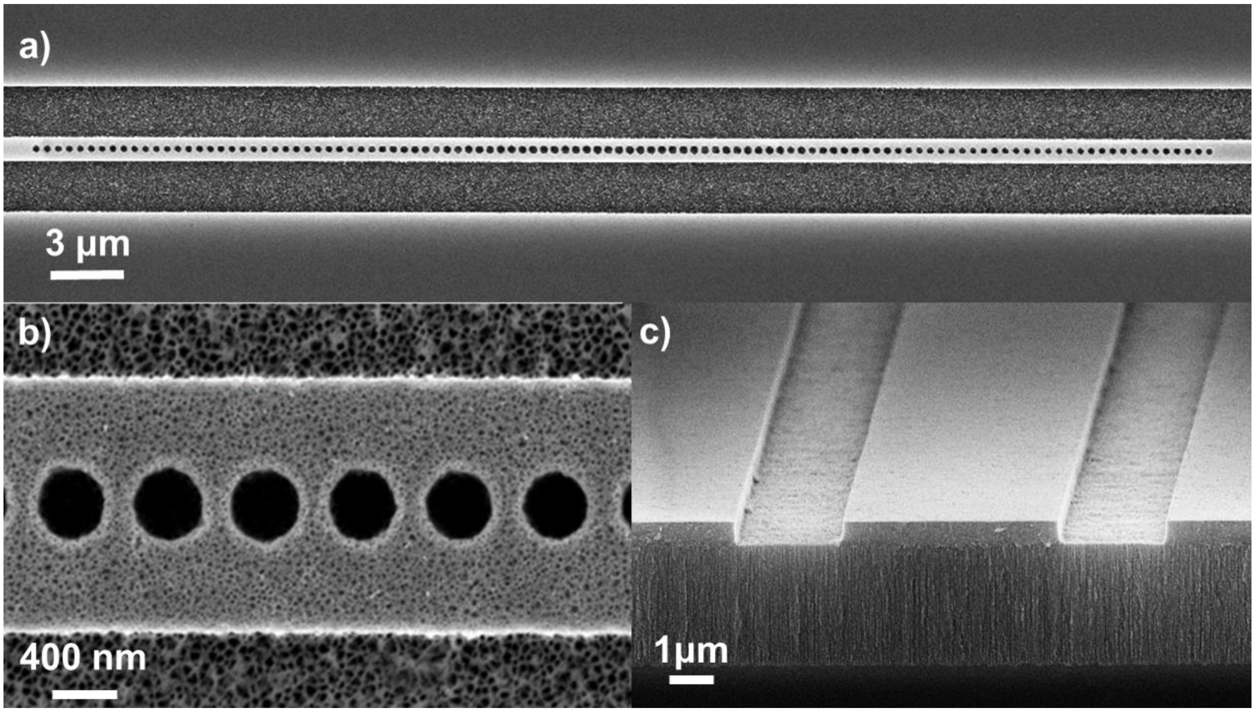

Figure 6.2. (a) SEM image of PSi PhC cavity with 30 mirror and 25 cavity segments and (b) zoom in of air holes in mirror region. (c) Cross-sectional SEM image of the ridge waveguide after the sample is manually cleaved.

The transmission spectrum of the single mode PSi NB is shown in Figure 6.3a, with the cavity resonance and dielectric band edge located at 1549.3 nm and 1555 nm, respectively. Figure 6.3b shows a Q factor near 4,000 for the PSi NB resonance centered near 1550 nm. A maximum Q factor of 9,000 was observed for a PSi NB designed at λ_0 = 1600 nm, as shown in Figure 6.3c, but this initial wavelength was not suitable for sensor experiments due to the limited spectral range of our experimental setup. As previously shown, the deterministic design approach results in radiation limited cavities [87]; therefore, we postulate the Q factor limitations are a result of the porous morphology, the low index contrast between the guiding and cladding layers, uniformity of the etched air holes, and scattering caused by the rough cladding and waveguide interface [104]. The highest SOI NB Q factor observed from samples fabricated in parallel with the PSi NBs is approximately 20,000, as shown Figure 6.3d. Previous reports demonstrate Q factors as high as 10^7 with optimized fabrication conditions [87]. The Q factors of the NB resonances (black) were calculated using a Lorentz fit (red) in Figure 6.3.

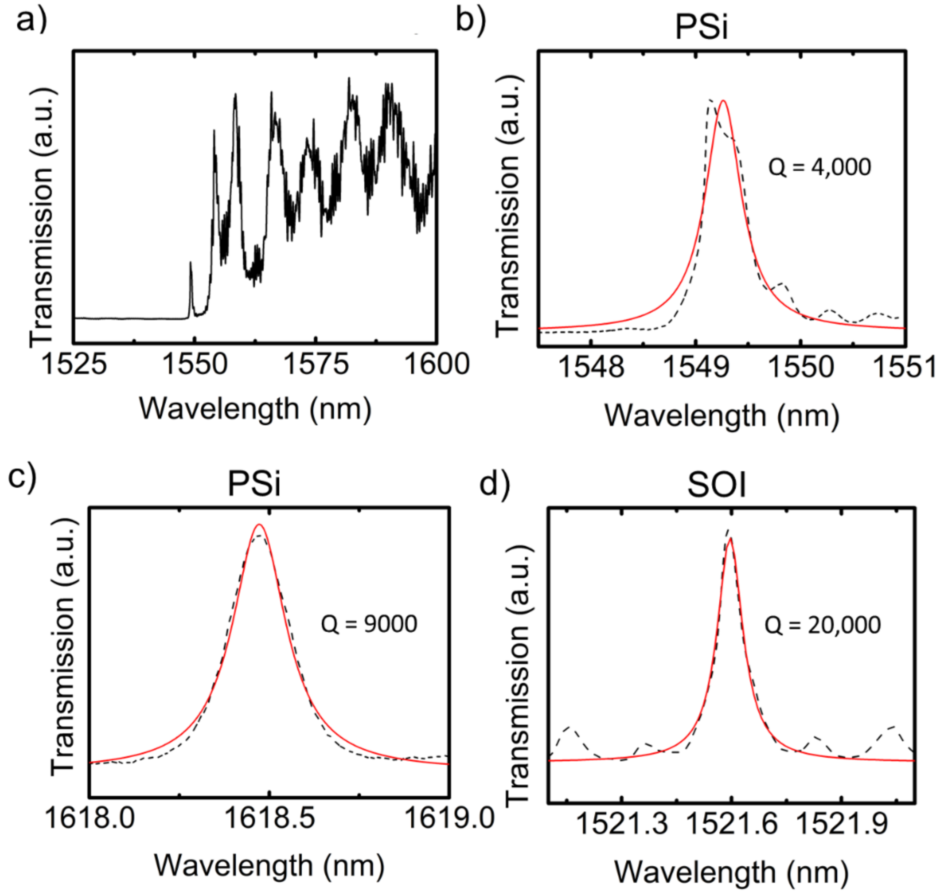

Figure 6.3. (a) Transmission spectrum of PSi NB cavity. The resonance and band edge are located at 1549.25 nm and 1555 nm, respectively. (b) Q factor of the resonant mode in a) is 4,000, calculated by a Lorentzian curve fit for a PSi NB centered at 1550 nm. c) Resonance of PSi NB near 1618 nm, giving the highest observed PSi Q factor among all structures fabricated and measured: 9,000. d) Resonance of SOI NB with Q factor of 20,000.

6.3.3 PSi and SOI PhC NB Sensing Comparison

Figure 6.4 summarizes the results of our biosensing experiment in the PSi and SOI NBs described in the previous characterization section. Figure 6.4a shows the resonance shifts after the attachment of the small linker molecules and oligonucleotides. Detection of the large 34 nm spectral shift of the self-assembled monolayer of APTES allows the experimental calculation of refractive index unit (RIU) molecular sensitivity in an ambient environment. As described by the Bruggeman approximation, a monolayer of approximately 0.8 nm sized molecules within the pores causes a refractive index shift of $\Delta n = 0.03$ (Rodriguez et al. 2014), leading to a molecular sensitivity of 1130 nm/RIU or 42 nm/nm. Note the sensitivity reported is based on changes within the porous matrix and does not incorporate the evanescent field in the cover layer of the device. Figure 6.4c illustrates the same DNA-PNA hybridization detection of the SOI PhC NB. Lorentz fit resonances are illustrated for clarity in order to eliminate Fabry-Perot reflections caused by the fiber-ridge waveguide interface. The noise caused by the reflections leads to a large standard deviation of 1 nm for the full width at half maximum of each resonance, as can be seen from the fluctuating Q factors in Figure 6.4c. This effect has been previously circumvented by incorporating polymer pads at the coupling interface to reduce the Fabry-Perot reflections in plane with the NB cavity [152]. Note that Fabry-Perot reflections are not observed in the case of the PSi NB due to the small refractive index contrast between the air and guiding layer at the fiber-coupling interface. The spectral shift caused by APTES attachment to the SOI NB was approximately 1.1 nm, leading to a molecular sensitivity of 1.3 nm/nm. This value agrees with previous reports utilizing the same surface functionalization chemistry for SOI ring resonators and 2-D PhCs [22]. The 32-fold sensitivity improvement agrees with the simulation presented at the end of section 6.3.1.

The resonance shifts of the PSi and SOI NBs caused by attachment of probe DNA and target PNA are shown in Figure 6.4b and c, respectively. The detection of target PNA using the PSi NB results in a 2 pm/nM sensitivity and is an order of magnitude improved over the SOI NB (0.2 pm/nM). The reduced sensitivity improvement for PNA detection compared to small molecule detection (e.g., APTES and SPDP molecules) is attributed to partial clogging after the probe DNA and small linker molecules are attached on the surface. Pore size and probe molecule surface coverage can be optimized to further improve the target sensitivity [43,153].

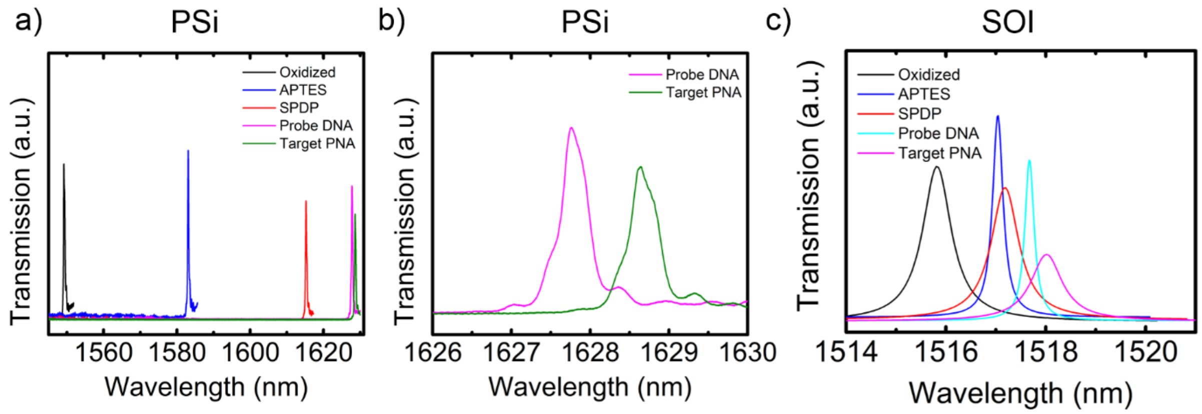

Figure 6.4. Transmission spectra of (a) as-measured PSi NB and (c) Lorentz fit of SOI NB resonances showing the detection of small chemical linker molecules (APTES and SPDP), probe DNA, and target PNA. (b) Zoom in of the as-measured transmission resonance showing PSi detection of 1 μM target PNA.

6.4 Summary

We introduce a PSi PhC NB cavity capable of detecting molecules over a large range of concentrations. The demonstration of the PSi PhC NB overcomes the sensitivity challenges of nonporous SOI sensor platforms for the detection of molecules small enough to be captured in the pores of the guiding layer of the PSi NB. We report an experimental sensitivity of 1130 nm/RIU that is 30-fold greater than a traditional SOI PhC NB, and a detection sensitivity of 2 pm/nM for a 16-base target nucleic acid, which is more than one order of magnitude higher than a SOI PhC NB.

In addition to their high sensitivity and high Q-factors (~10^4), the versatile PSi substrates having compatibility with standard silicon fabrication procedures and reduced cost over silicon-on-insulator substrates make the PSi PhC NBs a promising platform to develop compact multidimensional photonic cavities for future lab-on-a-chip and sensor array devices.

CHAPTER 7

CONCLUSIONS

7.1 Summary

This work investigates the biosensing properties of PSi resonant thin films and for the first time reports their integration with optical devices. This demonstration extends the field of silicon photonics to encapsulate PSi when developing novel optical components. The material achieves competitive sensitivities when compared to SPR commercial sensors and is coupled with the desired lab-on-a-chip properties inherent to compact SOI optical devices. The material reduces cost when compared to SOI, and the supporting film can be tuned such that these devices can be supported on non-WG configurations.

In Chapter 2, the temporal and sensitivity response of both small and large molecules were evaluated using microfluidic integrated microcavity, WG, and BSW PSi films. The three structures show a similar temporal response for molecules <2 nm. A stable concentration of small molecules and large DNA strands was observed within the pores in less than 10 minutes. The microcavity and WG were determined to have an advantage in selectively detecting small molecules within the pores. Surface bound large molecules and particulates do not contribute to the measurable resonance shift of these films. The BSW structure was able to detect the presence of large molecules at the surface, and small molecules within the pores were detected with a reduced sensitivity when compared to the WG. In Chapter 3, these advantages are leveraged to create a novel film, termed the BSW/BSSW sensor, that utilizes both surface and near surface defect states in a PhC to independently and size selectively detect large and small molecules. The BSW mode retains the ability to detect large surface bound molecules as seen in Chapter 2. The novel BSSW mode is a buried WG-like mode that allows selective detection of only small molecules and exhibits a 33% sensitivity enhancement when compared to the WG mode. Additionally, the excitation of both modes with a single reflectance measurement can be utilized to detect molecular infiltration and diffusion within the porous layers in real-time. In Chapter 4, the combination of high Q factor, low modal volume, and cascadable ring resonators with nanoscale PSi WG films resulted in biosensors 40 times more sensitive than their nonporous counterparts. Additionally, a novel technique utilizing dispersion engineering through controlled oxide growth achieves nonlinear stability to fluctuations in input laser power at a fixed ambient temperature. The improved sensitivity, reduced cost over SOI, and nonlinear stability make PSi ring resonators a promising biosensor that can be integrated in on-chip biosensing technology. Additionally, the successful demonstration of a PSi WG-based ring resonator allows for potential implementation of photonic devices within non-WG platforms. The versatility of PSi and successful implementation of ring resonators extends the study of silicon photonics to explore devices with non-WG substrates. In Chapter 5, the step BSW mode is utilized to experimentally demonstrate the first functional BSW ring resonator. The BSW ring resonator exhibited the large molecule sensing advantage presented in Chapter 2 and 3. This implementation suggests future integration of photonic crystal cavities with the BSW mode. Additionally, the functional device also suggests future integration of resonant devices with alternate multilayer supports such as the microcavity or BSSW mode. Lastly, Chapter 6 presents the design and experimental characterization of a single mode PSi-WG PhC NB cavity. The NB exhibits similar Q factor and sensitivity as the ring resonator. However, the lack of a free spectral range in the transmission spectrum allows a much larger dynamic sensing range compared to traditional PSi and SOI ring resonators, and enables the detection of large spectral shifts created by self-assembled monolayers of small chemical molecules. The following section presents future ideas that may optimize the structures in this work as well as explore novel geometries for PSi biosensors.

7.2 Future Work

7.2.1 Device Optimization

As seen in Chapter 2, the PSi WG is capable of detecting only molecules that infiltrate the pores. For this reason, pore diameter is a significant tunable parameter when surface functionalization steps require long linker molecule chains. In this work, the index contrast between porous layers was maximized in order to achieve the strongest realizable cavity confinement. However, as a result of the 10 – 20 nm pore size of the high index layer, steric hindrance and diffusion limitations were observed as a result of pore clogging. Pore size and accessible binding sites are reduced as the linker molecule chain of APTES, SPDP, and probe DNA are grown within the pore. As seen in Chapter 6, the sensitivity improvement over SOI diminishes from 40 fold to 10 fold as the linker molecules, probe DNA, and target PNA are attached to the sensor. In order to prevent these effects, an optimization of confinement versus pore size is required. The pore size can be individually tailored to each biosensing application to reduce infiltration limitations. The pore can be widened by increasing KOH concentration and exposure post PSi fabrication or by reducing the porosity of the guiding layer during the etching procedure. The Q factor of the cavity device may diminish as a result of the reduced index contrast between layers. The resonant devices such as the ring resonator and PhC NB will require redesign to account for the n_{eff} of the new guided mode.

7.2.2 Bloch Surface Wave Multidimensional Photonic Crystal Cavities

The realization of a BSW ring resonator suggests the development of a novel family of resonators based on BSW films. The natural progression will be to implement 1-D photonic crystal NB cavities within the multilayer film. Utilizing the step BSW presented in Chapter 3, the NB device can be deterministically designed with n_{eff} = 1.16 [87]. A model of the proposed PSi BSW NB with periodic circles is shown in Figure 7.1. Previous reports determine the use of periodic ellipsoids will maximize Q factor and mirror strength for guided modes with low effective index [151]. The investigation of periodic shape will be important to maximize field confinement within the cavity, such as ellipsoids and rectangles. The single NB mode will eliminate ambiguity faced by large spectral shifts due to the small FSR observed in the PSi BSW ring resonator for biosensing applications. Further investigation can lead to the development of a 2-D PhC cavity, described in Section 1.4.2, realizing a cavity confined by PhC in 2.5 dimensions and TIR in 0.5 dimensions. Although the nanobeam and 2-D PhC cavity have similar Q factors in SOI [154], it will be important to determine if the same phenomenon occurs in low index materials. This can be realized by investigating cavity losses produced by TIR and PhC confinement independently, and can be achievable through the integration of multidimensional PhC cavity structures.

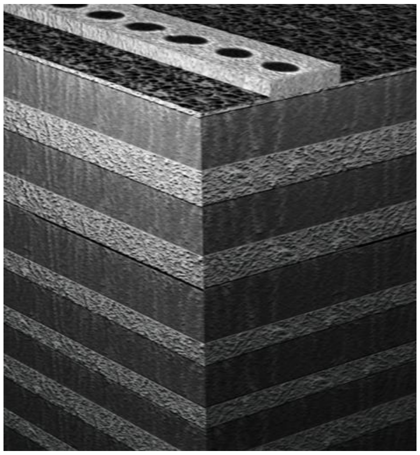

Figure 7.1 3-D model of the proposed PSi BSW PhC NB.

7.2.3 Three Dimensional Photonic Crystals Based on Porous Silicon Films

7.2.3.1 Checkerboard 3-D PSi PhCs

3-D PhCs have been challenging to both fabricate and characterize in many material platforms [86,155]. Future work in PSi can lead to simple fabrication of the checkerboard 3-D crystal depicted in Figure 7.2. The structure can be fabricated by using an offset etching procedure of layers of alternating porosity. The checkerboard mask material can be patterned using photo- or electron beam- lithography as shown in images 1 and 2 in Figure 7.2. Next, the initial high porosity layer is etched. The Si under the masked area will not form a porous layer. Next, the mask is removed and a conventional Bragg mirror can be etched into the structure to create the 3-D checkerboard pattern through an offset etch. There have been no prior reports of selective offset etching and a novel procedure will require optimization of an intrinsic mask material that can be submerged in hydrofluoric acid without causing field effects at the surface of the device that interfere with the offset etch. The insulating material will circumvent field effects at the corners of the patterned checkerboard region that may result in curvature of the pores, creating a poor lateral interface between periodic cells. This simple and cost-effective development of 3-D PhCs near telecom wavelength can lead to the development of new resonator structures.

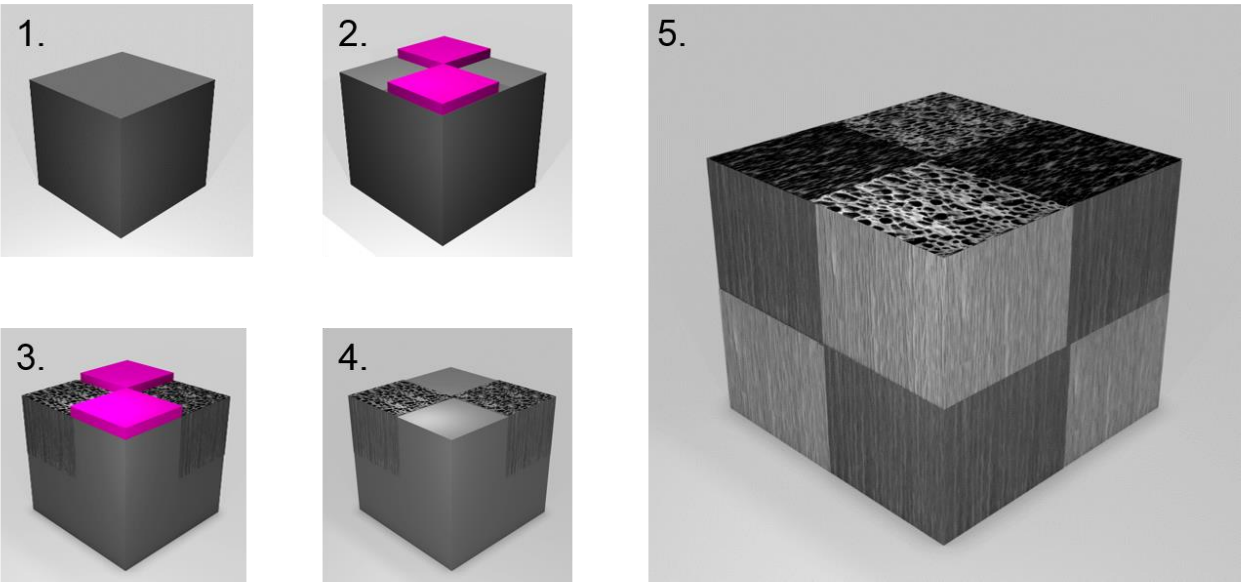

Figure 7.2. Proposed method of fabricating checkerboard 3-D PhCs. A doped Si wafer (1) is patterned with a checkerboard pattern mask (2). An initial layer is etched into the material to form the first checkered layers (3). The mask is then removed (4). Next, the Bragg mirror is etched into the sample, offset by first checkered layer (5).

7.2.3.2 Microcavity Integrated Resonant Devices

Success in developing a family of resonators in BSW films allows the exploration of integrating resonators within different film structures that support a confined light mode, such as the microcavity. Figure 7.3 depicts a model of a ring resonator microcavity. The advantage of this device is it does not require a coupling configuration such as the prism or grating, and simple reflection measurements would be capable of exciting the cavity mode. This would require careful design such that the microcavity mode within the photonic bandgap aligns to create constructive interference within the ring structure. The angle of incident light will also be required to meet TIR conditions for confinement in the ring in addition to exciting the microcavity mode. If the proposed device is successful, future work can lead to 3-D PhC confined cavities by implementing a 2-D PhC cavity with the microcavity structure that may excite high Q cavity modes without the need for a coupling configuration and can be excited for light at any incident angle.

Figure 7.3 3-D model of a PSi microcavity ring resonator.

7.2.4 On-chip optical sources and photodetectors

The versatility and ability to infiltrate PSi multilayer structures with various materials creates a new realm of research that may lead to the success of fully integrated optoelectronic modulators and lab-on-a-chip biosensors. This proposed work investigates the electroluminescence, photoluminescence, and defect luminescence of nanocrystal semiconductors, graphene, and quantum dots within a PSi light guiding device in an effort to determine if optical emitters can successfully excite a guided mode. If achieved, an in depth study could be pursued to determine the most efficient emitter within a nanoscale pore and mechanisms (e.g. structuring distributed Bragg reflectors around the composite material) for efficient directional coupling into nanowire waveguides. Figure 7.4 presents a model of a fully integrated PSi ring resonator with monolithic light source and photodetector. The emitting material within the pores will excite the lateral ridge WG. In order to efficiently and directionally couple light from the emitter into the WG, an on-chip directional mirror may be required. A PSi annular Bragg mirror is proposed to surround the emitting material to promote directional coupling into the waveguide that excites the ring resonator cavity. Materials used for both emitters and photodetectors such as graphene, nanocrystal p-n or p-i-n semiconductors, or quantum dots can infiltrate the porous structure via drop casting, spin coating, chemical vapor deposition, and thermal evaporation techniques. Next, development of on-chip photodetectors will require two main components: 1) a structured photonic device to split different wavelengths such as an on-chip diffraction grating and 2) a waveguide array that is infiltrated with a photodetector material such as graphene or GaAs based quantum dots, as shown in the right side of Figure 7.4. Fabrication of PSi infiltrated with graphene [156], annular Bragg mirrors [157], and ring resonators have been demonstrated and show promise for the success of developing on-chip sources and detectors.

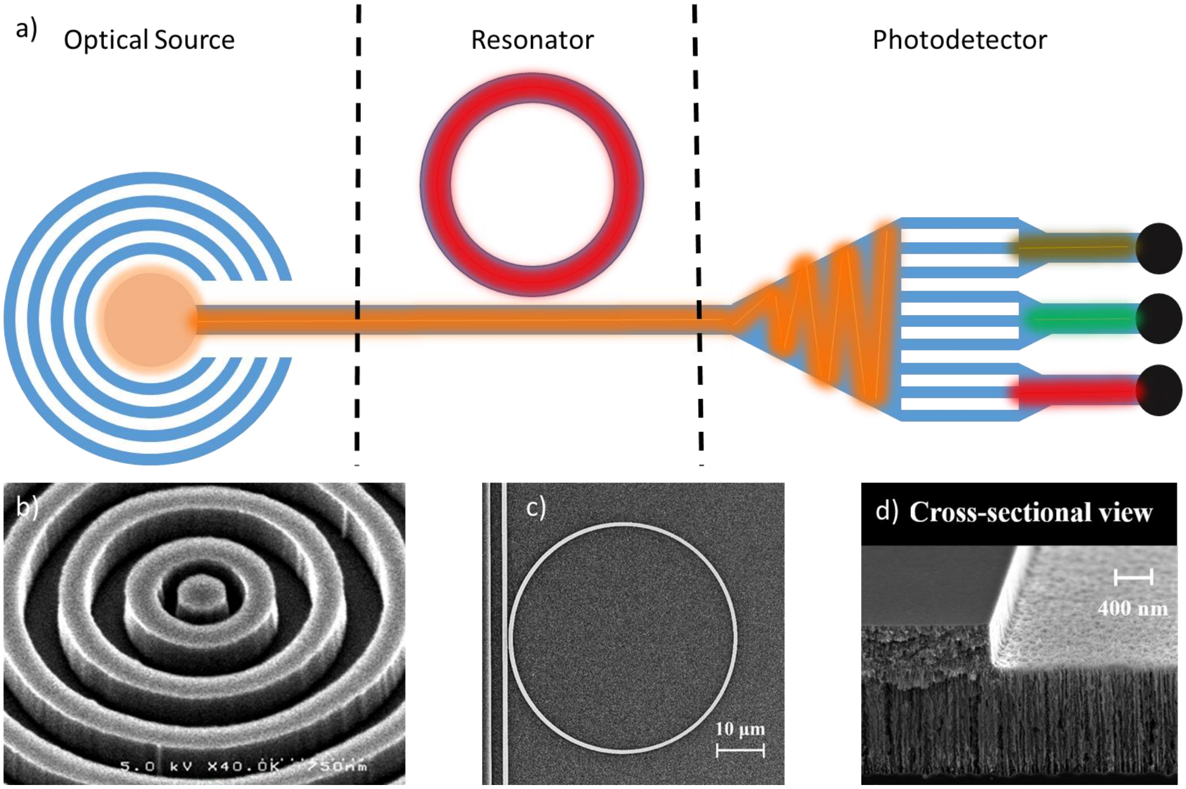

Figure 7.4 a) A ring resonator with fully integrated optical source and photodetector. Blue is PSi. White areas are etched away. Peach and black are the source and detector, respectively. Other colors represent propagating waveguide modes of various wavelengths. b-d) Show successful implementation of a annular Bragg mirror, ring resonator, and the smooth sidewalls achieved in PSi, respectively. b) is adapted from [157], and c) and d) are adapted from [67].

REFERENCES

[1] L. Gervais, N. De Rooij, and E. Delamarche, Adv. Mater. **23**, H151 (2011).

[2] M. U. Farooq, M. Waseem, S. Mazhar, A. Khairi, and T. Kamal, International Journal of Computer Applications **113**, 7 pages (2015).

[3] G. Rong, J. D. Ryckman, R. L. Mernaugh, and S. M. Weiss, Appl. Phys. Lett. **93**, 161109 (2008).

[4] M. Archer, M. Christophersen, and P. M. Fauchet, Biomedical Microdevices **6**, 203 (2004).

[5] L. H. Lie, S. N. Patole, A. R. Pike, L. C. Ryder, B. A. Connolly, A. D. Ward, E. M. Tuite, A. Houlton, and B. R. Horrocks, Faraday Discuss. **125**, 235 (2004).

[6] F. Bessueille, V. Dugas, V. Vikulov, J. P. Cloarec, E. Souteyrand, and J. R. Martin, Biosens. and Bioelectron. **21**, 908 (2005).

[7] G. Di Francia, V. La Ferrara, S. Manzo, and S. Chiavarini, Biosensors and Bioelectronics **21**, 661 (2005).

[8] X. Fan, I. M. White, S. I. Shopova, H. Zhu, J. D. Suter, and Y. Sun, Anal. Chim. Acta. **620**, 8 (2008).

[9] G. P. Stone, R. L. Mernaugh, and F. R. Haselton, Biotechnol Bioeng. **91**, 699 (2005).

[10] K.-P. S. Dancil, D. P. Greiner, and M. J. Sailor, J. Am. Chem. Soc. **121**, 7925 (1999).

[11] B. H. Clare and N. L. Abbott, Langmuir **21**, 6451 (2005).

[12] X. Lv, L. Chen, H. Zhang, J. Mo, F. Zhong, C. Lv, J. Ma, and Z. Jia, Biosens. and Bioelectron. **39**, 329 (2013).

[13] K. De Vos, I. Bartolozzi, E. Schacht, P. Bienstman, and R. Baets, Opt. Express **15**, 7610 (2007).

[14] T. Claes, J. G. Molera, K. De Vos, E. Schacht, R. Baets, and P. Bienstman, IEEE Photonics Journal **1**, 197 (2009).

[15] Y. Zhang, Progress in Natural Science-Materials International **23**, 481 (2013).

[16] Genalyte, Inc. www.genalyte.com (2016).

[17] M. Iqbal, M. A. Gleeson, B. Spaugh, F. Tybor, W. G. Gunn, M. Hochberg, T. Baehr-Jones, R. C. Bailey, and L. C. Gunn, IEEE Journal of Selected Topics in Quantum Electronics **16**, 654 (2010).

[18] A. J. Qavi, T. M. Mysz, and R. C. Bailey, Anal. Chem. **83**, 6827 (2011).

[19] C. F. Carlborg *et al.*, Lab Chip **10**, 281 (2010).

[20] A. Densmore *et al.*, IEEE Photonics Technology Letters **18**, 2520 (2006).

[21] C. Kang, S. M. Weiss, Y. A. Vlasov, and S. Assefa, Opt. Express **37**, 2850 (2012).

[22] S. Hu, Y. Zhao, K. Qin, S. T. Retterer, I. I. Kravchenko, and S. M. Weiss, ACS Photonics **1**, 590 (2014).

[23] F. Dell'Olio and V. M. N. Passaro, Opt. Express **15** (2007).

[24] Y. Jiao and S. M. Weiss, Biosens. and Bioelectron. **25**, 1535 (2010a).

[25] X. Wei and S. M. Weiss, Opt. Express **19**, 11330 (2011).

[26] G. Rong, A. Najmaie, J. E. Sipe, and S. M. Weiss, Biosens. and Bioelectron. **23**, 1572 (2008a).

[27] X. Wei and S. M. Weiss, Mater. Res. Soc. Symp. Proc. **1301**, 219 (2011).

[28] K. Kim and T. E. Murphy, Opt. Express **21**, 19488 (2013).

[29] T. Uesugi, B.-S. Song, T. Asano, and S. Noda, Opt. Express **14**, 377 (2006).

[30] P. Apiratikul, A. M. Rossi, and T. E. Murphy, Opt. Express **17**, 3396 (2009).

[31] V. Almeida, R. and M. Lipson, Opt. Letters **29**, 2387 (2004).

[32] A. Pham, H. Qiao, B. Guan, M. Gal, J. J. Gooding, and P. J. Reece, J. Appl. Phys. **109** (2011).

[33] M. J. Sailor, *Porous silicon in practice* (Wiley VCH Verlag & CO. KGaA, 2012).

[34] H. A. Santos, *Porous silicon for biomedical applications* (Woodhead Publishing, 2014).

[35] L. Canham, *Handbook of porous silicon* (Springer Reference, 2014).

[36] M. Ge, X. Fang, J. Rong, and C. Zhou, Nanotechnology **24** (2013).

[37] A. Jane, R. Dronov, A. Hodges, and N. H. Voelcker, Trends in Biotechnology **27**, 230 (2009).

[38] R. L. Smith and S. D. Collins, J. Appl. Phys. **71** (1992).

[39] V. Lehmann and U. Gosele, Appl. Phys. Lett. **58**, 856 (1991).

[40] X. G. Zhang, S. D. Collins, and R. L. Smith, J. Electrochem. Soc. **136**, 1561 (1989).

[41] R. Voicu, R. Boukherroub, V. Bartzoka, T. Ward, J. T. C. Wojtyk, and D. D. M. Wayner, Langmuir **20**, 11713 (2004).

[42] C. S. Solanki, R. R. Bilyalov, J. Poortmans, J. P. Celis, J. Nijs, and R. Mertens, J. Electrochem. Soc. **151**, C307 (2004).

[43] J. L. Lawrie, Y. Jiao, and S. M. Weiss, IEEE Transactions on Nanotechnology **9**, 596 (2010).

[44] M. Khardani, M. Bouaicha, and B. Bessais, Phys. Stat. Sol. (c) **4**, 1986 (2007).

[45] G. Rong, A. Najmaie, J. E. Sipe, and S. M. Weiss, Biosens. and Bioelectron. **23**, 1572 (2008).

[46] S. Content, W. C. Trogler, and M. J. Sailor, Chem. Eur. J **6**, 2205 (2000).

[47] T. Guinan, M. Ronci, H. Kobus, and N. H. Voelcker, Talanta **99**, 791 (2012).

[48] V. S. Y. Lin, K. Motesharei, K.-P. S. Dancil, M. J. Sailor, and M. R. Ghadiri, Science **278**, 840 (1997).

[49] L. De Stefano, P. Arcari, A. Lamberti, C. Sanges, L. Rotiroti, I. Rea, and I. Rendina, Sensors **7**, 214 (2007).

[50] R.-t. Yamaguchi, K.-i. Miyamoto, K.-i. Ishibashi, A. Hirano, S. M. Said, Y. Kimura, and M. Niwano, J. Appl. Phys. **102**, 14303 (2007).

[51] V. Vamvakaki and N. A. Chaniotakis, Electroanalysis **20**, 1845 (2008).

[52] S. Chan, P. M. Fauchet, Y. Li, L. J. Rothberg, and B. L. Miller, Phys. Stat. Sol. (a) **182**, 541 (2000).

[53] S. Chan, Y. Li, L. J. Rothberg, B. L. Miller, and P. M. Fauchet, Materials Science and Engineering C **15**, 277 (2001).

[54] C. Steinem, A. Janshoff, V. S. Y. Lin, N. H. Volcker, and M. R. Ghadiri, Tetrahedron **60**, 11259 (2004).

[55] Y. Zhao, J. L. Lawrie, K. R. Beavers, P. E. Laibinis, and S. M. Weiss, ACS Appl. Mater. Interfaces **6**, 13510 (2014).

[56] N. H. Voelcker, I. Alfonso, and M. R. Ghadiri, Chembiochem. **9**, 1776 (2008).

[57] C. Pacholski, M. Sartor, M. J. Sailor, F. Cunin, and G. M. Miskelly, J. Am. Chem. Soc. **127**, 11636 (2005).

[58] P. A. Snow, E. K. Squire, P. S. J. Russel, and L. T. Canham, J. Appl. Phys. **86**, 1781 (1999).

[59] S. Li, D. Hu, J. Huang, and L. Cai, Nanoscale Res. Lett. **7**, 1 (2012).

[60] X. Wei, J. W. Mares, Y. Gao, D. Li, and S. M. Weiss, Biomed. Opt. Express **3**, 1993 (2012).

[61] H. Qiao, B. Guan, J. J. Gooding, and P. J. Reece, Opt. Express **18**, 15174 (2010).

[62] E. Guillermain, V. Lysenko, R. Orobtchouk, T. Benyattou, S. Roux, A. Pillonnet, and P. Perriat, Appl. Phys. Lett. **90**, 241116 (2007).

[63] F. Michelotti, B. Sciacca, L. Dominici, M. Quaglio, E. Descrovi, F. Giorgis, and F. Geobaldo, Phys. Chem. Chem. Phys. **12**, 502 (2010).

[64] C. Jamois, C. Li, R. Orobtchouk, and T. Benyattou, Photonics and Nanostructures - Fundamentals and Applications **8**, 72 (2010).

[65] J. D. Ryckman, M. Liscidini, J. E. Sipe, and S. M. Weiss, Appl. Phys. Lett. **96**, 171103 (2010).

[66] G. A. Rodriguez, J. D. Ryckman, Y. Jiao, R. L. Fuller, and S. M. Weiss, Proc. of SPIE, Frontiers in Biological Detection: From Nanosensors to Systems V **8570** (2013).

[67] G. A. Rodriguez, S. Hu, and S. M. Weiss, Opt. Express **23**, 7111 (2015).

[68] X. Wei, C. Kang, M. Liscidini, G. Rong, S. T. Retterer, M. Patrini, J. E. Sipe, and S. M. Weiss, J. Appl. Phys **104**, 123113 (2008).

[69] S. D. J., A. Tao, M. Law, R. Fan, and P. Yang, Adv. Mater. **19**, 61 (2007).

[70] N. Skivesen, A. Tetu, M. Kristensen, J. Kjems, L. H. Frandsen, and P. I. Borel, Opt. Express **15**, 3169 (2007).

[71] B. Momeni, E. S. Hosseini, M. Askari, M. Soltani, and A. Adibi, Optics Communications **282**, 3168 (2009).

[72] C. R. Pollock, *Fundamentals of Optoelectronics* CBLS, 1995).

[73] M. Iqbal, M. A. Gleeson, B. Spaugh, F. Tybor, W. G. Gunn, M. Hochberg, T. Baehr-Jones, R. C. Bailey, and L. C. Gunn, IEEE J. Sel. Topics Quantum Electron. **16**, 654 (2010).

[74] S. Pal, E. Guillermain, R. Sriram, B. L. Miller, and P. M. Fauchet, Biosens. and Bioelectron. **26**, 4024 (2011).

[75] J. Xia, A. M. Rossi, and T. E. Murphy, Opt. Letters **37**, 256 (2012).

[76] R. J. Suess, M. M. Jadidi, K. Kim, and T. E. Murphy, Opt. Express **22**, 17466 (2014).

[77] M. Liscidini and J. E. Sipe, J. Opt. Soc. Am. B **26**, 279 (2009).

[78] A. Sinibaldi, N. Danz, E. Descrovi, P. Munzert, U. Schulz, F. Sonntag, L. Dominici, and F. Michelotti, Sensors and Actuators B: Chemical **174**, 292 (2012).

[79] M. Liscidini, M. Galli, M. Patrini, R. W. Loo, M. C. Goh, C. Ricciardi, F. Giorgis, and J. E. Sipe, Appl. Phys. Lett. **94**, 043117 (2009).

[80] E. Descrovi, T. Sfez, M. Quaglio, D. Brunazzo, L. Dominici, F. Michelotti, H. P. Herzig, O. J. F. Martin, and F. Giorgis, Nano Lett. **10**, 2087 (2010).

[81] V. N. Konopsky and E. V. Alieva, Anal. Chem. **79**, 4729 (2007).

[82] S. Pirotta *et al.*, J. Phys. Chem. C **117**, 6821 (2013).

[83] K. Toma *et al.*, Biosens. and Bioelectron. **43**, 108 (2013).

[84] G. A. Rodriguez, J. D. Ryckman, Y. Jiao, and S. M. Weiss, Biosens. and Bioelectron. **53**, 486 (2014).

[85] W. Bogaerts *et al.*, Laser Photonics Rev. **6**, 47 (2012).

[86] J. D. Joannopoulos, S. G. Johnson, J. N. Winn, and R. D. Meade, *Photonic crystals: Molding the flow of light* (Princeton University Press, 2008), 2nd edition edn.

[87] Q. Quan and M. Loncar, Opt. Express **19**, 18529 (2011).

[88] Q. Quan, P. B. Deotare, and M. Loncar, Appl. Phys. Lett. **96** (2010).

[89] C. Jamois, R. B. Wehrspohn, L. C. Andreani, C. Hermann, O. Hess, and U. Gosele, Photonics and Nanostructures - Fundamentals and Applications **1**, 1 (2003).

[90] M. Menotti and M. Liscidini, J. Opt. Soc. Am. B **32** (2015).

[91] G. Z. Mashanovich, M. M. Milosevic, M. Nedeljkovic, N. Owens, B. Xiong, E. J. Teo, and Y. Hu, Opt. Express **19**, 7112 (2011).

[92] D. I. Siapkas and C. C. Katsidis, Applied Optics **41**, 3978 (2002).

[93] E. Hecht, *Optics* (Addison Wesley, 2002), 4th Edition edn.

[94] P. Yeh, *Optical waves in layered media* (Wiley, 1988).

[95] M. G. Moharam, E. B. Grann, D. A. Pommet, and T. K. Gaylord, J. Opt. Soc. Am. A **12**, 1068 (1995).

[96] R. C. Rumpf, Progress in Electromagnetics Research B **35**, 241 (2011).

[97] M. G. Moharam and T. K. Gaylord, Journal of the Optical Society of America **71**, 811 (1981).

[98] G. Mur, IEEE Transactions on Electromagnetic Compatibility **23**, 377 (1981).

[99] K. Yee, IEEE Transactions on Antennas and Propagation **14**, 302 (1966).

[100] I. Rea, E. Orabona, A. Lamberti, I. Rendina, and L. De Stefano, Biomicrofluidics **5**, 34120 (2011).

[101] G. Gaur, D. S. Koktysh, and S. M. Weiss, Adv. Funct. Mater. **23**, 3604 (2013).

[102] K. C. Tang, E. Liao, W. L. Ong, J. D. S. Wong, A. Agarwal, R. Nagarajan, and L. Yobas, Journal of Physics: Conference Series **34**, 155 (2006).

[103] R. Joshi, H. Janagama, H. P. Dwivedi, T. M. A. S. Kumar, L.-A. Jaykus, J. Schefers, and S. Sreevatsan, Molecular and Cellular Probes **23**, 20 (2009).

[104] P. J. Reece, G. Lerondel, W. H. Zheng, and M. Gal, Appl. Phys. Lett. **81**, 4895 (2002).

[105] A. M. Rossi, L. Wang, V. Reipa, and T. E. Murphy, Biosens. and Bioelectron. **23**, 741 (2007).

[106] N. Massad-Ivanir, G. Shtenberg, A. Tzur, M. A. Krepker, and E. Segal, Anal. Chem. **83**, 3282 (2011).

[107] J. Homola, S. S. Yee, and G. Gauglitz, Sensors and Actuators B: Chemical **54**, 3 (1999).

[108] G. A. Rodriguez, J. D. Lonai, R. L. Mernaugh, and S. M. Weiss, Nanoscale Res. Lett. **9**, 1 (2014).

[109] M. Zhu, M. Z. Lerum, and W. Chen, Langmuir **28**, 416 (2012).

[110] G. A. Rodriguez, J. D. Ryckman, Y. Jiao, and S. M. Weiss, Biosens. and Bioelectron. **53**, 486 (2014).

[111] P. Lalanne, S. Mias, and J. P. Hugonin, Opt. Express **12**, 458 (2004).

[112] H. Ouyang, C. C. Striemer, and P. M. Fauchet, Appl. Phys. Lett. **88**, 163108 (2006).

[113] F. Dell'Olio and V. M. N. Passaro, Opt. Express **15**, 4977 (2007).

[114] M. Mancuso, J. M. Goddard, and D. Erickson, Opt. Express **20**, 245 (2011).

[115] Y. A. Vlasov and S. J. McNab, Opt. Express **12**, 1622 (2004).

[116] J. W. Mares and S. M. Weiss, Appl. Opt. **50**, 5329 (2011).

[117] J. L. Lawrie, Z. Xu, G. Rong, P. E. Laibinis, and S. M. Weiss, Phys. Stat. Sol. A **206**, 1339 (2009a).

[118] K. R. Beavers, J. W. Mares, C. M. Swartz, Y. Zhao, S. M. Weiss, and C. L. Duvall, Bioconjugate Chem. **25**, 1192 (2014).

[119] S. M. Grist *et al.*, Opt. Express **21**, 7994 (2013).

[120] P. E. Barclay, K. Srinivasan, and O. Painter, Opt. Express **13**, 801 (2005).

[121] J. Komma, C. Schwarz, G. Hofmann, D. Heinert, and R. Nawrodt, Appl. Phys. Lett. **101**, 4 pages (2012).

[122] E.-S. Kang, M. Takahashi, Y. Tokuda, and T. Yoko, Appl. Phys. Lett. **89** (2006).

[123] R. Boyd, *Nonlinear Optics* (Academic Press, Elsevier, 2008), 3rd Edition edn.

[124] Y. Kim, M. Takenaka, T. Osada, M. Hata, and S. Takagi, Scientific Reports **4**, 6 pages (2014).

[125] F. C. Ndi, J. Toulouse, T. Hodson, and D. W. Prather, Opt. Letters **30**, 2254 (2005).

[126] K. Padmaraju and K. Bergman, Nanophotonics (2013).

[127] Y. Kokobun, N. Funato, and M. Takizawa, IEEE Photonic Tech L **5** (1993).

[128] A. Blanco-Redondo, D. Eades, J. Li, S. Lefrancois, T. F. Krauss, B. J. Eggleton, and C. Husko, Optica **1** (2014).

[129] R. J. Seuss, M. M. Jadidi, K. Kim, and T. E. Murphy, Opt. Express **22**, 17466 (2014).

[130] S. M. Weiss, M. Molinari, and P. M. Fauchet, Appl. Phys. Lett. **85**, 1980 (2003).

[131] S. M. Weiss, University of Rochester, 2005.

[132] L. De Stefano, I. Rea, M. A. Nigro, F. G. Della Corte, and I. Rendina, Journal of Physics: Condensed Matter **20**, 5 pages (2008).

[133] X. Wei, Vanderbilt University, 2012.

[134] P. Yeh, A. Yariv, and A. Y. Cho, Appl. Phys. Lett. **32** (1978).

[135] V. Paeder, V. Musi, L. Hvozdara, S. Herminjard, and H. P. Herzig, Sensors and Actuators B **157**, 260 (2011).

[136] M. H. Doolittle, O. Ben-Zeev, and V. Briquet-Laugier, Journal of Lipid Research **39**, 934 (1998).

[137] M. Saba and G. E. Schroder-Turk, Crystals **5**, 14 (2015).

[138] H. Qiao, A. H. Soeriyadi, B. Guan, P. J. Reece, and J. J. Gooding, Sensors and Actuators B: Chemical **211**, 469 (2015).

[139] A. Ramachandran *et al.*, Biosens. and Bioelectron. **23**, 939 (2008).

[140] Y. Akahane, T. Asano, B.-S. Song, and S. Noda, Nature **425**, 944 (2003).

[141] M. E. Beheiry, V. Liu, S. Fan, and O. Levi, Opt. Express **18**, 22702 (2010).

[142] F. Liang, N. Clarke, P. Patel, M. Loncar, and Q. Quan, Opt. Express **21**, 32306 (2013).

[143] D. Yang, H. Tian, and Y. Ji, Applied Optics **54**, 1 (2015).

[144] Y. Akahane, T. Asano, B.-S. Song, and S. Noda, Opt. Express **13**, 1202 (2005).

[145] Q. Quan, Harvard University, 2012.

[146] S. J. Zalyubovskiy, M. Bogdanova, A. Deinega, Y. Lozovik, P. A. D., K. H. An, W. P. Hall, and R. A. Potyrailo, J. Opt. Soc. Am. A **29**, 994 (2012).

[147] J. D. Ryckman and S. M. Weiss, IEEE Photonics Journal **3**, 986 (2011).

[148] T.-W. Lu, P.-T. Lin, and P.-T. Lee, Opt. Letters **37**, 569 (2012).

[149] J. D. Ryckman, M. Liscidini, J. E. Sipe, and S. M. Weiss, Nano Lett. **11**, 1857 (2011).

[150] P. Girault *et al.*, Optical Materials **50**, 167 (2015).

[151] Q. Quan, I. B. Burgess, S. K. Y. Tang, D. L. Floyd, and M. Loncar, Opt. Express **19**, 22191 (2011).

[152] K. Kruse and C. T. Middlebrook, Opt. Communications **362**, 87 (2016).

[153] J. L. Lawrie and S. M. Weiss, Phys. Stat. Sol. C **8**, 1851 (2011).

[154] P. B. Deotare, M. W. McCutcheon, I. W. Frank, M. Khan, and M. Loncar, Appl. Phys. Lett. **94**, 3 pages (2009).

[155] J. D. Joannopoulos, P. R. Villeneuve, and S. Fan, Nature, 143 (1997).

[156] J. Kim, S. S. Joo, K. W. Lee, J. H. Kim, D. H. Shin, S. Kim, and S.-H. Choi, ACS Appl. Mater. Interfaces **6**, 20880 (2014).

[157] G. Gaur, Vanderbilt University, 2015.